# BOLD and non-BOLD signal fluctuations in line-scanning fMRI at 7 Tesla

**Catarina Inês Rosa Passarinho**

Thesis to obtain the Master of Science Degree in

## Biomedical Engineering

Supervisors: Prof. Patrícia Margarida Piedade Figueiredo
MSc. Luisa Raimondo

### Examination Committee

Chairperson: Prof. João Miguel Raposo Sanches
Supervisor: MSc. Luisa Raimondo
Member of the Committee: Prof. Rita Homem de Gouveia Costanzo Nunes

**November 2021**

# Declaration

I declare that this document is an original work of my own authorship and that it fulfills all the requirements of the Code of Conduct and Good Practices of the Universidade de Lisboa.

# Preface

The work presented in this thesis was performed at the Spinoza Centre for Neuroimaging (Amsterdam, The Netherlands), during the period February - June 2021, under the supervision of Prof. Wietske van der Zwaag and PhD. student Luisa Raimondo. The thesis was co-supervised at Instituto Superior Técnico by Prof. Patrícia Figueiredo.

# Acknowledgments (***Agradecimentos***)

I would like to begin by thanking the entire supervision team for their support and expertise throughout this project. I am very grateful to Professor Patrícia Figueiredo for the pleasant lectures that expanded my interest in MRI and for creating the link between IST and Spinoza, which made this experience possible. I must also thank Dr. Wietske van der Zwaag and Luisa Raimondo, for welcoming me into their team at Spinoza and for all the knowledge, opportunity and kindness I have received from them during this project.

For supporting me through these last five years, a gigantic ”thank you” is due to my family and closest friends. To my mom, my dad, and my brother, who have been extremely patient and supportive - I could not have done it without you. A very special and heartfelt ”thank you” to my grandparents Alice, José, Herculina, João and Isidra, that do everything to make sure I am well and happy. I must also mention my godparents Inês and Rui, my aunt Helena and uncle Alexandre and my cousins Ana and Marlene, who have given me strength to fearlessly follow my dreams since I can remember. Last but not least, I must thank the unconditional support I have received from Rodrigo, the best person I know, and the friendship from Afonso, Francisca, Sibele and Miguel, who have celebrated my achievements but also gotten me through the toughest moments in the past years.

*Gostaria de começar por agradecer às minhas supervisoras pelo seu apoio e partilha de conhecimento ao longo deste projeto. Estou muito agradecida à Professora Patrícia Figueiredo pelas aliciantes aulas que expandiram o meu interesse em MRI e por criar a ligação entre o IST e o Spinoza, tornando esta experiência possível. Não posso deixar de agradecer à Dra. Wietske van der Zwaag e à Luisa Raimondo, por me acolherem na sua equipa no Spinoza e por todo o conhecimento, oportunidades e gentileza que me deram durante este projeto.*

*Por todo o apoio durante estes últimos 5 anos, devo um enorme agradecimento à minha família e amigos mais próximos. Para a minha mãe, o meu pai, e o meu irmão, que têm sido tão pacientes comigo durante todo o curso - não teria conseguido fazê-lo sem vocês. Um obrigada muito especial e cheio de carinho aos meus avós Alice, José, Herculina, João e Isidra, que tudo fazem para que eu esteja bem e feliz. Não posso deixar de mencionar os meus padrinhos Inês e Rui, os meus tios Helena e Alexandre e as minhas primas Ana e Marlene, que desde que me lembro me encorajaram a seguir os meus sonhos sem quaisquer receios. Por último, mas não menos importante, quero agradecer o apoio incondicional do Rodrigo, a melhor pessoa que conheço, e a amizade do Afonso, Francisca, Sibele e Miguel, que festejaram vitórias comigo, mas também me ajudaram em tantos dos piores momentos destes últimos anos.*

# Abstract

Neurons are spatially organized in columnar and laminar structures that measure hundreds of micrometers and communicate between themselves on a millisecond timescale. Therefore, an fMRI technique with increased spatial and temporal resolutions, such as line-scanning fMRI, is required for the study of sub-millimeter structures of the brain and sub-second activity of cortical grey matter. Because the BOLD response induced by neuronal activity only represents a small percentage of the signal variance in fMRI, denoising the BOLD signal is a critical step in the processing pipeline of task-based fMRI. Four healthy volunteers were scanned on a 7 Tesla MRI scanner while performing a visual task. The sequence used included two slab-selective saturation pulses for outer volume suppression. Subjects' respiratory and cardiac fluctuations were simultaneously recorded using external hardware. Thermal noise was removed using a weighted echo combination and an in-house implementation of NORDIC PCA. The removal of other noise sources, such as physiological fluctuations, was carried out by relying on the TE-dependence of fMRI signals, the results of an ICA decomposition and the outcome of RETROICOR-based signal regression. Echo-combination, NORDIC PCA and the regression of RETROICOR-based physiology regressors yielded significant reduction of thermal noise and physiological fluctuations within line-scanning data. Overall, the denoising results presented offer valuable insight into noise removal in line-scanning fMRI acquired at 7T, and NORDIC PCA revealed the best potential for improving BOLD sensitivity.

**Keywords:** fMRI, line-scanning, noise removal, BOLD contrast, 7T

## Resumo

Neurónios estão organizados em estruturas colunares e laminares que medem centenas de micrómetros e que comunicam entre si a uma escala temporal de milisegundos. Assim sendo, é necessária uma técnica de ressonância magnética funcional com elevada resolução espacial e temporal que possibilite o estudo de estruturas cerebrais sub-milimétricas e de atividade cortical ultra-rápida, tal como *line-scanning* fMRI. O contraste dependente do nível de oxigenação sanguínea (*BOLD*) apenas representa uma pequena percentagem da variância do sinal de MRI funcional, pelo que a remoção de ruído é essencial no processamento do sinal de fMRI. Quatro voluntários saudáveis foram submetidos a uma sessão de fMRI adquirida a 7 Tesla e baseada numa tarefa visual. A sequência utilizada incluiu dois pulsos de radiofrequência para a supressão do sinal fora da linha de interesse. Os ciclos respiratórios e cardíacos de cada voluntário foram adquiridos simultaneamente através de hardware externo. A remoção de ruído térmico foi feita através da combinação ponderada das várias aquisições de fMRI e usando uma implementação adaptada do algoritmo NORDIC PCA. A extração de outras fontes de ruído, como variações do foro fisiológico, foi conseguida através do estudo da relação entre os sinais de fMRI e os respetivos tempos de aquisição TE, da análise de decomposições ICA e de regressões lineares usando diferentes modelos RETROICOR. Os resultados aqui apresentados oferecem informação relevante sobre a remoção de ruído em dados de *line-scanning* adquiridos a 7T, e a implementação de NORDIC PCA revelou o maior potencial para melhorar a sensibilidade ao contraste BOLD.

**Palavras-chave:** imagem por ressonância magnética funcional, *line-scanning*, remoção de ruído, contraste *BOLD*, 7T

# Contents

# List of Tables

# List of Figures

# List of Abbreviations

**BOLD** Blood Oxygenation Level-dependent.

**CBF** Cerebral Blood Flow.

**CBV** Cerebral Blood Volume.

**CMRO$_2$** Cerebral Metabolic Rate of Oxygen consumption.

**CSF** Cerebrospinal Fluid.

**EEG** Electroencephalography.

**FFT** Fast Fourier Transform.

**FID** Free Induction Decay.

**fMRI** Functional Magnetic Resonance Imaging.

**GLM** General Linear Model.

**GM** Grey Matter.

**GSR** Global Signal Regression.

**HRF** Hemodynamic Response Function.

**ICA** Independent Component Analysis.

**MEG** Magnetoencephalography.

**MRI** Magnetic Resonance Imaging.

**NMR** Nuclear Magnetic Resonance.

**OVS** Outer Volume Suppression.

**PCA** Principal Component Analysis.

**PPG** Photoplethysmography.

**PSC** Percent Signal Change.

**PVE** Partial Volume Effects.

**RF** Radiofrequency.

**ROI** Region Of Interest.

**SAR** Specific Absorption Rate.

**SNR** Signal-to-Noise Ratio.

**SoS** Sum of squares.

**SPIR** Spectral Presaturation with Inversion Recovery.

**SVD** Singular Value Decomposition.

**TE** Echo Time.

**tSNR** Temporal Signal-to-Noise Ratio.

**WM** White Matter.

# Chapter 1

# Introduction

## 1.1 Motivation

Functional magnetic resonance imaging (fMRI) is a widely used tool in neuroscience to study evoked responses in the brain. It has allowed for incredible advances in our understanding of human brain function, in particular blood oxygenation level-dependent (BOLD) fMRI.

BOLD fMRI data is acquired with a temporal resolution of seconds and up to submillimeter spatial resolution [1]. However, neurons are spatially organized in columnar and laminar structures (see Figure 1.1) that measure hundreds of micrometers [2] and communicate between themselves on a millisecond timescale [3]. Thus, an fMRI technique with increased spatial and temporal resolutions is required for the study of sub-millimeter structures of the brain and sub-second activity of cortical grey matter.

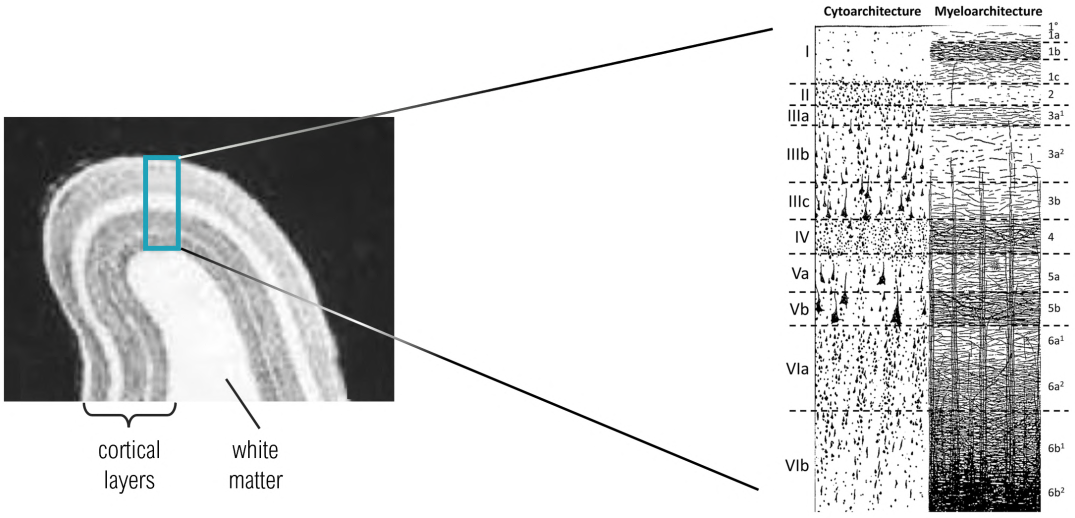

Figure 1.1: **(Left)** Illustration of cortical layers of the primary visual cortex V1. Adapted from [4]. **(Right)** Schematic of cyto- and myeloarchitecture cortical layering. Adapted from [5].

The balance between high spatial and temporal resolutions presents as a challenge - very high spatial resolution typically comes at the cost of low temporal resolution, resulting in slow sampling of the hemodynamic response and subsequent prolonged scan times and loss of functional specificity [2].

Line-scanning fMRI at ultra-high magnetic field strengths (7T and above) is able to reach very high spatial resolutions without compromising very high temporal resolutions. This is possible by sacrificing spatial coverage of the brain volume. However, as shown by Kruger et al. in 2001 [6], the sensitivity of the fMRI signal to non-neuronal physiological contributions increases with higher field strengths. Therefore, the ultra-high static magnetic field strength of 7T, the small voxel size (~250μm) and the very short TR (~100ms) typically used in line-scanning fMRI, lead to appreciable contributions from both physiological fluctuations and thermal noise.

The BOLD response induced by neuronal activity only represents a small percentage (2-3%) of the variance of the fMRI signal [7]. Non-neuronal contributions to the BOLD fMRI signal within a voxel include thermal noise inherent to the electrical circuits used for NMR signal reception, signal changes due to head motion and physiological fluctuations (such as cardiac and respiratory noise), changes in arterial $CO_2$ concentration and vasomotion mechanisms. Hence, denoising the BOLD fMRI signal is a critical step in the processing pipeline of task-based fMRI [8]. It is essential that established denoising techniques, as well as new procedures, are adapted or implemented and applied to line-scanning fMRI to take advantage of the great potential of this method.

## 1.2 Basic principles

### 1.2.1 Magnetic Resonance Imaging

Nuclear magnetic resonance (NMR) was simultaneously discovered by Felix Bloch and Edward Purcell in 1947, and the Nobel Prize in Physics was shared by both in 1952. This non-invasive technique allowed physicists to observe and measure the magnetic properties of nuclear particles, and later provided the underlying physical principles for magnetic resonance imaging (MRI), which started being used for medical applications in the 1970s.

MRI uses magnetic fields and radiofrequency pulses instead of the radiation used in X-ray imaging, therefore avoiding exposure to the harmful effects of ionizing particles. This imaging technique relies on the abundance of water molecules in the human body and on their magnetic properties, namely, hydrogen protons within water molecules are usually targetted. The application of a very strong static magnetic field ($B_0$) causes the magnetic moments (”spins”) of hydrogen protons to align along the direction of the magnetic field, providing a small, but measurable NMR signal that precesses around the axis of $B_0$ (see Figure 1.2).

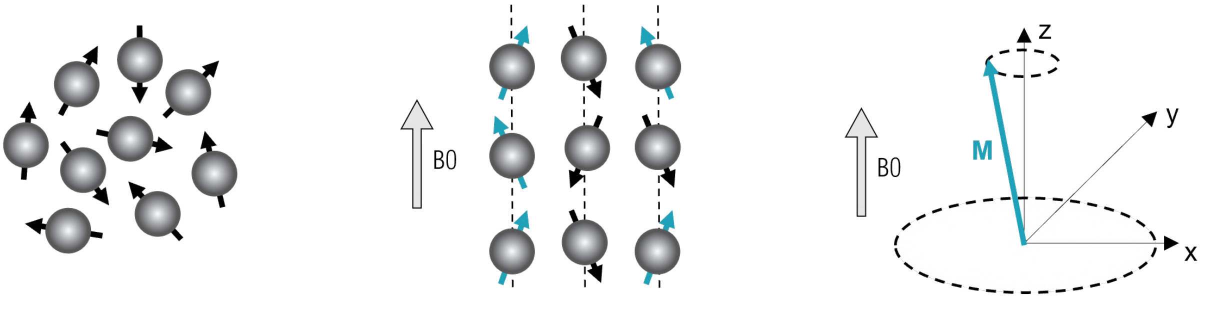

Figure 1.2: Behaviour of a sample when placed inside a strong magnetic field: **(Left)** Initially, the nuclear magnetic moments are randomly oriented. **(Center)** Once the sample is placed inside a strong magnetic field, the nuclear magnetic moments gradually align either with the field or against it. **(Right)** The slightly preferred alignment along the direction of the field results in a single magnetization vector M, represented in blue. Adapted from [9].

Due to the way the scanner coils are arranged, changes in the net magnetization are only detected in the plane orthogonal to the $B_0$ axis (referred to as the transverse plane). An oscillatory magnetic field $B_1$, produced by radiofrequency coils, is briefly applied perpendicular to the static magnetic field

$B_0$ and causes the net magnetization to tip away from its initial alignment, onto the transverse plane (excitation). The net magnetization does not persist indefinitely in the transverse plane and eventually decays into its original state due to two relaxation processes that occur simultaneously - $T_1$ and $T_2^{(*)}$ relaxation (Figure 1.3 illustrates the excitation and relaxation processes of the net magnetization vector). Relaxation causes the net magnetization to vary with time and generate its own time-varying magnetic fields. Consequently, time-varying currents are induced in a nearby receiver coil as a manifestation of Faraday's Law of Induction. The resulting oscillating signal decays under an exponential envelope, commonly referred to as a free induction decay (FID) [9], as shown in Figure 1.3.

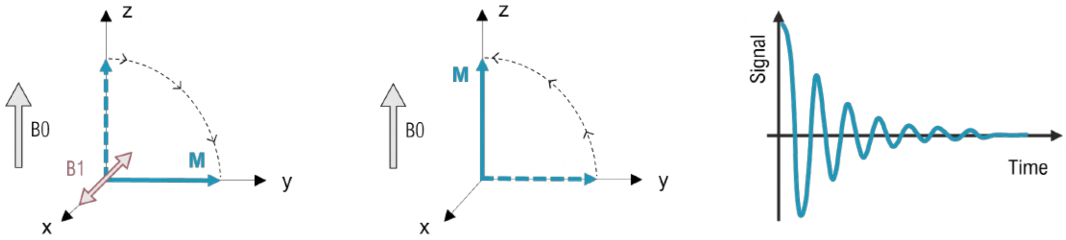

Figure 1.3: Schematic representation of the MRI **(Left)** excitation and **(Center)** relaxation phenomena in a rotating reference frame. The brief application of a $B_1$ pulse tips the magnetization onto the transverse plane, which eventually returns to the initial state. **(Right)** Free induction decay.

Since its initial introduction in the clinical environment in the late 1970s, MRI has rapidly become a widely accepted imaging modality to provide information regarding anatomical structures and, more recently, biological function [10]. Other noninvasive techniques for the assessment of human brain function, such as electroencephalography (EEG) and magnetoencephalography (MEG) also provide a measurement of neuronal activity. However, these specific techniques are limited by sensitivity, localization and spatial resolution issues [11]. Additional current methods of human functional brain imaging rely on indirect measurements of neuronal activity, related to blood flow, oxygenation or metabolic activity. The most common functional brain imaging technique is functional MRI.

### 1.2.2 The BOLD contrast

fMRI has offered unprecedented advances in our understanding of human brain function since the early 1990s, when the BOLD principle was first described by Ogawa and colleagues [12]. This functional imaging technique mostly relies on gradient recalled echo (GRE) sequences, due to their sensitivity to variations in the $T_2^*$ decay time. The typical structure of an fMRI experiment is represented in Figure 1.4.

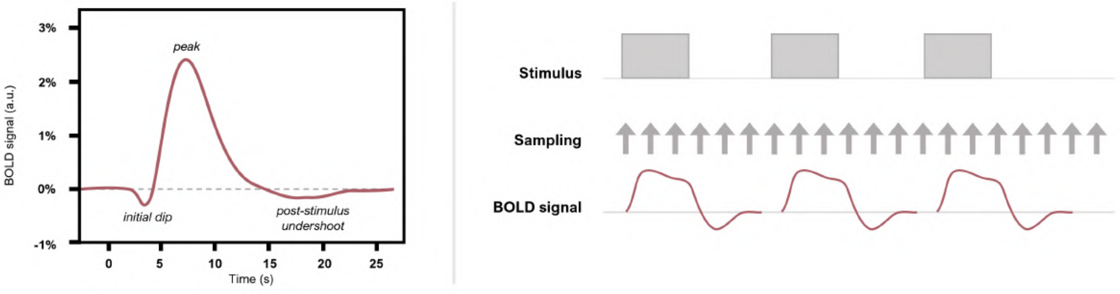

Figure 1.4: **(Left)** Canonical hemodynamic response function (HRF) reflecting the nature of the BOLD signal. **(Right)** Schematic representation of a block-design fMRI paradigm. Adapted from [13].

The BOLD effect is the basis for most fMRI studies done today to investigate the patterns of activation in the working human brain [14]. Task-based fMRI experiments, particularly, are widely used to study the functional activities and cognitive behaviours of the brain based on task-induced stimuli [15].

The BOLD contrast is not a direct measure of neuronal activity but rather results from the sensitivity of the MR signal to local changes in perfusion and metabolism of brain tissue (see Figure 1.5).

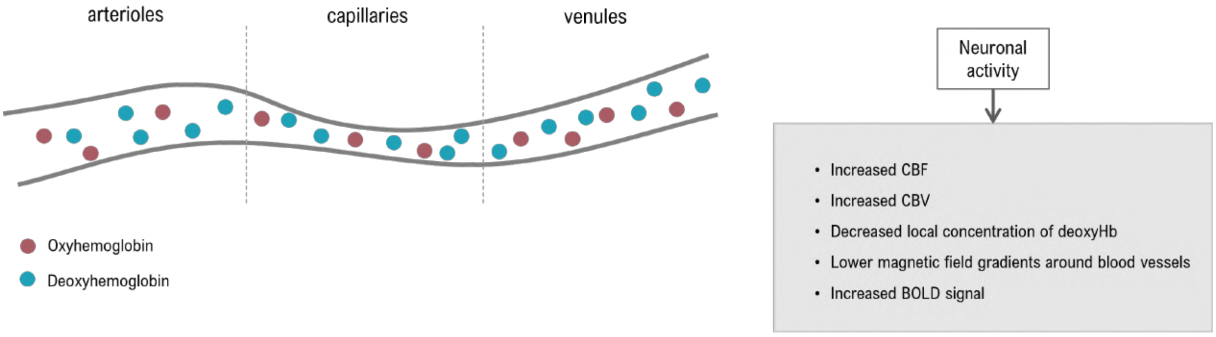

Figure 1.5: Schematic diagram illustrating the hemodynamic variables that change during neuronal activity. Adapted from [13].

Through neurovascular coupling mechanisms, a localized increase in neuronal activity causes vasodilation and a consequent increase in cerebral blood flow (CBF) and cerebral blood volume (CBV), as a response to the increased oxygen demand. However, the cerebral metabolic rate of oxygen consumption (CMRO$_2$) does not increase as drastically as the amount of oxygen being supplied. This results in a reduction in the overall concentration of deoxyhemoglobin, which has paramagnetic properties whereas oxyhemoglobin is diamagnetic. The presence of paramagnetic deoxyhemoglobin molecules leads to local magnetic susceptibility gradients, causing a faster dephasing of excited spins and ultimately shortening the T$_2^*$ value [16]. Therefore, neuronal activity inherently increases the value of T$_2^*$ and, consequently, increases the BOLD signal. The signal intensity at each time point $t$ can be described as

$$S(t) = S_0 e^{-t/T_2^*} \tag{1.1}$$

where $S_0$ denotes the initial magnetization after excitation.

### 1.2.3 Physiological noise fluctuations

The fMRI signal relies on signal changes that result from blood oxygenation or blood flow fluctuations in the activated regions of the brain. However, pulsatility of blood flow within the brain, respiration-induced changes in the magnetic field and motion artifacts (also due to respiration) may cause substantial undesired perturbations of the fMRI signal [17].

Cardiac pulsatility generates inflow effects in and around blood vessels, making the added noise rather localized in tissue regions close to large arteries and draining veins, such as the sagittal sinus or the circle of Willis . Respiration effects are often more spatially dispersed, since they originate from thoracic modulation of the magnetic field or from bulk head movements [17]. Additionally to the main components related to the respiratory and cardiac cycles, the BOLD signal also inevitably contains physiological fluctuations related to low frequency changes of respiration rate, cardiac rate and vasomotion, that interact with each other and result in changes in arterial CO$_2$, blood pressure and vascular tone [8].

The main cardiac-related components of the fMRI signal have frequencies of about 1 Hz, whereas respiration-related components typically fluctuate around 0.3 Hz [18]. Both of these frequency values are relatively high when compared to standard evoked BOLD responses, where the hemodynamic process acts as a low-pass filter with a cuttoff frequency below 0.25 Hz [8][19].

Figure 1.6 shows the model timecourses for both the cardiac and respiratory cycles, and the respective frequency spectra. The described noise components have demonstrated to be comparable to the signals of interest, thus degrading the sensitivity to neuronal activation detection and compromising the statistical significance of event-related analysis. Because of its significant negative impact on fMRI data, several methods have been developed for physiological noise removal.

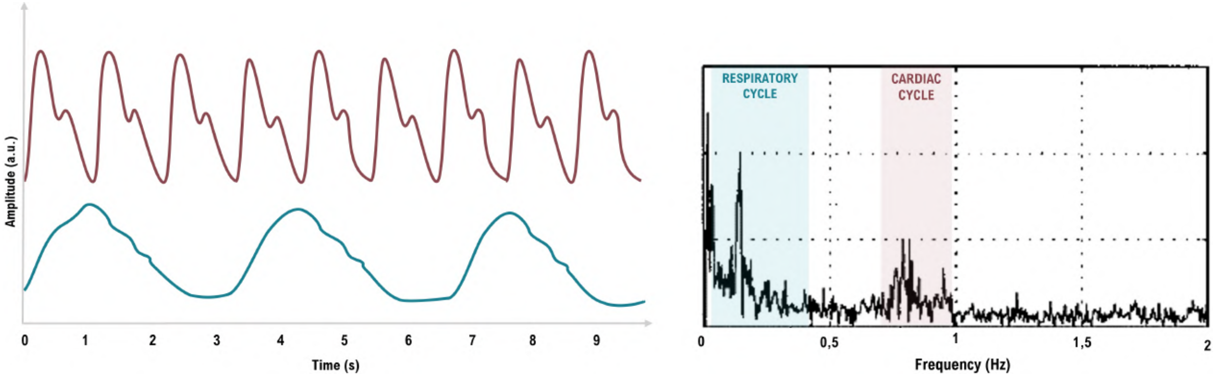

Figure 1.6: **(Left)** Model timecourses for the cardiac cycle in red (∼1 Hz) and the respiratory cycle in blue (∼0.3 Hz). **(Right)** Power spectrum of the respiratory cycle - highlighted in blue - and cardiac cycle - highlighted in red. Adapted from [17].

## 1.3 State-of-the-Art

### 1.3.1 Ultra-high field MRI

The increase in strength of the static magnetic field ($B_0$) has had a huge impact in the field of MRI. Initial experiments were performed at field strengths of 1.5 Tesla, which were eventually followed by high field strengths of 3-4 Tesla and ultra-high field strengths of 7 Tesla and beyond [2].

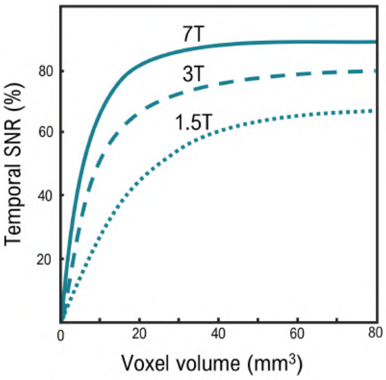

Figure 1.7: Temporal signal-to-noise ratio (tSNR) for three different field strengths as a function of voxel volume for $T_2^*$-weighted imaging. Ultra-high field strenghts (7T) show improved sensitivity overall, and particularly for smaller voxel volumes, thus making it ideal for exploring brain structures at the mesoscopic scale. Adapted from [20].

Ultra-high field MRI provides several advantages for neuroscience, as well as some challenges. The increased field strengths result in an increase in the available magnetization, and ultimately improve the signal-to-noise ratio (SNR). Ultra-high field strengths are being successfully used in conventional spatial resolution functional imaging ($>$1mm), allowing the exploration of brain function and macroscopic organization at an unprecedented level of detail [21].

Ultra-high field MRI is additionally used to characterize a new organization level of the human brain at the mesoscopic scale, by delineating laminar and columnar cortical structures, which typically require voxel sizes below 1 mm. Very high spatial resolutions ($<$1 mm) usually come at the cost of low temporal resolution, resulting in a slow sampling rate of the hemodynamic brain response and subsequent loss of functional specificity. Additionally, a slow acquisition of the MRI signal results in prolonged scan times, which is not only unpleasant for the subjects but also increases the chances of artifacts due to motion. For these high spatial resolutions, SNR and sensitivity remain a challenge. However, these can be improved with the use of surface coils [22], at the expense of reduced spatial coverage.

### 1.3.2 Line-scanning fMRI

As introduced in Section 1.3.1, the increased availability of ultra-high field human MRI scanners and the development of new fMRI acquisition techniques have made it possible to achieve sub-millimeter spatial resolutions and, therefore, allow the non-invasive assessment of laminar structures that are essential for functional processing in humans [23].

Human cortical thickness varies between 1 and 4.5mm, averaging at approximately 2.5mm overall [24]. Thus, to resolve brain activation at a laminar scale, the sub-millimeter spatial resolution provided by ultra-high field strengths is of paramount importance.

Additionally, a very high temporal resolution is necessary to accurately locate microvessel responses and characterize the distribution of blood flow across the cortical depth [25]. Different methods have been developed to achieve higher temporal resolutions, such as undersampling techniques and parallel imaging. However, to reach a combination of very high temporal and spatial resolutions, specific strategies need to be adopted.

One promising technique that achieves the required spatial and temporal resolutions for laminar studies is line-scanning fMRI. This method sacrifices volume coverage and resolution across the cortical surface, however, it has the potential to achieve very high spatial and temporal resolutions (200 μm and 100 ms, respectively) using ultra high-field 7T fMRI [26].

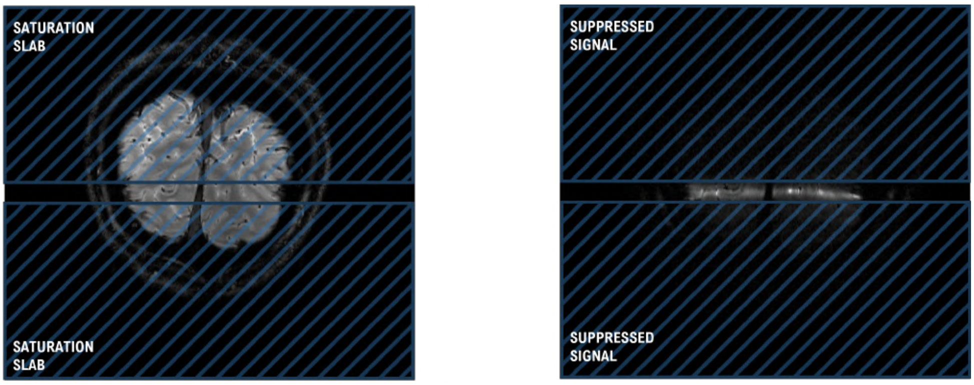

Figure 1.8: Schematic representation of a line-scanning fMRI acquisition. Outer volume suppression (OVS) is achieved through the placement of saturation slabs outside the line of interest to suppress unwanted signal.

Line-scanning fMRI, as the name suggests, consists of acquiring only one line of fMRI data. Two saturation pulses are positioned outside the relevant cortical area to suppress the MRI signal, the phase-encoding gradient in the direction perpendicular to the line is turned off [1] and the signal is acquired into a single line profile across the cortical depth (see Figure 1.8). The slice selection step during the radiofrequency excitation, combined with the application of saturation pulses, ensure that the signal is predominantly coming from the relevant cortical area [27].

Line-scanning fMRI capitalizes on high resolution spatial and temporal information of BOLD responses across cortical depth. Isolating and characterizing microvessel spatiotemporal behaviour clarifies microvascular function in health and disease, and provides important insights on laminar information flow and microvascular pathophysiological mechanisms of certain brain disorders [25].

Moreover, characterizing the microvascular hemodynamics through line-scanning could potentially help neuroscientists understand neurovascular coupling and how capillary blood flow and oxygen distribute across cortical layers to meet the local metabolic demand [1]. This knowledge will help neuroscientists but will also translate to clinical neuroscience, since the cortical processing unit and its columnar and laminar components may be altered in a wide range of clinical conditions [2].

### 1.3.3 Strategies for denoising fMRI data

To benefit from the increased BOLD contrast at higher field strengths, thermal noise should be larger in magnitude than non-neuronal physiological fluctuations, which can be achieved by reducing the voxel size. However, the increased spatial resolution turns the fMRI time series more sensitive to physiology and motion-related fluctuations [8].

As described in Section 1.2.2, the BOLD signal is an indirect measure of neuronal activity that arises from a complex mixture of neuronal, metabolic and vascular processes. This signal is significantly corrupted by non-neuronal fluctuations of instrumental, physiological or subject-specific origin. Techniques targetting the identification and removal of these confounds include data-driven approaches and methods that require external recordings. Some commonly used methods will be described in this section and are summarized in Figure 1.9.

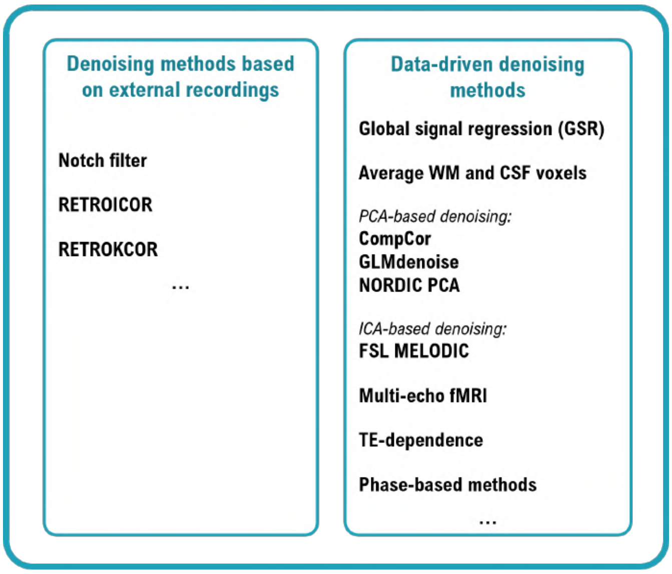

Figure 1.9: Summary of the fMRI denoising methods established for 2D and 3D data covered in this work.

### *Notch filter*

Most current MR scanners include equipment for physiological monitoring of respiration and cardiac pulse. Typically, respiration is measured through a pneumatic belt placed around the subject's abdomen, whereas the cardiac pulse is measured by placing a pulse oxymeter or a photoplethysmograph (PPG) in the pad of a finger. Specific peaks of the frequency spectra of these external recordings correspond to the fundamental frequencies of the cardiac and respiratory fluctuations, and therefore, notch filters can be implemented at these frequencies to remove the physiological fluctuations from the acquired fMRI signal.

However, notch filtering will also remove any BOLD fluctuations of interest that may exist at those frequencies. Due to this disadvantage, multiple modelling approaches have been developed to retrospectively reduce the effects of the cardiac cycle and respiratory fluctuations.

### *RETROICOR and RETROKCOR*

The most common of the modelling approaches proposed is RETROICOR, which assumes that the fMRI time series in a voxel is corrupted by quasi-periodic additive noise related to the cardiac and respiratory cycles. RETROICOR uses external recordings of the cardiac and respiratory states monitored during the scan and models these physiological fluctuations as low-order Fourier series with time-varying cardiac and respiratory phases, as shown in Equation 1.2.

$$y_\delta(t) = \sum_{m=1}^{M} a_m^c cos(m\phi_c(t)) + b_m^c sin(m\phi_c(t)) + a_m^r cos(m\phi_r(t)) + b_m^r sin(m\phi_r(t)) \tag{1.2}$$

where y$_\delta(t)$ is the physiological noise component of the mathematical model of the data, the superscripts on the coefficients $a$ and $b$ refer to the cardiac or respiratory function and $\phi_c(t)$ and $\phi_r(t)$ are the phases of the respective cardiac and respiratory cycles [17]. The physiological noise models obtained for both cycles are then fit to the data as nuisance regressors in a general linear model (GLM) analysis [8].

Thus, the fMRI data can be corrected by subtracting y$_\delta(t)$ from the acquired signal y$(t)$ (see Figure 1.10).

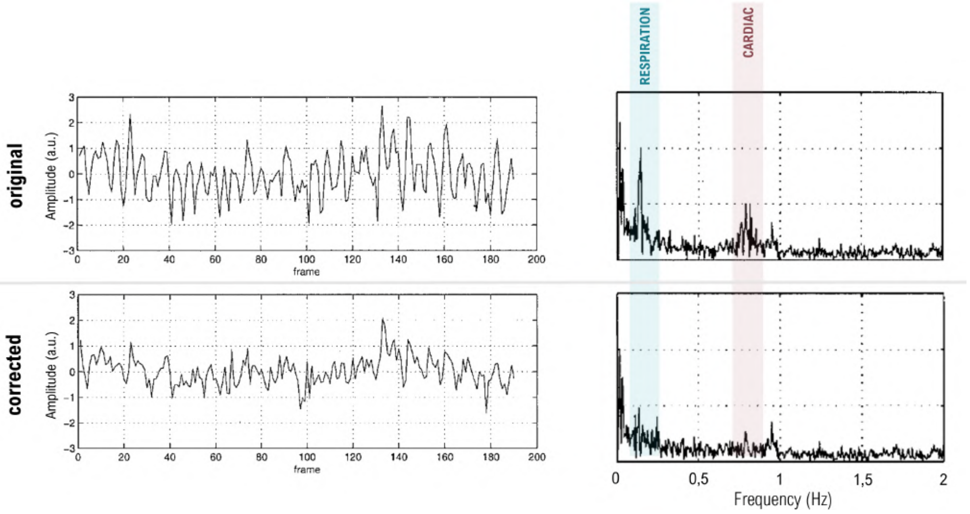

Figure 1.10: **(Left)** Time series without (top) and with (bottom) RETROICOR correction. **(Right)** Frequency spectra of time series without correction (top) and with respiratory and cardiac corrections (bottom). In this example, the cardiac and respiratory spectra are resolved with peaks near 0.8 and 0.15 Hz, respectively. Adapted from [17].

Previously to RETROICOR, a method later referred to as RETROKCOR was proposed by Hu et al. in 1995 [28], which fits a set of Fourier terms defined from physiological recordings directly to the k-space, whereas RETROICOR operates in the image space by fitting and reducing the physiological noise in each voxel time series independently. Therefore, RETROICOR overcomes some of the drawbacks of RETROKCOR, since it avoids the calculations in the magnitude and phase k-space data for each individual channel.

### *Global Signal Regression (GSR)*

One of the most straightforward denoising methods is global signal regression (GSR) and it is based on the assumption that any process that is detected across the entire brain cannot be linked to neuronal activity. The average fMRI signal across all the voxels in the brain is computed and removed from the data, as it represents all the processes that confound the BOLD signal [8].

### *CSF and White Matter regressors*

Similarly, nuisance regressors that explain non-neuronal activity can be generated from the averaged signal of white matter (WM) and ventricular cerebrospinal fluid (CSF) voxels, which are usually identified through segmentation algorithms as illustrated in Figure 1.11. It is generally thought that fluctuations of neuronal origin are not significantly present in these tissues, but rather only physiological and hardware noise, which contaminates grey matter (GM) as well [29]. Using the signals from these tissues as nuisance regressors has become fairly common in both resting state and task-based fMRI, however, some consider erroneous to overlook white matter fMRI activation strictly as a confound component [30].

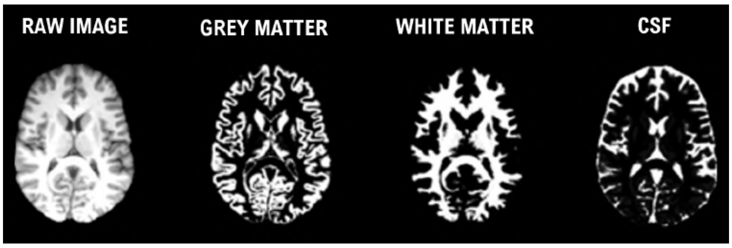

Figure 1.11: An example of brain tissue segmentation by FSL's automated segmentation toolbox (FAST) - probability maps of GM, WM and CSF. Adapted from [31].

Alternatively to averaging isolated signals, several **principal component analysis (PCA)** based methods have been developed for denoising the fMRI signal.

### *CompCor*

CompCor is a widely-used noise modelling method based on a PCA decomposition of voxels where no BOLD fMRI signals of neuronal origin are expected. This approach defines multiple nuisance regressors from the principal components of WM and CSF voxels, instead of using the average signal of those tissues and without requiring external monitoring of physiological fluctuations [32]. PCA decomposition is also commonly used to generate nuisance regressors from the PCs of voxels located on the outer edges of the brain to account for motion-related and respiration-induced signal fluctuations.

### *GLMdenoise*

Additionally, Kay and colleagues have developed GLMdenoise, an automated technique for denoising task-based fMRI [33]. This approach identifies task-unrelated voxels from an initial model fit and uses them in a PCA decomposition to derive noise regressors, that can then be used in a GLM analysis of the data. GLMdenoise does not require any external physiological monitoring, thus it can be applied retrospectively to any existing dataset.

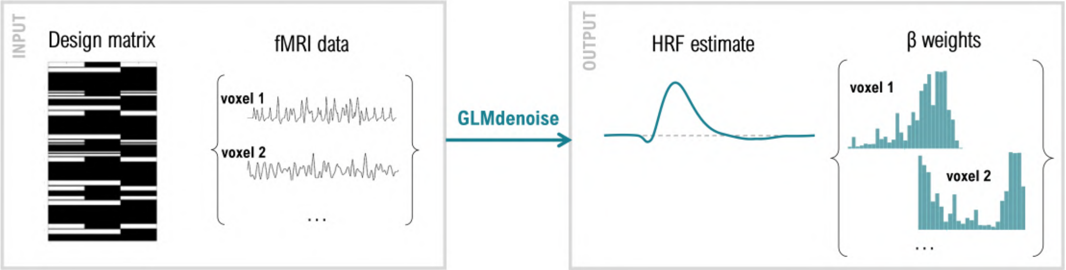

Figure 1.12: Schematic representation of GLMdenoise - inputs and outputs. GLMdenoise takes as input a design matrix indicating the experimental design and an fMRI dataset consisting of multiple runs, and returns as output an estimate of the hemodynamic response function (HRF) and BOLD response amplitudes (beta weights). Adapted from [33].

### *NOise Reduction with DIstribution Corrected (NORDIC) PCA*

An alternative PCA-based denoising technique is the recently proposed NOise Reduction with DIstribution Corrected (NORDIC) PCA framework, that relies on a singular value decomposition (SVD) to ultimately improve the SNR, without compromising any information [34]. Using locally low-rank (LLR) PCA, NORDIC ensures the elimination of independent, identically distributed, zero-mean Gaussian entries, thus removing components that cannot be distinguished from Gaussian thermal noise. A flowchart illustrating this method is included in Figure 1.13.

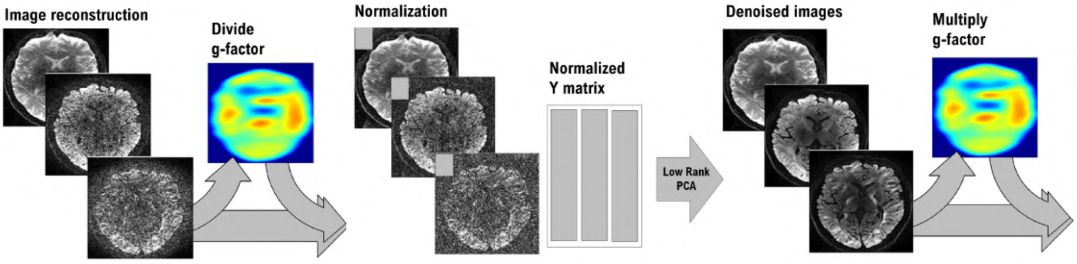

Figure 1.13: Flowchart of the NORDIC algorithm. In this example from Moeller et al. (2021), NORDIC PCA is applied to diffusion-weigthed MRI data obtained from an accelerated parallel imaging acquisition. Adapted from [34].

In the original application of NORDIC PCA to fMRI data (described in [35]), the authors acquired 2D slice selective fMRI data accelerated through parallel imaging. Due to the undersampling pattern intrinsic to parallel imaging, the noise within the data undergoes a spatially varying amplification characterized by the geometry-factor (g-factor). From the g-factor maps obtained, the complex fMRI data is normalized, ensuring zero-mean spatially identical noise. For LLR processing, a fixed patch of g-factor corrected complex fMRI data $(Y)$ is extracted for each volume. In essence, the denoising problem consists of recovering matrix $X$, based on the model

$$Y = X + N \tag{1.3}$$

where N is additive Gaussian noise.

The noisy data $Y$ is subjected to a singular value decomposition determined as $Y = USV^H$ (see Figure 1.14), where $U$ and $V$ are unitary matrices and $S$ is a diagonal matrix containing the ordered singular values. Any singular value below a predetermined threshold $\lambda_{thres}(t)$ is replaced with zero (hard thresholding), while the other singular values are unaffected. This threshold can be selected either empirically - based on which components exhibit relevant spatio-temporal features, - or it can be selected according to the largest singular value of the noise matrix $N$ [34]. Using the new diagonal matrix $S_{thresh}$, the low-rank estimate of $Y$, $X$, is given as $Y_L = US_{thresh}V^H$.

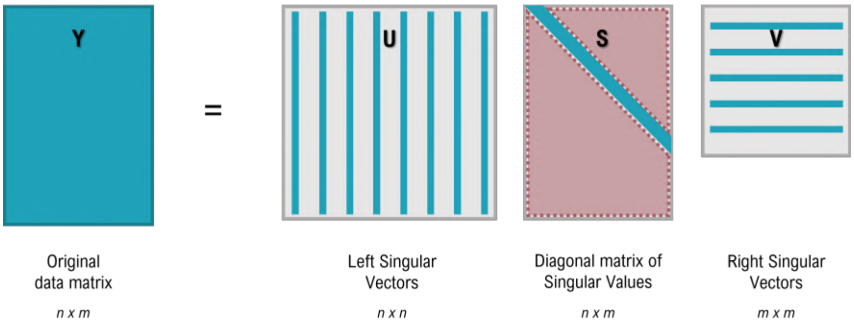

Figure 1.14: Schematic representation of a singular value decomposition.

### ***ICA-based denoising***

Other methods for denoising fMRI are based on **independent component analyses (ICA)**, which can be performed in **FSL's MELODIC** [36], for example. The success of these methods relies on accurately labelling independent components (IC) that can be related to neuronal mechanisms or to noise sources. This classification can be manual, semi-automated or automated. Manual classification is the gold standard, but it is time consuming nonetheless, lacks in reproducibility and requires expertise [37]. Due to this, automated and semi-automated classification algorithms that label the components based on their temporal and spatial features have emerged.

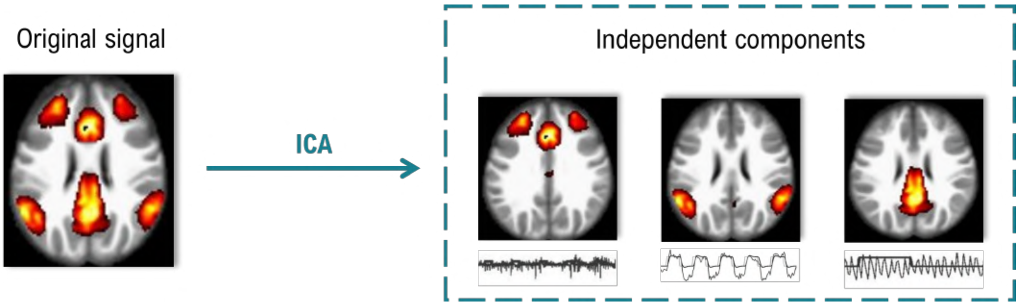

Figure 1.15: Schematic illustration of spatial ICA of fMRI data. Adapted from [38].

### ***Multi-echo fMRI***

In most fMRI protocols, the application of a radiofrequency excitation pulse is followed by the acquisition of a single image at a certain optimal echo time (TE), which depends on various factors, such as field strength, target tissue and target relaxation constant. Typically, TE is set as close as possible to the $T_2^*$ of grey matter, in order to maximize the sensitivity to BOLD fluctuations [8]. However, different voxels have different $T_2^*$ values depending on tissue properties and changes in the local magnetic field [39] and thus, $T_2^*$ varies considerably across the brain.

To address the spatial variation of $T_2^*$, the sampling strategy can be modified to allow the acquisition of multiple images in rapid succession at different predetermined TEs - multi-echo fMRI. By covering a larger range of potential $T_2^*$ values, multi-echo fMRI improves BOLD contrast-to noise ratio (CNR). However, the highest contrast for different brain regions will be spread over the different TE images [40]. Therefore, rather than being analyzed individually, multi-echo data can be combined into a single image. For this purpose, different weighting strategies have been suggested based on global or local estimates of $T_2^*$ (where $T_2^*$ values can be estimated from the data based on how signals scale across echoes) or the measure of voxel-wise CNR [41]. Ultimately, the weighted combination of multiple echoes results in significant artifact reduction and improves BOLD sensitivity and CNR [40].

Similarly to Equation 1.1, the signal intensity at each TE can be described as $S(TE) = S_0 e^{-TE/T_2^*}$. Therefore, data acquired with a very short TE1 has minimal $T_2^*$-weighting and high sensitivity to fluctuations in $S_0$, and can be used as a nuisance regressor for denoising the remaining echoes.

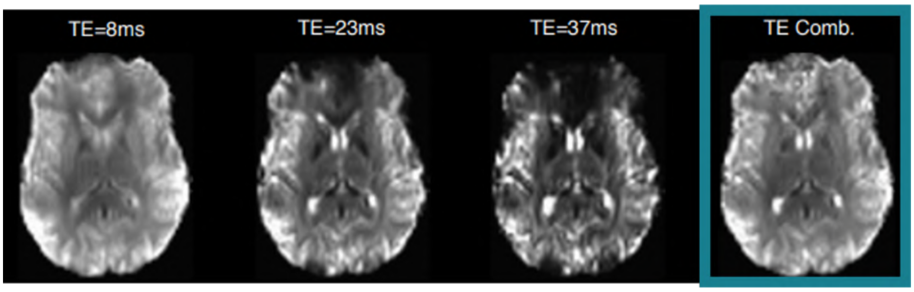

Figure 1.16: Combination of echo images from a multi-echo fMRI acquisition at 7T. The optimal echo combination weights towards early TE signals in regions with shorter $T_2^*$ to counteract signal dropout artifacts. Adapted from [39].

### ***TE-dependence assessment***

Additionally, studying the TE-dependence of a signal (i.e., how a signal evolves across the different images of a multi-echo fMRI acquisition [39]) can be used to differentiate BOLD from non-BOLD signals, allowing the latter to be removed without any conventional noise modelling [42].

As described in Section 1.2.2, the cerebrovascular hemodynamics of blood oxygenation modulate $T_2^*$ due to changes in concentration of deoxyhemoglobin, but, in practice, the BOLD response to neuronal activation also affects blood flow and volume, thus changing the amount of available nuclear spins and, consequently, modulating $S_0$ as well [39]. However, BOLD-related changes modulate $T_2^*$ much more substantially than $S_0$, making $S_0$ a reliable indicator of artifacts such as head motion, CSF fluctuations and cerebrovascular pulsatility. Therefore, a signal time series with a high $T_2^*$ and low $S_0$ contributions is most likely to be related to changes in blood oxygenation, and thus functional brain activity, whereas components with higher $S_0$-weighting, independently of its correlation with a $T_2^*$ mono-exponential decay, can be considered to be associated with artifacts (see Figure 1.17).

This principle can be applied not only to single-voxel time series across TEs, but also to averaged region-of-interest (ROI) signals and independent components obtained through ICA decompositions. By studying the TE-dependence or independence of fMRI signals, it is possible to distinguish neurally-related activity from artifacts.

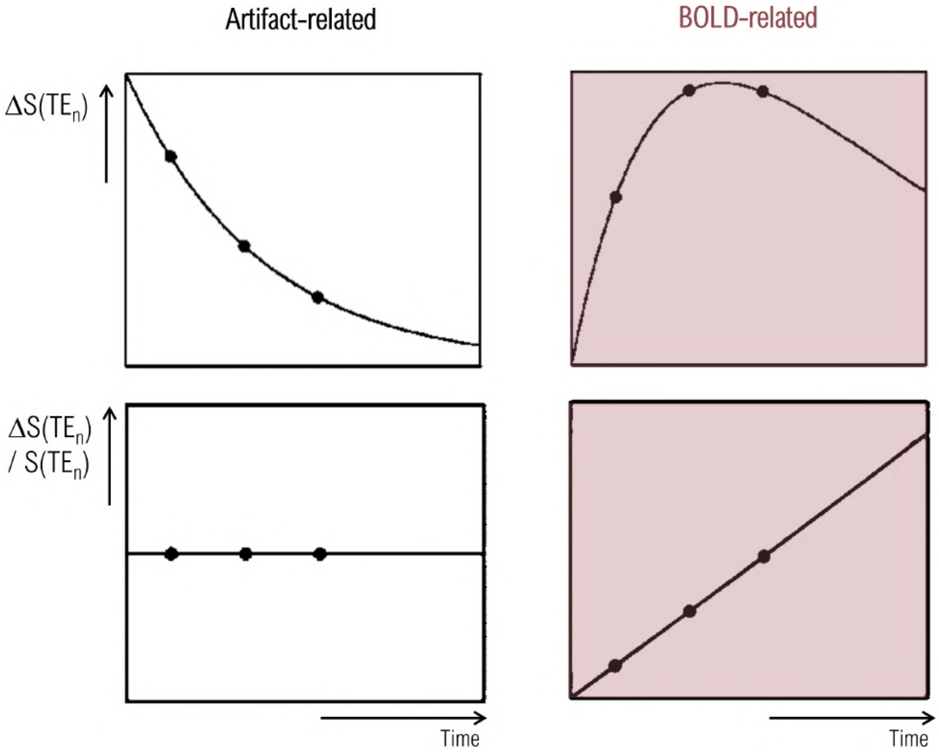

Figure 1.17: TE-independence of non-BOLD versus TE-dependence of BOLD fMRI signal changes. **(Top)** Computed difference in signal at different TEs due to (left) artifact-related changes in $S_0$ and (right) BOLD-related changes in $R_2^*$. **(Bottom)** Percent signal change at different TEs for (left) artifact-related changes in $S_0$ and (right) BOLD-related changes in $R_2^*$. Adapted from [42].

### ***Phase-based methods***

Although fMRI is initially acquired as complex-valued image pairs (see Figure 1.18), the denoising techniques previously mentioned only use magnitude data. However, the phase signal contains relevant biological information about magnetic susceptibility changes in and around vasculature in response to neuronal activity and is useful for the identification of different tissue types [43]. Therefore, considering both magnitude and phase changes improves the mapping of the BOLD response in terms of sensitivity and spatial specificity.

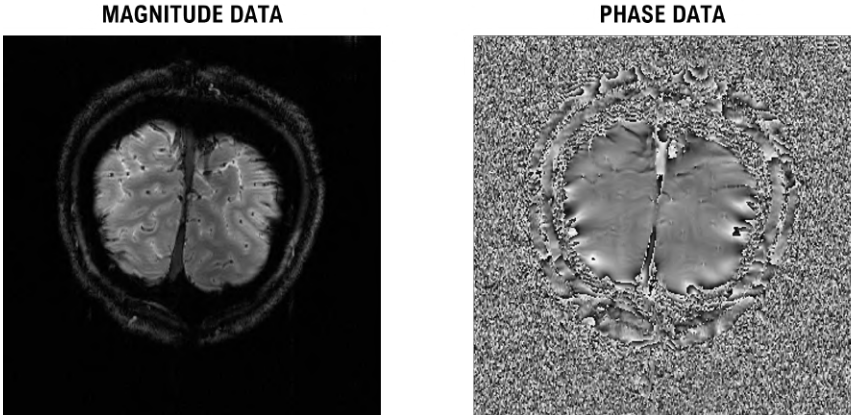

Figure 1.18: **(Left)** Magnitude and **(Right)** phase images of a representative MRI acquisition.

Large vessels can be several millimeters away from the primary site of neuronal activity [8], thus hampering spatial localization of neuronal activation and negatively impacting high-resolution fMRI studies [44]. Due to the sensitivity of the phase signal to blood flow - particularly within large vessels [8], - phase data can be used to reduce the macrovascular weighting of the fMRI signal by relying on phase regression [44]. With this method, large-vessel BOLD contamination is estimated from the phase data, and is then subtracted from the magnitude data, reducing the macrovascular bias intrinsic to BOLD fMRI without using any additional venous identification [45].

The steps included in an fMRI preprocessing pipeline and their relative order should be decided according to the characteristics of each dataset. The optimal denoising pipeline for any given data will depend on the MR acquisition parameters (type of sequence, voxel size, TR), subject-specific traits that modulate the type of noise included in the data (head motion, respiration pattern, heart rate variability, blood pressure), and the type of experiment (resting state or task-based fMRI, with a block or event-related design) [8].

## 1.4 Goals and approach

This study focused on line-scanning fMRI data and its intrinsic BOLD and non-BOLD signal fluctuations. The main goals of the presented work are:

1) To highlight the great potential of line-scanning fMRI for the future of neuroscience and clinical applications - the fMRI technique is explained in detail as well as the data acquired, its advantages and its current challenges.

2) To review the existing methods for denoising 2D and 3D fMRI data - understand their implementation, advantages and drawbacks.

3) To assess the validity of the application of different denoising methods to line-scanning fMRI data - some already well-established for 2D and 3D fMRI data and other more recent techniques - for the identification of different signal sources and noise within the original data.

4) To evaluate the quality of the line-scanning fMRI data after denoising - the performance of the different algorithms is qualitatively and quantitatively analyzed.

## 1.5 Thesis outline

This report is divided into four main chapters. In the present chapter, Chapter 1, the main concepts behind the topic of this study are described, as well as the problem at hand and the approach adopted to address it. Chapter 2 covers the materials and methods utilized during this study, including hardware equipment, data acquisition techniques, computational frameworks for data analysis and noise removal and the metrics used to evaluate said frameworks. In Chapter 3, the physiological and fMRI data acquired are characterized in detail and the performances of the multiple noise removal algorithms tested are compared. Lastly, Chapter 4 outlines the main contributions and limitations of this study, followed by some suggestions to be implemented in future work.

# Chapter 2

# Methods

## 2.1 Methods overview

The methodology used in all stages of this project is outlined in Figure 2.1 and described in greater detail throughout the present chapter. Firstly, the acquisition protocol of fMRI and physiological data is explained, covering the hardware and software tools required (see Section 2.2). This is then followed by a description of the techniques selected for data analysis (see Section 2.3) - in particular, the frequency- and time-domain characteristics of the acquired fMRI and physiological data are examined. At last, the processing pipeline used for identifying non-BOLD fluctuations within the fMRI data is described and the methods included are explained.

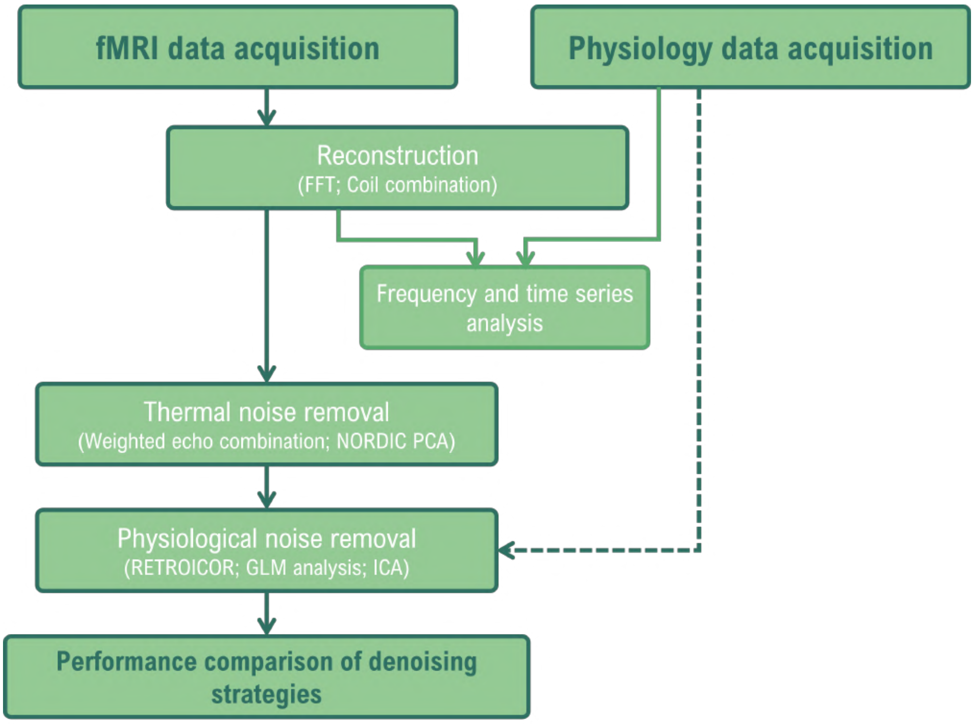

Figure 2.1: Flow diagram summarizing the protocol followed to acquire and process the line-scanning fMRI data and the physiological recordings.

## 2.2 Data acquisition

### 2.2.1 MRI data acquisition

Four healthy volunteers were scanned at the Spinoza Centre for Neuroimaging on a 7T Philips Achieva MRI scanner, equipped with a 2-channel transmit and 32-channel receive head coil from Nova Medical (see Figure 2.2). All participants were screened prior to the experiment in order to ensure MR compatibility.

Figure 2.2: **(Left)** Nova Medical Head Coil 2TX/32RX. **(Right)** Philips Achieva 7T MRI scanner.

Line-scanning fMRI data was acquired using a modified 2D multi-echo gradient-echo (ME-GRE) sequence, illustrated in Figure 2.3. Both respiratory and cardiac fluctuations were simultaneously recorded using external hardware (see Section 2.2.4). Two slab-selective saturation radiofrequency (RF) pulses, with a duration of 7.76 ms, were applied for outer volume suppression (OVS) before slice excitation [1]. Fat suppression was applied before the saturation pulses using the Philips implementation of spectral presaturation with inversion recovery (SPIR). Five echoes with an echo spacing of $\Delta$TE = 8ms (TEs = 6, 14, 22, 30, 38 ms) were acquired after slice excitation. The pre-pulses (fat suppression and OVS) were repeated every TR and the phase-encoding gradient in the direction perpendicular to the line of interest was turned off [25], resulting in the the projection of all the signal into a single line profile.

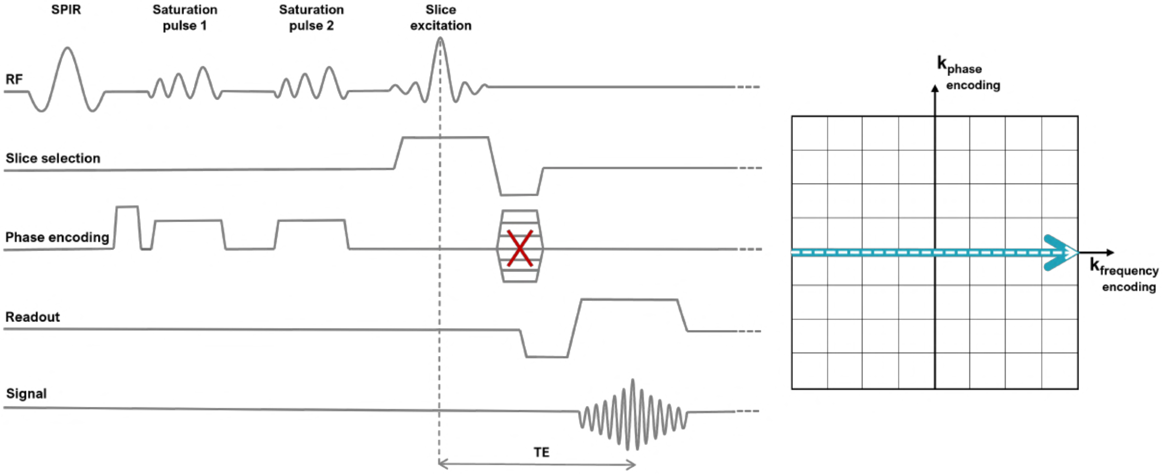

Figure 2.3: **(Left)** Schematic representation of the multi-echo gradient-echo line-scanning sequence. Two OVS pulses suppress the signal outside the area of interest and the remaining signal is projected onto a line profile. Five echoes were acquired after excitation. **(Right)** Sampling pattern of k-space characteristic to line-scanning - repeated acquisition of $k_{FE}=0$ at every TR. Adapted from [1].

The planning of each experiment included placing the slice and saturation slabs in such a way that the resulting line was positioned within the visual cortex for detecting neuronal activation during visual tasks. The line-scanning acquisition in each session was preceded by the acquisition of a structural MRI slice with no saturation pulses, and $B_0$ shimming was performed before each run to correct any unwanted inhomogeneities of the static magnetic field $B_0$, which can lead to erroneous voxel localization and spectral broadening [46]. $B_0$ shimming relies on the superposition principle by creating and adding a corrective magnetic field to $B_0$, in order to homogenize the original static magnetic field distribution. Although hardware imperfections exist, the majority of the $B_0$ field inhomogeneities found in vivo are induced by the sample itself, i.e. the subject, due to the different magnetic susceptibilities of brain tissues [46]. Figure 2.4 shows the placement of the shimming ”box” for one of the scanning sessions and the frequency distribution of $B_0$ before and after applying the correction.

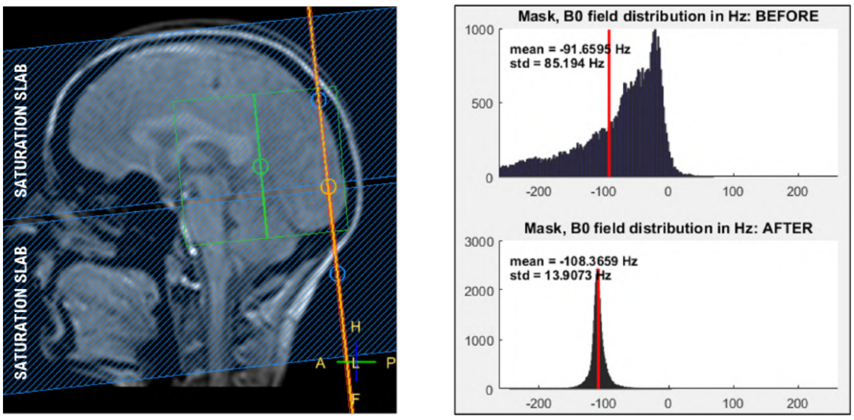

Figure 2.4: **(Left)** Overview of the planning of the line-scanning fMRI acquisition: Sagittal view of the placement of the saturation pulses and the acquired slice, represented in blue and orange, respectively. The green rectangle represents the $B_0$ shimming ”box”. **(Right)** $B_0$ field distribution before and after shimming.

The placement of the spatial saturation pulses ensures significant signal suppression outside the targetted line of interest (see Figure 2.5), and the resulting line-scanning data is defined as the projection of the signal from the entire slice with OVS slabs onto a line along the phase-encoding direction. The line is positioned across the two hemispheres and orthogonally to the cortical surface to minimize the presence of different tissues within the same voxel (partial volume effects) [26].

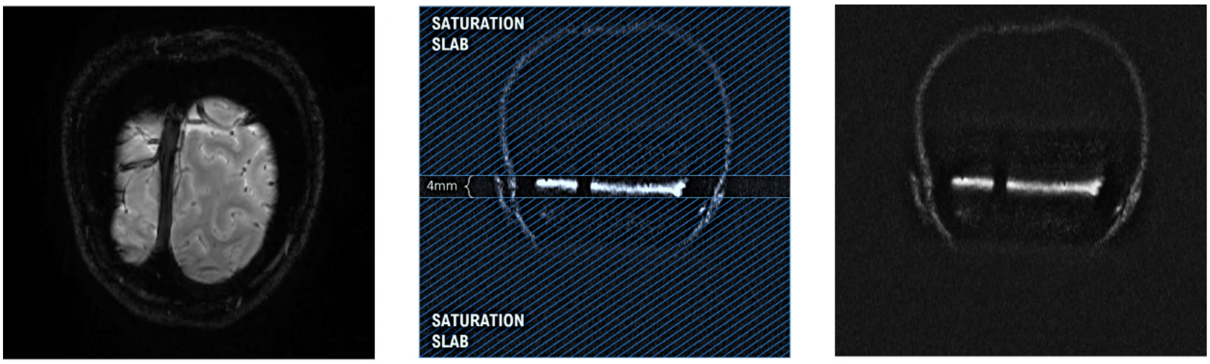

Figure 2.5: **(Left)** Acquired slice. **(Center)** Placement of OVS slabs to suppress signal from outside the line of interest. **(Right)** Saturation effect of the OVS slabs on the acquired slice with phase-encoding enabled. Adapted from [1].

For accurate physiological denoising, selecting an adequate TR is critical to correctly sample cardiac and respiration fluctuations within the fMRI data. Based on the characteristic frequencies of first-order respiration- and cardiac-related components (0.3 Hz and 1 Hz, respectively), the Nyquist principle stipulates that the fMRI sampling rate should be greater than 0.6 Hz (TR<1.6 s) and 2 Hz (TR<0.5 s) to prevent aliasing of the lowest order harmonics of the respiratory and cardiac cycles [8]. Therefore, a repetition time of 105 ms was selected for this study.

Thus, the parameters for the multi-echo line-scanning functional acquisitions were the following: TR = 105 ms, TE1 = 6 ms, echo spacing = 8 ms, flip angle = 16°, line spatial resolution = 250 µm, line thickness = 2.5 mm, line length = 180 mm (i.e. 720 voxels), line width (gap between the two saturation pulses) = 4 mm and 3200 time points (i.e. 336 seconds).

### 2.2.2 Task paradigm

One run of functional MRI data was acquired for each volunteer using a block design visual task consisting of a 20Hz black and white flickering checkerboard presented for 10 seconds, followed by 10 second rest periods (see Figure 2.6). Each session started with one dummy scan, to ensure the system was on a steady state before beginning acquisition, and included 16 task blocks, having a total duration of 336 seconds (3200 time points). Subjects were asked to fixate in the center of the checkerboard during the the ON condition to elicit strong BOLD responses in the primary visual cortex V1.

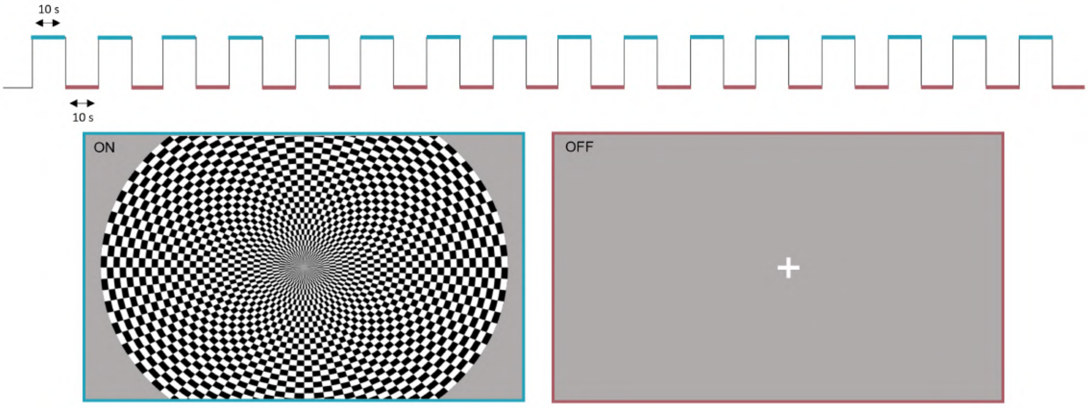

Figure 2.6: **(Top)** Visual task model - stimulus blocks for 10 seconds ON/OFF. **(Bottom)** Task description - ON condition with a 20Hz flickering checkerboard; OFF condition with grey screen and white cross.

The visual stimulus was presented on a MRI compatible 32” LCD BOLD screen from Cambridge Research Systems, placed behind the scanner bore. The participants were able to view the stimulus screen via an angled mirror mounted inside the head coil.

### 2.2.3 MRI data reconstruction

The reconstruction of the MRI data was performed offline with in-house software previously implemented using Matlab (Mathworks Inc.) and MRecon (Gyrotools). To combine the multi-channel line-scanning data, a weighted sum of squares (SoS) was calculated according to Equation 2.1.

$$S(x) = \frac{\sum_i^{N_c} w_i(x) * S_i(x)}{\sqrt{\sum_i^{N_c} |w_i(x)|^2}} \tag{2.1}$$

where S is the MRI signal and $N_c$ is the total number of channels (in this case, 32 channels).

The weight $w_i(x)$ for each channel was obtained using the tSNR per coil element, as well as coil sensitivity maps (Figure 2.7) obtained for each of the four subjects [1].

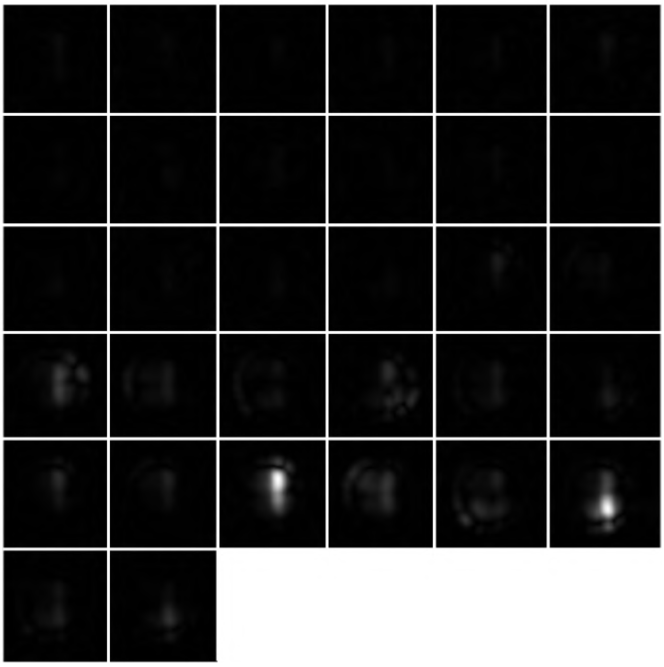

Figure 2.7: Coil sensitivity maps acquired for the 32 channels of a representative subject.

For each echo time (TE), the reconstructed line-scanning fMRI data can be described as a 720-by-3200 data matrix, in which each row represents the time series of the corresponding voxel. Because the MR signal starts to decay immediately after excitation due to relaxation processes, the multi-echo acquisitions show a gradual decrease in signal intensity throughout time as shown in Figure 2.8.

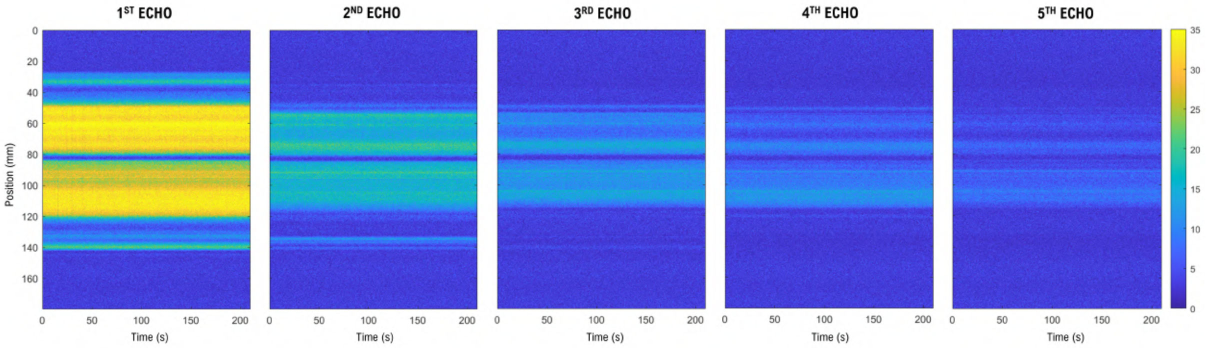

Figure 2.8: Line-scanning fMRI data - five multi-echo acquisitions for one run of a representative subject.

### 2.2.4 Physiological data acquisition

Simultaneously to the fMRI acquisition, the cardiac and respiratory fluctuations were monitored using the scanner's built-in PPG unit and respiratory belt, respectively. Both signals were acquired at a sampling rate of 500 Hz.

The respiratory belt was strapped around the subject's upper abdomen to measure changes in chest diameter, whereas the pulse-oximeter was placed on the right index finger to assess variations in global blood oxygenation by measuring the absorption of infrared light transmitted through the tissue [8], as illustrated in Figure 2.9. The waveforms acquired were used to determine the phase of the cardiac and breathing cycles at each time point of the fMRI data.

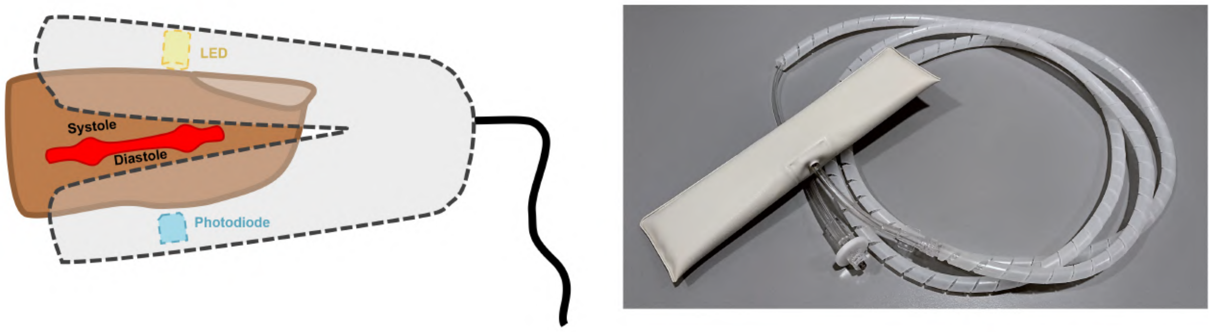

Figure 2.9: **(Left)** Schematic representation of a finger-based PPG sensor. Changes in light absorption are indicative of different phases of the cardiac cycle due to variations in blood volume and blood oxygenation. **(Right)** Respiration belt transducer.

## 2.3 Data processing

### 2.3.1 Physiological data analysis

The external physiological recordings were obtained during the fMRI experiment with the purpose of generating timecourse regressors from these signals, which could later be included in a GLM multiple regression analysis (further described in Section 2.3.5) to quantify their impact on the BOLD signal.

To guarantee the quality of the acquired physiological recordings, their timecourses were examined, as well as their frequency spectra, to ensure the presence of relevant time and frequency domain characteristics. A digital low-pass filter with a cutoff frequency of $f_c = 5$ Hz was first applied to both signals to discard any unequivocal noise contributions that would be responsible for non-physiological peaks. The cutoff frequency selected ensures that the first fundamental harmonics of the cardiac and respiratory cycles are preserved.

### 2.3.2 fMRI data analysis

The analysis of functional MRI data and the application of multiple denoising approaches comprised the bulk of this study. The data was processed using Matlab (version R2021a, Mathworks Inc.), the Statistical Parametric Mapping software package (SPM12, https://www.fil.ion.ucl.ac.uk/spm/) and some of the tools available in the FMRIB Software Library (FSL 6.0.4, https:/fsl.fmrib.ox.ac.uk/fsl).

Similarly to the analysis of physiological data, the time series and frequency content of the functional data were inspected to understand how the visual activation task and the acquisition parameters influenced the fMRI dataset. The five multi-echo acquisitions were analyzed separately.

Additionally, to isolate different brain tissues and study their responses to the visual activation task individually, tissue segmentation was performed using in-house software previously written in Python.

The averaged signals from GM, WM and CSF regions-of-interest (ROI) and their frequency distribution were interpreted in light of the structural characteristics of each tissue.

Following a preliminary analysis of the acquired line-scanning fMRI data, several denoising strategies were implemented and compared (as described in Sections 2.3.3 to 2.3.6). After the application of each of these methods, the resulting data was compared to the SoS-combined line-scanning fMRI data, which was used as a reference. Additionally, the evolution of relevant metrics were examined, such as the tSNR (evaluated through Equation 2.2).

$$tSNR = \frac{\overline{S}(t)}{\sigma(S(t))} \tag{2.2}$$

where $\overline{S}(t)$ is the mean signal over all time points and $\sigma(S(t))$ is the standard deviation of the signal across time [1].

### 2.3.3 Thermal noise removal

Improving the spatiotemporal resolution of fMRI measurements, such as in line-scanning fMRI, ultimately compromises the signal-to-noise and functional contrast-to-noise ratios, which remain relatively low in BOLD-fMRI despite many advances. In this study, the contribution of thermal noise is particularly significant due to the small voxel size of 0.25x2.5x4 mm$^3$ used.

Therefore, efforts to effectively improve the SNR, namely by removing thermal noise, are crucial for taking advantage of the full potential of line-scanning as well as other high resolution fMRI techniques.

***Weighted combination of Multi-Echo data***

The five multi-echo acquisitions were combined offline using in-house code previously implemented in Matlab. Based on the echo-combination modalities covered in Raimondo et al [47], the two strategies that revealed the highest BOLD sensitivity were selected for this study: a simple and computationally inexpensive SoS combination and a tSNR-weighted combination as proposed by Poser et al [40]. As its name implies, the tSNR-weighted combination uses the temporal SNR measured at each TE to compute the weighting coefficient for the corresponding echo signal. The equations used to merge the five signals into a single data matrix in both methods are presented in Table 2.1.

| **SoS** | **tSNR** |
|---|---|
| $\sqrt{\sum_{n=1}^{N=5} \lvert S_0 \rvert_n^{\,2}}$ | $\sum_{n=1}^{N=5} [\lvert S_0 \rvert_n . w(tSNR)_n]$<br>where $w(tSNR)_n = \frac{tSNR_n . TE_n}{\sum (tSNR_n) . TE_n}$ [40] |

Table 2.1: Equations used in the covered echo-combination weighting strategies.

The echo-combination method yielding the highest tSNR was used as a reference for subsequent analyses of the data acquired.

***NOise reduction with DIstribution Corrected (NORDIC) PCA denoising***

Additionally, a method based on the novel NOise Reduction with DIstribution Corrected (NORDIC) PCA method was implemented using Matlab and was included in the reconstruction pipeline before the coil and echo combination steps.

As described in Section 1.3.3, the original method involves hard thresholding of a singular value decomposition of the line-scanning fMRI data, in which all singular values below a selected threshold are set to zero. The proposed threshold-estimation process relies on geometry-factor maps, characteristic of parallel imaging studies. In this work, as an alternative to selecting a numerical threshold, increasing percentages of the lowest singular values obtained were set to zero (as illustrated in Figure 2.10) to remove components indistinguishable from zero-mean Gaussian-distributed noise, such as thermal noise.

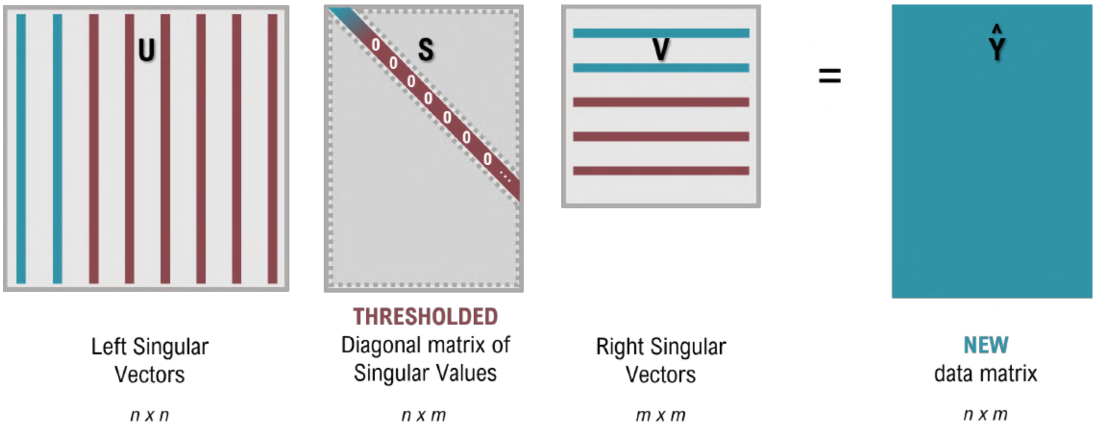

Figure 2.10: Schematic representation of a singular value decomposition submitted to hard thresholding. The singular values set to zero eliminate the contributions of the corresponding left and right singular vectors, resulting in a new data matrix, $\hat{Y}$.

Reconstruction with and without NORDIC-based denoising were compared in terms of tSNR, t-statistics and percent signal change within an ROI of interest for 4 different thresholds - 20, 50, 70 and 90% of the singular values obtained were set to zero. To validate the application of this denoising method to line-scanning fMRI data, the coherence between these results and the conclusions from the original NORDIC PCA publication [35] was assessed.

### 2.3.4 Differentiating BOLD and non-BOLD signals through TE-dependence

To characterize the evolution of different fMRI timecourses across echo-times, two well-defined ROIs were considered - one containing voxels within the superior sagittal sinus (typically significantly contaminated by cerebrovascular pulsatility, and thus with a high $S_0$ contribution), and the other including GM voxels with the highest relative activation for each subject (and consequently having a high $T_2^*$ contribution).

The signal from each ROI was classified as BOLD-like or not BOLD-like by analyzing the degree to which the fMRI timecourse at each TE fit a relevant regressor, to determine whether they were $S_0$- or $T_2^*$-weighted. The sagittal sinus ROI was compared to a subject-specific physiological regressor, while the grey matter ROI was fit to the predicted BOLD response. Goodness-of-fit was quantified via the adjusted-$R^2$ metric.

By selecting these specific well-characterized regions, the accuracy of this method at categorizing other line-scanning fMRI signals as BOLD or non-BOLD can be assessed. The evolution of the adjusted-$R^2$ value (or an alternative goodness-of-fit metric of relevance) throughout echo-times for these specific signals can be considered as the standard progression for both $T_2^*$-weighted and $S_0$-weighted signals.

### 2.3.5 GLM-based denoising

The General Linear Model (GLM) describes the recorded BOLD signal as a linear combination of explanatory variables, also known as regressors (see Equation 2.3).

$$y(t) = \beta X(t) + \varepsilon(t) \tag{2.3}$$

where $y(t)$ is the fMRI time series, $X(t)$ is the design matrix containing the explanatory variables of interest as well as confounds, $\beta$ is the vector of coefficients that quantify the relative contributions of each component and $\varepsilon(t)$ is a vector of random Gaussian-distributed noise.

Different regressors that could be deemed as confounds were defined in an attempt to accurately represent the MR signal fluctuations unrelated to neuronal activation. GLM fitting was carried out using Matlab and, after computing the $\beta$ coefficients for each of the regressors added to the design matrix, these components were removed from the original fMRI data. A regressor describing the visual task was generated using the SPM software package with Matlab, based on the block design task convolved with a canonical HRF (see Figure 2.11 (Top)). This regressor was included in every GLM analysis along with confound regressors.

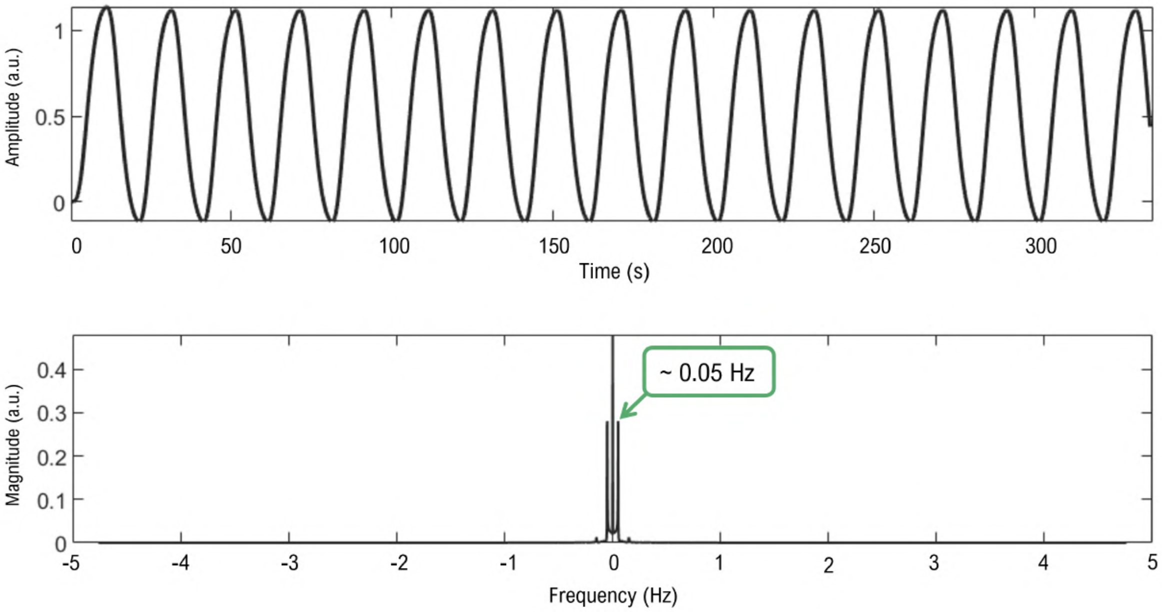

Figure 2.11: **(Top)** Task regressor representing the predicted BOLD response to a 10s ON/OFF flickering checkerboard visual task. **(Bottom)** Frequency spectrum of the visual task regressor. A strong peak at 0.05 Hz is descriptive of this task, since the task block is repeated every 20 s.

#### *Short TE1 signal as a nuisance regressor*

The very first echo in all multi-echo fMRI experiments in this study was acquired 6 ms after slice excitation. Due to the short echo-time, the contribution of BOLD-related fluctuations in the TE1 signal was considered to be negligible. Thus, this signal was used as a voxel-wise regressor for fMRI data acquired at a later TE to ensure higher BOLD sensitivity.

Because more than two echoes were collected, a weighted combination of the five echoes was first performed. GLM fitting was carried out considering the task regressor and a second regressor generated from the averaged timecourses of all voxels within the brain for the first echo acquisition (see Figure 2.12). Prior to being included in the design matrix, the TE1 regressor of each session was re-scaled using a standard min-max normalization.

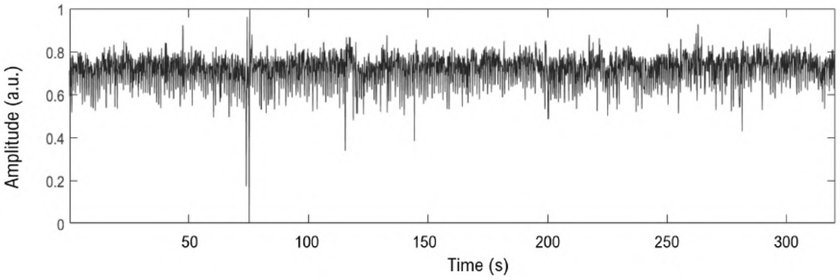

Figure 2.12: TE1 regressor of a representative subject defined as the average of the timecourses of all brain voxels.

After calculating the $\beta$ coefficients, the TE1 regressor was subtracted from the echo-combination signal, and the quality of the resulting data was assessed.

***White matter and CSF regressors***

Relying on the brain tissue segmentation described in Section 2.3.2, two regressors where generated from the average timecourses of white matter and CSF voxels, which went through a min-max normalization (see Figure 3.6). ROIs with a total of 90 and 30 voxels were considered for WM and CSF, respectively.

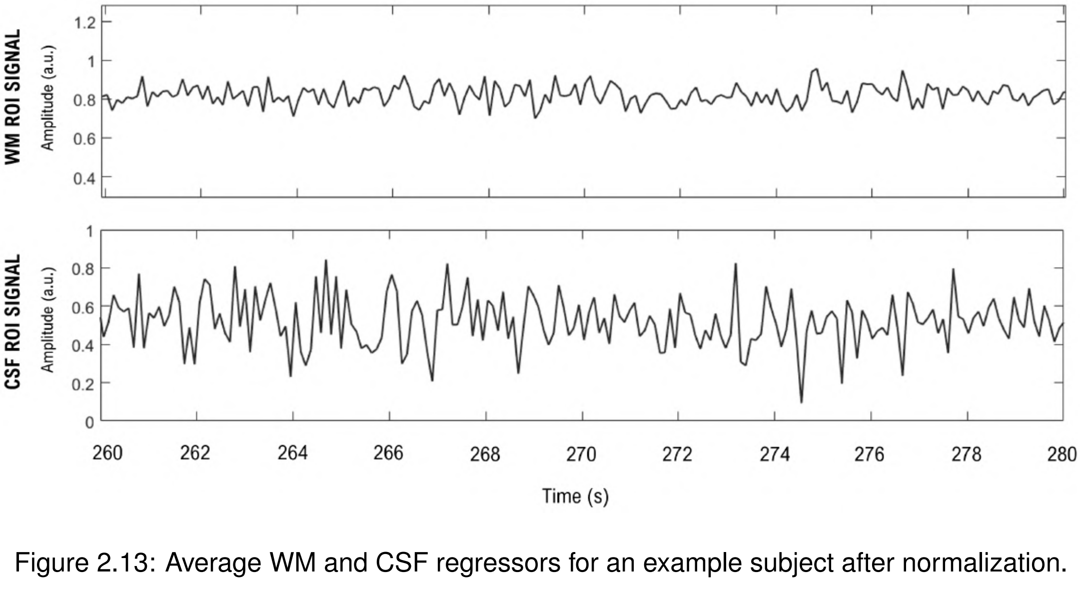

Figure 2.13: Average WM and CSF regressors for an example subject after normalization.

The characteristics of the tissue-specific signals were examined and compared to known confounding sources of the fMRI signal, such as the pulse oximetry recording from the PPG sensor.

The design matrix considered for the GLM analysis included both nuisance regressors described above and the task regressor. The $\beta$ coefficients computed were used to subtract the contributions of WM and CSF from the combined-echo data and the result was analysed.

### ***RETROICOR physiology regressors***

As opposed to the data-driven noise regression methods previously described, this section relied on a model-based denoising approach using the PhysIO Toolbox. This toolbox offers a model-based physiological noise correction alternative and is freely available as part of the open source TAPAS software (Translational Algorithms for Psychiatry-Advancing Science 2021, version 5.1.2, https://www.tnu.ethz.ch/en/software/tapas). Additionally, PhysIO features a full integration with SPM's Batch Editor Tool, offering a user-friendly and GUI-based experience for preprocessing and modeling the physiological data [48].

The peripheral physiological recordings were imported into the Batch Editor module, preprocessed and synchronized to its corresponding fMRI acquisition, considering the two different sampling rates. The automatized preprocessing steps included peak detection, band-pass filtering, cardiac and respiratory phase estimation, heart rate estimation and respiratory volume estimation [48].

RETROICOR is one of the noise modeling approaches integrated into the PhysIO toolbox, and the orders for the cardiac and respiratory Fourier expansions are fully customizable within the Batch Editor Tool (see Figure 2.14).

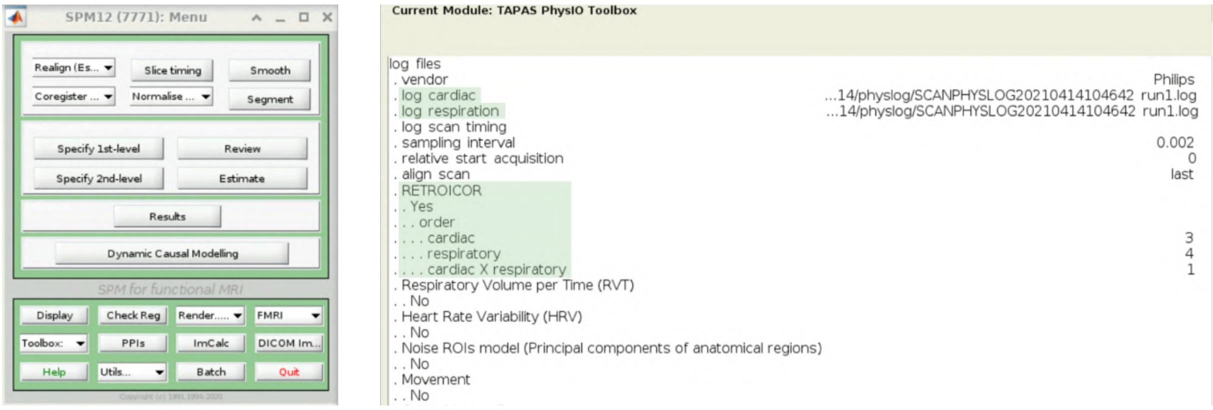

```
Current Module: TAPAS PhysIO Toolbox

log files
. vendor                                                              Philips
. log cardiac                  ...14/physlog/SCANPHYSLOG20210414104642 run1.log
. log respiration              ...14/physlog/SCANPHYSLOG20210414104642 run1.log
. log scan timing
. sampling interval                                                     0.002
. relative start acquisition                                                0
. align scan                                                             last
. RETROICOR
. . Yes
. . . order
. . . . cardiac                                                             3
. . . . respiratory                                                         4
. . . . cardiac X respiratory                                               1
. Respiratory Volume per Time (RVT)
. . No
. Heart Rate Variability (HRV)
. . No
. Noise ROIs model (Principal components of anatomical regions)
. . No
. Movement
. . No
```

Figure 2.14: **(Left)** SPM software main menu. **(Right)** Batch Editor Tool in which the physiological recordings are selected as well as the order of the Fourier expansions for the cardiac, respiration and cardiacXrespiration interaction models.

Different models were generated including cardiac and respiratory regressors of multiple orders, as well as multiplicative Fourier terms to account for interactions between the respiratory and cardiac cycles as proposed by Harvey et al. [49] (described by Equation 2.4). All RETROICOR models will be referred to using the notation "$x$C$y$R$z$X", i.e., $x^{th}$ order cardiac model, $y^{th}$ order respiratory model and $z^{th}$ order interaction model.

$$\begin{aligned} y_{cXr}(t) = \sum_{m=1}^{M} & [a_m \cdot cos(m\phi_c(t)) \cdot cos(m\phi_r(t))] \\ & +[b_m \cdot sin(m\phi_c(t)) \cdot cos(m\phi_r(t))] \\ & +[c_m \cdot cos(m\phi_c(t)) \cdot sin(m\phi_r(t))] \\ & +[d_m \cdot sin(m\phi_c(t)) \cdot sin(m\phi_r(t))] \end{aligned} \tag{2.4}$$

Similarly to other nuisance regression approaches, adding more physiological noise regressors to the design matrix does not necessarily lead to improvements in BOLD sensitivity or statistical significance due to the loss in degrees of freedom and possible noise overfitting [48]. Hence, 8 different models were generated in this study. The ”3C4R1X” model was considered the optimal RETROICOR model for physiological noise extraction [49], and any models with higher order regressors were not included. Figure 2.15 presents the design matrix of the ”3C4R1X” model.

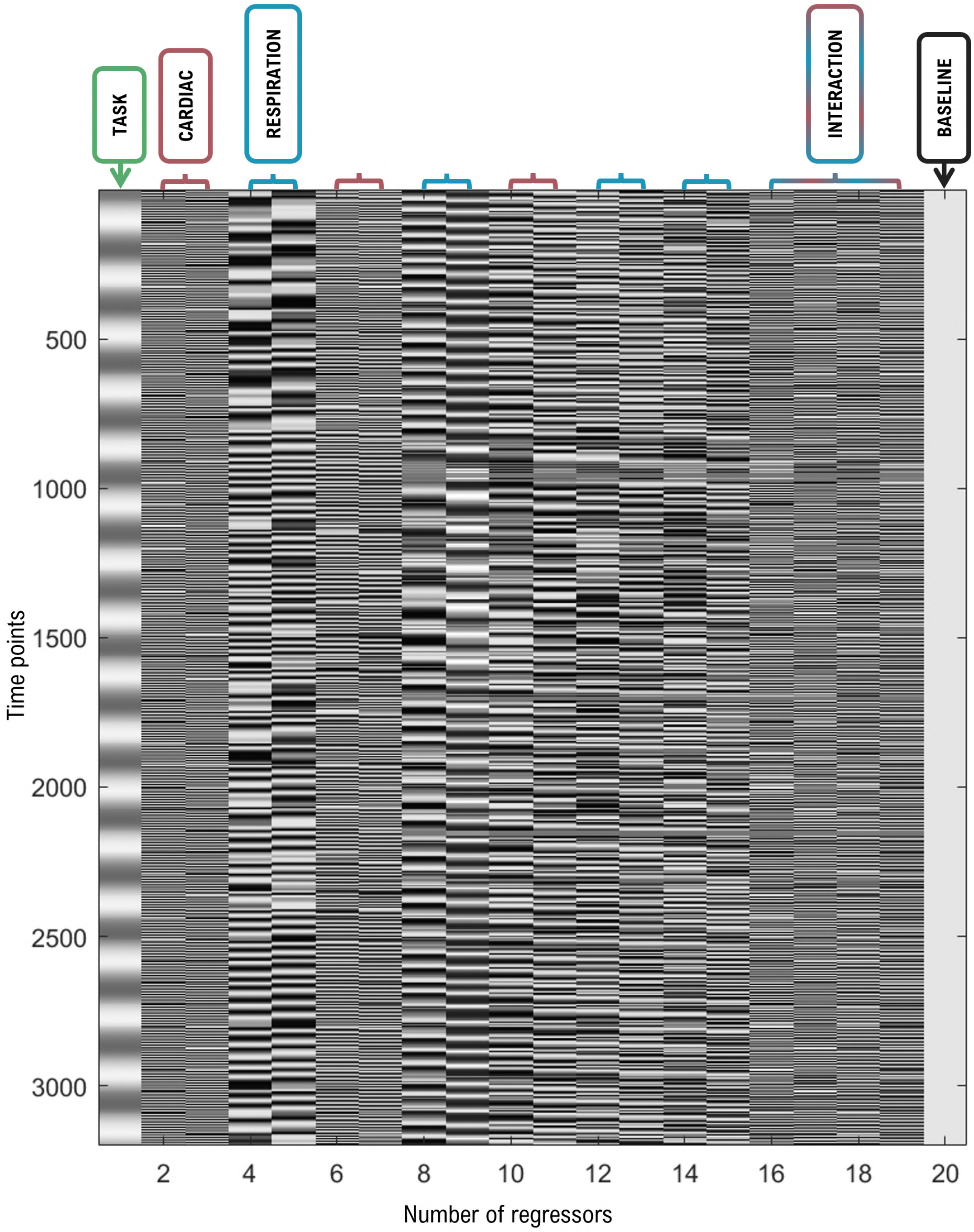

Figure 2.15: Design matrix used in the GLM analysis including the ”3C4R1X” physiological confound model (18 physiological regressors), the task-related regressor and baseline. A total of 20 regressors were considered.

Each added order to the cardiac or respiration Fourier models generates two sinusoidal components - a sine term and a cosine term, as described by Equation 1.2. The corresponding cardiac or respiration regressors result from the weighted sum of the two terms, using the respective GLM coefficients, as illustrated in Figure 2.16.

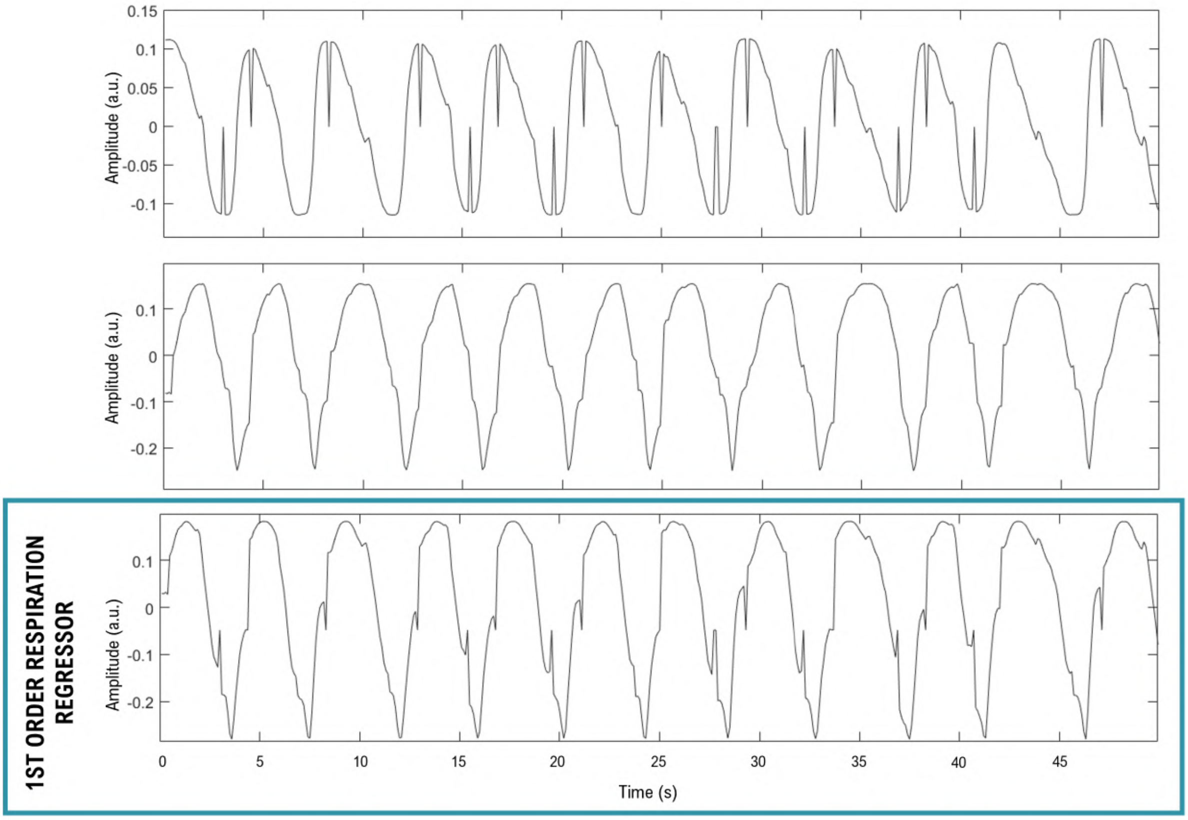

Figure 2.16: First order respiration regressor for a representative session. The resulting regressor is equivalent to a Fourier expansion with a sine term and a cosine term (shown in the two plots on top), weighted by their respective coefficients. The two sinusoidal terms were generated using the PhysIO toolbox.

The original fMRI time series was then fit to each of the generated models and the goodness-of-fit was determined by calculating the adjusted-R$^2$. A GLM analysis for the RETROICOR models assigned $\beta$ coefficients for each component of the design matrix, allowing for the physiological regressors to be subtracted from the data according to their respective contribution.

### 2.3.6 ICA-based denoising

Lastly, an independent component analysis was performed using FSL's MELODIC ICA tool. Due to compatibility issues with line-scanning fMRI data, the command-line MELODIC was used instead of the GUI. Unlike most FSL modules, the MELODIC GUI is not equivalent to the command-line function, since the GUI-based implementation will call different preprocessing steps such as motion correction, spatial smoothing and registration, whereas the command-line MELODIC only performs the ICA decomposition and provides more control over its parameters. In particular, the arguments specified when calling command-line MELODIC were the following:

**- d** , to specify the number of ICs to which the original data should be reduced to
**- - nobet** , to switch off the brain extraction tool
**- - update_mask** , to disable mask updating

The selection of an optimal number of independent components for an ICA decomposition of fMRI data is not straightforward. In fact, there as been no consensus on the most pertinent method for choosing the ideal number of ICs [50]. Due to the high dimensionality and high noise level of fMRI data, applying ICA on the full spatial or temporal dimension is likely to overfit the data and degrade the ICA estimation [51]. Therefore, the number of informative independent components is often assumed to be much less than the spatial or temporal dimension of the fMRI data. In this study, a total of 10 independent components was defined (based on the results from [50]).

A typical ICA model assumes that the fMRI data can be modeled as a linear combination of independent sources with an unknown linear mixing process [52]. The fMRI signal can be represented by a space-time data matrix $X$ (see Equation 2.5).

$$X_{m\mathrm{x}n} = A_{m\mathrm{x}m} \cdot S_{m\mathrm{x}n} \tag{2.5}$$

where $A$ is an unknown mixing matrix and $S$ is a matrix of statistically independent source signals. The goal of ICA is to estimate an unmixing matrix $W$ such that $\hat{S}$ is a good approximation to the true sources $S$ (see Equation 2.6).

$$\hat{S}_{m\mathrm{x}n} = W_{m\mathrm{x}m} \cdot X_{m\mathrm{x}n} \tag{2.6}$$

The mixing matrix $A$ and the spatial activation maps of the estimated sources $\hat{S}$ were generated as outputs of the MELODIC command.

Once the ICA was computed, the estimated components were distinguished between neuronal-related and artifact-related using a manual classification approach. In general, manual classification of independent components is time consuming and lacks in reproducibility, but the unique dimensions of line-scanning fMRI data render the existing classification methods unreliable. Thus, the timecourses and frequency spectra of the generated ICs were carefully inspected and compared to the features of the task model and physiological regressors. The order in which the ICs were generated was taken into account as well, since their respective eigenvalues are arranged in descending order, indicating the amount of explained variance within each IC. Additionally, the TE-dependence of the resulting ICs was analysed as described in Section 2.3.4.

The removal of ICA components within FSL is usually carried out using the *fsl_regfilt* command. However, also due to compatibility issues with line-scanning data, this method could not be applied. Instead, a GLM analysis including all 10 ICs as explanatory variables was carried out in Matlab. Any components classified as noise were multiplied to the $\beta$ coefficients computed during GLM fitting and subtracted from the original data matrix. The quality of the denoised line-scanning data was assessed as previously described.

# Chapter 3

# Results and discussion

The following chapter describes the main results obtained throughout this study. The quality of the acquired physiological recordings was first assessed, to ensure the subsequent generation of accurate physiological regressors. The line-scanning fMRI data was also inspected, and the features of the BOLD signal for the multiple echoes and different brain tissues were evaluated.

After becoming acquainted with the fMRI data, the outcome of applying several denoising techniques is presented. Firstly, the effects of thermal noise removal through: (1) weighted echo combination and (2) the implementation of NORDIC PCA described in Section 2.3.3 are shown and discussed. The removal of other noise sources, such as physiological fluctuations, is then also discussed by relying on the TE-dependence of fMRI signals and examining the results of an ICA decomposition and GLM analyses with different linear models.

## 3.1 Physiological data analysis

Figure 3.1 shows the pulse oximetry and respiration belt signals acquired during the scanning session of one participant.

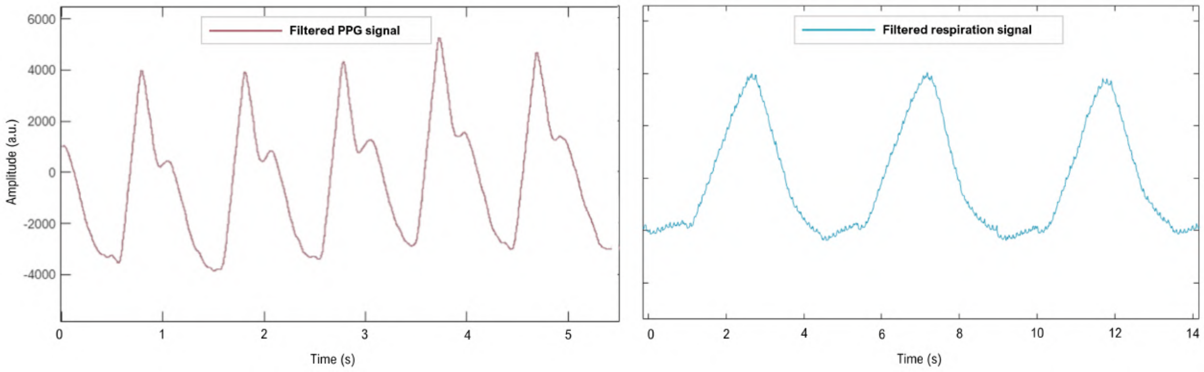

Figure 3.1: Representative examples of the **(left)** pulse oximetry and **(right)** respiratory amplitude signals acquired in this study.

Both physiological signals present the expected behaviour for all subjects - the pulse oximetry waves exhibit the characteristic R-peaks followed by T-waves and the respiratory amplitude signals present maximum and minimum peaks corresponding to the ends of inspiration and expiration, respectively. The filtered respiration signal in particular still shows considerable influence from noise.

The frequency spectra of the physiological recordings show distinctive peaks at 1 Hz and 0.3 Hz, related to the first harmonics of the cardiac and respiratory cycles, respectively (see Figure 3.2). Additionally, the frequency distribution of the cardiac signal shows two additional peaks at ∼2 Hz and ∼3 Hz, likely associated to higher order harmonic components of the signal. The PPG and respiratory belt recordings were inspected for all four subjects, and were deemed as accurate representations of these physiology cycles.

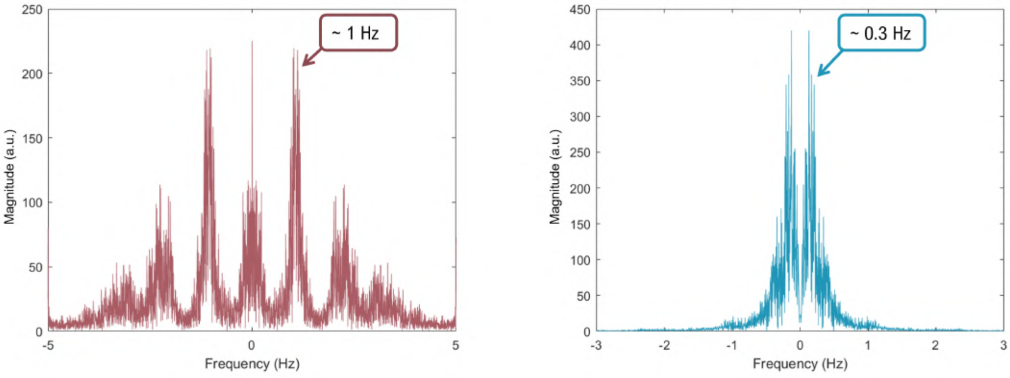

Figure 3.2: Filtered frequency spectra of the **(left)** cardiac and **(right)** respiratory trace for one representative subject.

## 3.2 fMRI data analysis

Following the physiological data analysis, the multi-echo fMRI acquisitions were inspected. Figure 3.3 shows the line-scanning data matrices for the five echo times and the frequency spectra for three of the acquisitions.

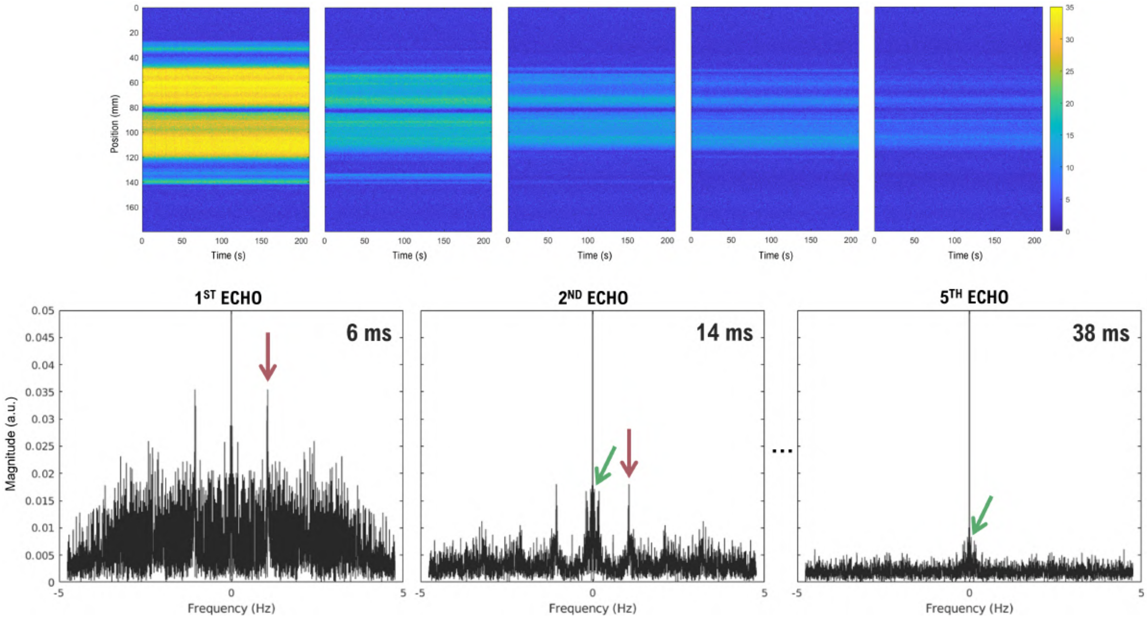

Figure 3.3: **(Top)** Line-scanning fMRI data for all five multi-echo acquisitions of a representative run. **(Bottom)** Frequency spectra for the first, second and fifth echo time signals averaged over all voxels in the line for a representative run. The red and green arrows point to the frequency peaks associated to the cardiac cycle ∼1Hz component and the ∼0.05Hz visual task BOLD response, respectively.

The reconstructed data matrices of the five multi-echo acquisitions are arranged in ascending order of echo-times. As expected, the earliest echo time has the highest signal intensity since the MR signal was only allowed to decay for a short amount of time (6ms). In contrast, the latter echoes show voxels in which the signal has decayed completely (signal dropout artifacts), which is due to the short $T_2^*$ values characteristic of brain regions with high magnetic susceptibility.

Additionally, the aforementioned figure shows the frequency spectra of the signals from three of the TE acquisitions. The first echo revealed the most significant contributions of cardiac-related fluctuations ($\sim$1 Hz) and thermal noise, evident by the uniform distribution of frequencies across the entire spectrum. As expected, at TE1 = 6ms the signal has no significant BOLD-weighting, validating the use of short-echo data for correcting motion and physiological noise. For the following echo times, the power density of physiological frequencies gradually decreases, while the power density of the frequency associated to the visual task response ($\sim$0.05 Hz) increases for the second echo signal and then drops steadily for the remaining acquisitions, while still maintaining relevance within the respective frequency spectra.

For further analysis of the line-scanning data, a tissue segmentation protocol was used to generate masks of different brain regions - grey matter, white matter and CSF. The segmentation results for one of the participants are shown in Figure 3.4.

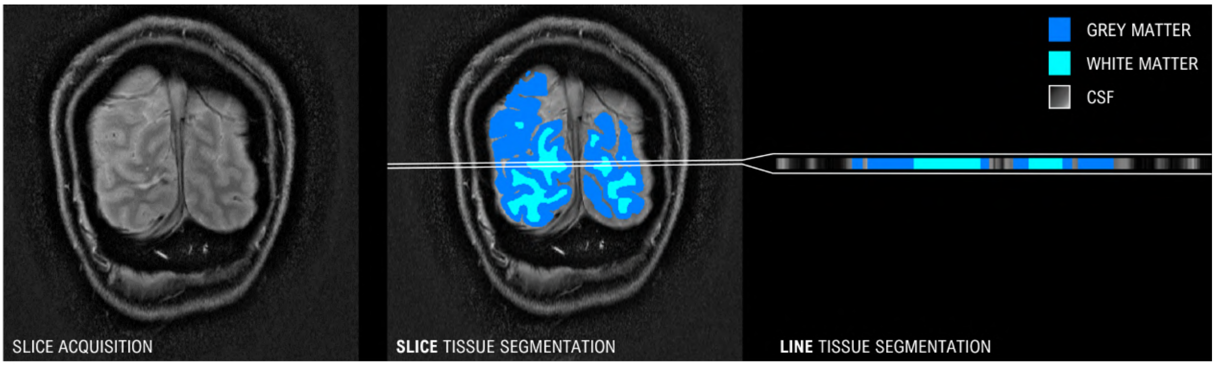

Figure 3.4: Tissue probability maps of grey matter, white matter and CSF for one representative subject. Segmentation was performed for the entire slice.

Relying on the segmentation results, the averaged signal of grey matter, white matter and CSF ROIs were analyzed separately.

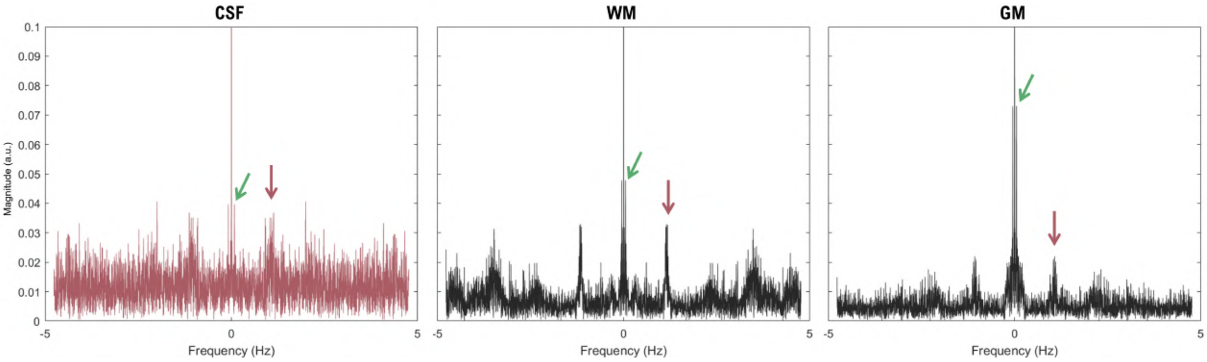

Figure 3.5: Frequency spectra of the averaged signal from **(left)** CSF, **(center)** white matter and **(right)** grey matter voxels. The red and green arrows point to the frequency peaks associated to the cardiac cycle $\sim$1 Hz component and the $\sim$0.05 Hz visual task BOLD response, respectively.

The CSF signal revealed a significant contribution from cardiac noise (associated to the 1 Hz frequency peak in Figure 3.5). However, the spectral density of the cardiac-related fluctuations was comparable to that of the task BOLD-response, despite the lack of neuronal activation in this tissue. Although a single voxel may contain several types of tissues, the finite spatial resolution of fMRI imposes misclassifications under the assumption that each voxel contains a single and pure tissue type. This phenomenon is referred to as partial volume effects (PVE) and occurs especially at tissue boundaries, causing errors in tissue segmentation and tissue property quantification [53]. Therefore, considering the frequency spectrum obtained for the averaged CSF signal, voxels with substantial $T_2^*$-weighting were likely incorrectly classified as CSF during tissue segmentation, resulting in a prominent peak at the visual task frequency. Moreover, the presence of thermal noise was the most pronounced in the CSF signal, compared to the other tissue types.

The averaged WM signal showed a relevant presence of both cardiac- and BOLD-related fluctuations, similarly to the CSF signal. Figure 3.6 compares the average WM and CSF time series to the external PPG recording of one participant.

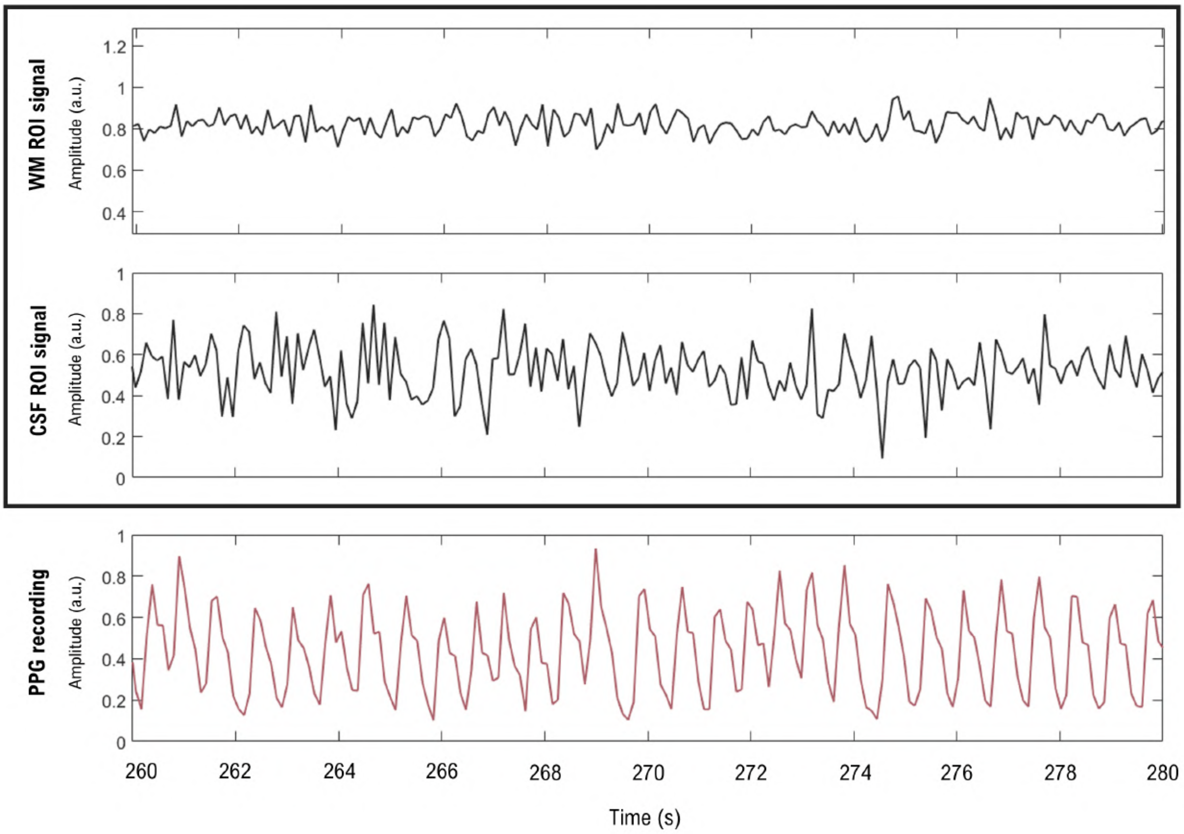

Figure 3.6: Average WM and CSF signals and PPG recording for a representative subject. The three signals were normalized.

Relatively to the WM time series, the CSF-related signal shows the most resemblances to the PPG recording, likely due to cerebrospinal fluid pulsation and proximity to major arteries and vessels [54]. The 1 Hz fluctuations are visibly present in both signals, however, other contributions other than simply cardiac are evident as well, as reported in the literature [55].

The frequency spectrum for the grey matter ROI in Figure 3.5 reveals that the signal is significantly contaminated by cardiac physiological noise, although less than the WM and CSF signals, as could be expected according to the literature [54]. This spectrum contains a very pronounced peak at the visual task frequency (0.05 Hz), which corresponds to the expected as well, due to the greater cerebral blood flow and volume of grey matter when compared to white matter, which has an impact on the BOLD signal

[56]. Additionally, the fMRI signal has been associated with post-synaptic potentials (mainly localized in grey matter), which further corroborates the prominent spectral peak at the visual task frequency.

Figure 3.7 overlays the visual task regressor onto the timecourse of the grey matter ROI. The raw signal time series for this ROI is represented in grey and, although it is relatively noisy, the moments in which the visual stimulus was presented to the subject are apparent due to the robust activation elicited in grey matter by the block design visual task implemented.

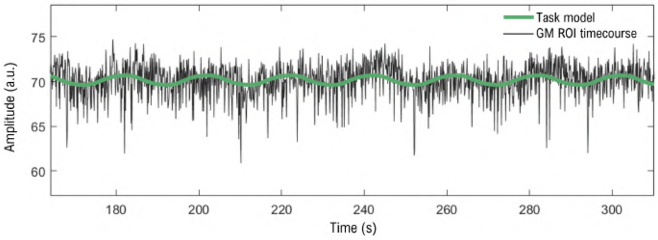

Figure 3.7: Visual task regressor fit for the average grey matter ROI signal.

In single-echo experiments, the fMRI signal is acquired at a predetermined TE optimized for BOLD contrast, which is typically close to the average $T_2^*$ value of grey matter in a targeted region [8]. However, different voxels have different $T_2^*$ decay rates depending on tissue properties and local magnetic field inhomogeneities. Relying on multi-echo fMRI, tissue properties can be parameterized through $T_2^*$ relaxometry, in which the $T_2^*$ constant of each voxel can be estimated from the data based on how the signal scales across echoes [39]. One such approach is fitting the signal across TEs to a monoexponential decay $S(TE) = S_0 \cdot e^{-TE/T_2^*}$. Figure 3.8 shows the $T_2^*$ relaxation curves for WM, GM and CSF voxels, as well as the decay curve for the averaged signal of the brain voxels of a representative participant. Moreover, a comparison between the average fMRI signal for all voxels within the brain across TEs and the monoexponential $T_2^*$ fit for those same voxels are compared as well.

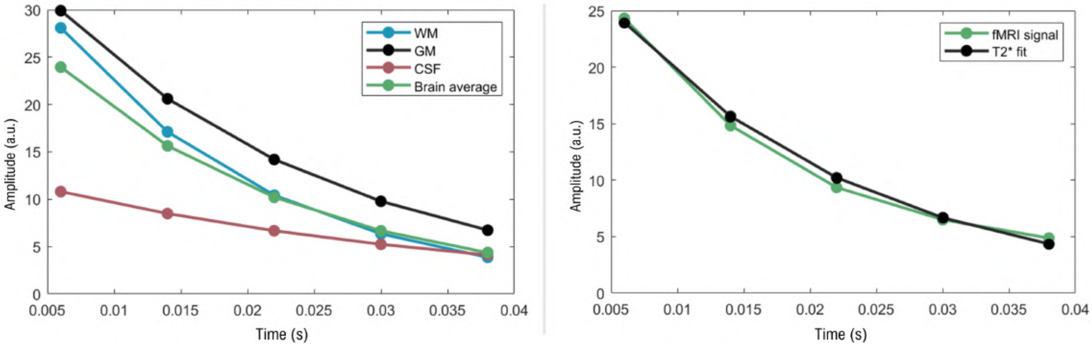

Figure 3.8: **(Left)** $T_2^*$ relaxation curves for WM, GM, CSF and all brain voxels. **(Right)** Comparison between the fMRI data across echo-times and the monoexponential $T_2^*$ fit for all brain voxels of a representative subject.

Fitting the data to a monoexponential decay model resulted in the estimation of the $T_2^*$ measurements presented in Table 3.1 for each tissue type. The values obtained were reasonably consistent with those previously described in the literature for fMRI at 7T [57][58][59], although some differences were expected due to distinct voxel sizes and ROI definition approaches. The estimated $T_2^*$ measurements are lower than expected, which can be attributed to ”partial voluming” and to the relatively thicker slice, since this leads to increased dephasing of spins within the slice and ultimately shortens the $T_2^*$.

Although the estimated values are overall lower than expected, the shorter $T_2^*$ for white matter, followed by the higher values for grey matter and, at last, CSF, are coherent with the literature.

| **Tissue** | **Estimated $T_2^*$ (ms)** | **Reference $T_2^*$ (ms)** |
|---|---|---|
| White matter | 19.2 ($\pm$ 1.6) | 26.8 ($\pm$ 1.3) |
| Grey matter | 22.7 ($\pm$ 2.0) | 33.2 ($\pm$ 1.2) |
| CSF | 37.5 ($\pm$ 7.4) | 168 ($\pm$ 12) |
| Brain average | 21.2 ($\pm$ 1.5) | - |

Table 3.1: Average $T_2^*$ measurements estimated in this study for all participants and reference $T_2^*$ measurements from Haast (2018) [58] and references therein.

It can be concluded that $T_2^*$ relaxometry can be used in line-scanning fMRI data to relate signals to their generative physical processes, providing important insight on the inner structure of tissues at a submillimeter scale [60]. By individually fitting the signal of each voxel to the monoexponential curve, tissue characteristics can be identified and artifactual contributions to the BOLD signal can be isolated and later removed.

## 3.3 Thermal noise removal

In this section, thermal noise removal was carried out using the implementation of NORDIC PCA described in Section 2.3.3 and two distinct combination strategies for multi-echo data. The respective results of each method were analyzed.

### 3.3.1 Weighted combination of Multi-Echo data

Multi-echo fMRI experiments are heavily used for validating BOLD-related signal origins, not only through relaxometry (as demonstrated in Section 3.2) but also through echo combination strategies to compensate for signal dropout effects. Although it may require a slight increase in TR to account for the acquisition of multiple echoes, ME-fMRI effectively improves sensitivity to BOLD signal, reduces the effects of thermal noise and does not imply an increase in specific absorption rate (SAR) as there are no additional excitation pulses [8]. The temporal SNR plots for each of the TE acquisitions are shown in Figure 3.9, along with the combined dataset resulting from a tSNR-weighted echo combination based on Poser et al [40].

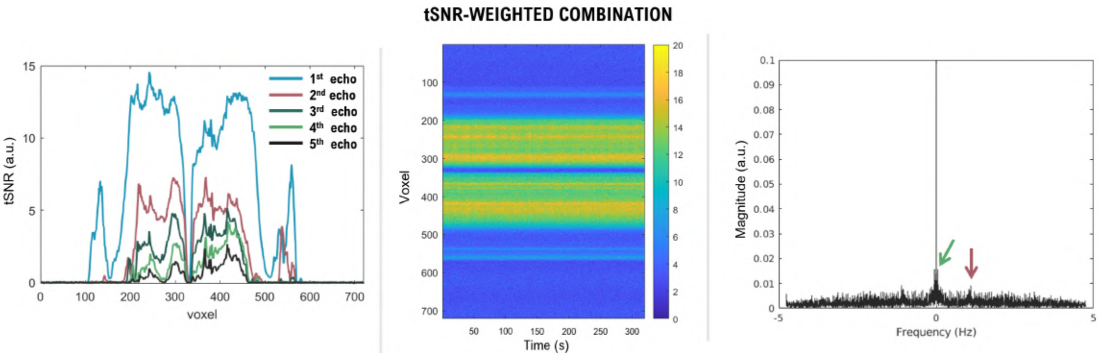

Figure 3.9: **(Left)** Temporal SNR plots for the five multi-echo fMRI acquisitions of a representative subject. **(Center)** Line-scanning data matrix after tSNR-weighted echo combination. **(Right)** Frequency spectrum of the tSNR-weighted echo combination signal over all voxels. The green and red arrows indicate relatively substantial peaks at the visual task and cardiac cycle frequencies, respectively.

The tSNR values for each echo were used to calculate their corresponding weighting coefficients and, as expected, gradually decrease along the five acquistions. Due to the contribution of the final echoes, the overall signal intensity of the combined data decreased in comparison to the first TE acquisition. However, the signal intensity of the combined data remained the highest for voxels in which relevant neuronal activation was consistently present throughout echoes.

Figure 3.10 shows the data matrix obtained after a sum-of-squares (SoS) echo-combination, as well as its respective frequency spectrum.

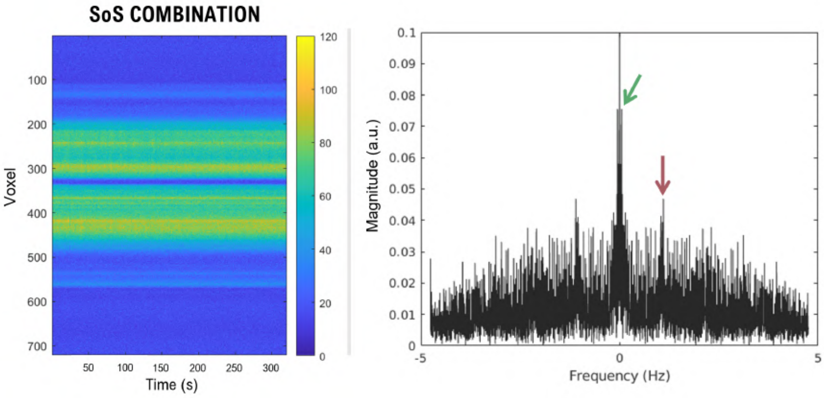

Figure 3.10: **(Left)** Line-scanning data matrix after SoS echo combination. **(Right)** Frequency spectrum of the SoS-combined line-scanning data over all voxels. The green and red arrows indicate substantial peaks at the visual task and cardiac cycle frequencies, respectively.

Overall, echo combination through SoS resulted in higher signal intensity for most participants. This was expected due to the more significant weighting coefficient attributed to the first echo in the SoS combination in comparison to the tSNR-weigthed coefficient, which is influenced by the 6ms TE1 (see equations in Table 2.1). A fast Fourier transform (FFT) was computed for the tSNR-weighted and the SoS-combined datasets, and the cardiac and task frequency peaks were evident in both spectra.

To determine which of the combination strategies should be used for the subsequent analyses of the line-scanning fMRI data, the tSNR and t-values were analyzed for each of the combined datasets, as shown in Figure 3.11.

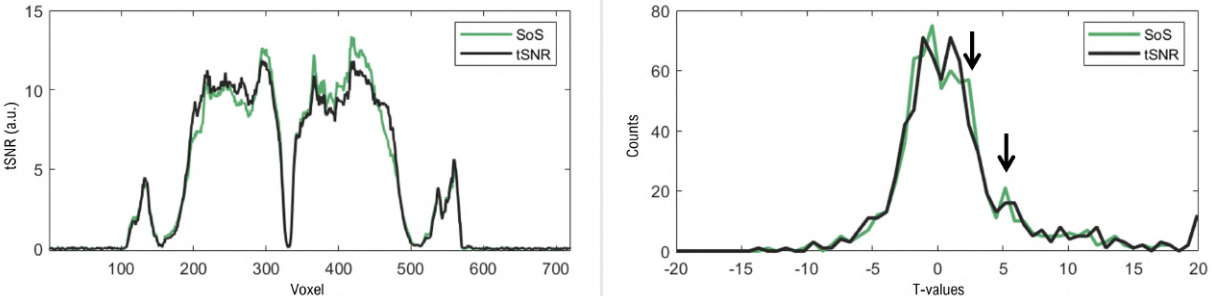

Figure 3.11: **(Left)** Temporal SNR plots and **(right)** t-values distribution for SoS and tSNR-weighted echo combinations for a representative subject. The arrows indicate an increase in the number of voxels with higher t-values for the SoS echo-combination method.

The SoS echo combination displayed slightly higher tSNR relatively to the tSNR-weighted combination in several of the voxels. Additionally, an increase in the number of voxels with higher t-values could be observed for the SoS-combined dataset, indicating a more statistically relevant correlation between the SoS-combined data and the predicted BOLD response.

Table 3.2 compares the mean tSNR and t-value for the two methods within an ROI showing significant activation (voxels with t-values above a selected threshold) for each of the four subjects.

| Subject | SoS combination | | tSNR-weighted combination | |
|---|---|---|---|---|
| | Mean tSNR | Mean t-value | Mean tSNR | Mean t-value |
| 1 | 9.79 | 18.04 | 8.94 | 18.32 |
| 2 | 11.70 | 1.49 | 10.87 | 1.60 |
| 3 | 11.78 | 9.90 | 10.70 | 9.82 |
| 4 | 11.24 | 0.47 | 11.47 | 0.35 |

Table 3.2: Mean tSNR and t-statistics values within an ROI showing relevant activation for the four participants.

For the majority of the subjects, the mean tSNR values were significantly greater for the SoS echo-combination, while the mean absolute t-values were only slightly weakened. Based on these results, the SoS echo-combination data was selected as the reference for all further denoising strategies applied.

### 3.3.2 NOise reduction with DIstribution Corrected (NORDIC) PCA denoising

After setting different percentages of the lowest singular values to zero, reconstruction of the line-scanning data involved coil and echo combination steps, which resulted in the data matrices shown in Figure 3.12. In this figure, the original data (on the left) can be compared to the denoised data after the removal of 50% and 90% of the SVD components. The signal outside of the brain (i.e., the top and bottom of the data matrices) was visibly reduced for both thresholds due to the removal of thermal noise.

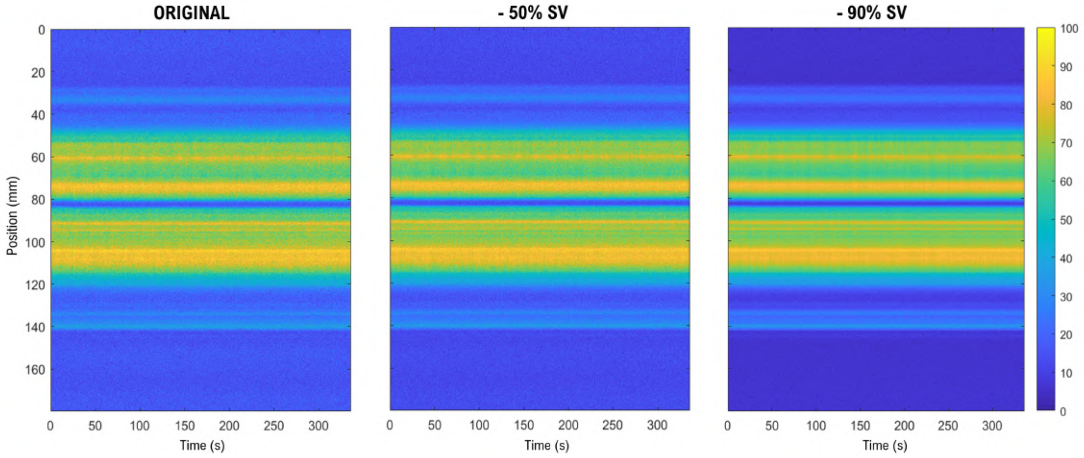

Figure 3.12: Line-scanning fMRI data matrices for a representative subject: **(Left)** Original data. **(Center)** Denoised data after the removal of 50% of the SVD components. **(Right)** Denoised data after the removal of 90% of the SVD components.

Additionally, for each acquisition, a 10-voxel ROI was defined in a region showing considerable neuronal activation. Figure 3.13 shows the tSNR and percent signal change (PSC) for the different thresholds for a representative subject. Similarly to the results in the literature [35], tSNR values increased significantly across all voxels after the removal of SVD components, particularly after setting 90% of the singular values to zero. Furthermore, the average of the percent signal change within the same ROI remained roughly constant after the application of NORDIC PCA, as also described in the literature.

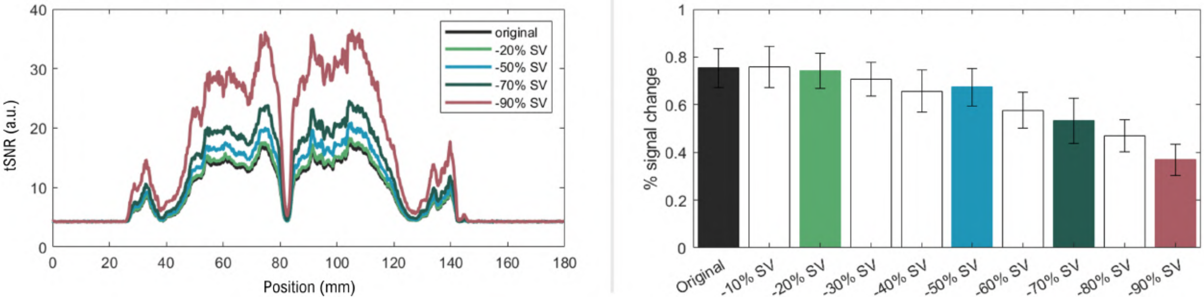

Figure 3.13: **(Left)** Temporal SNR comparison of the original line-scanning fMRI data and the NORDIC-denoised data for the different thresholds. **(Right)** Single-run percent signal change averaged across all voxels within the predetermined ROI for the different thresholds. The error bars represent the standard error across all voxels in the ROI.

The distribution of t-values across the line of interest for the different thresholds and for all four subjects was also analysed, as shown in Figure 3.14. Overall, more voxels with higher t-values were found for all participants as more components were removed, indicating a more statistically relevant correlation between the denoised data and the predicted BOLD response.

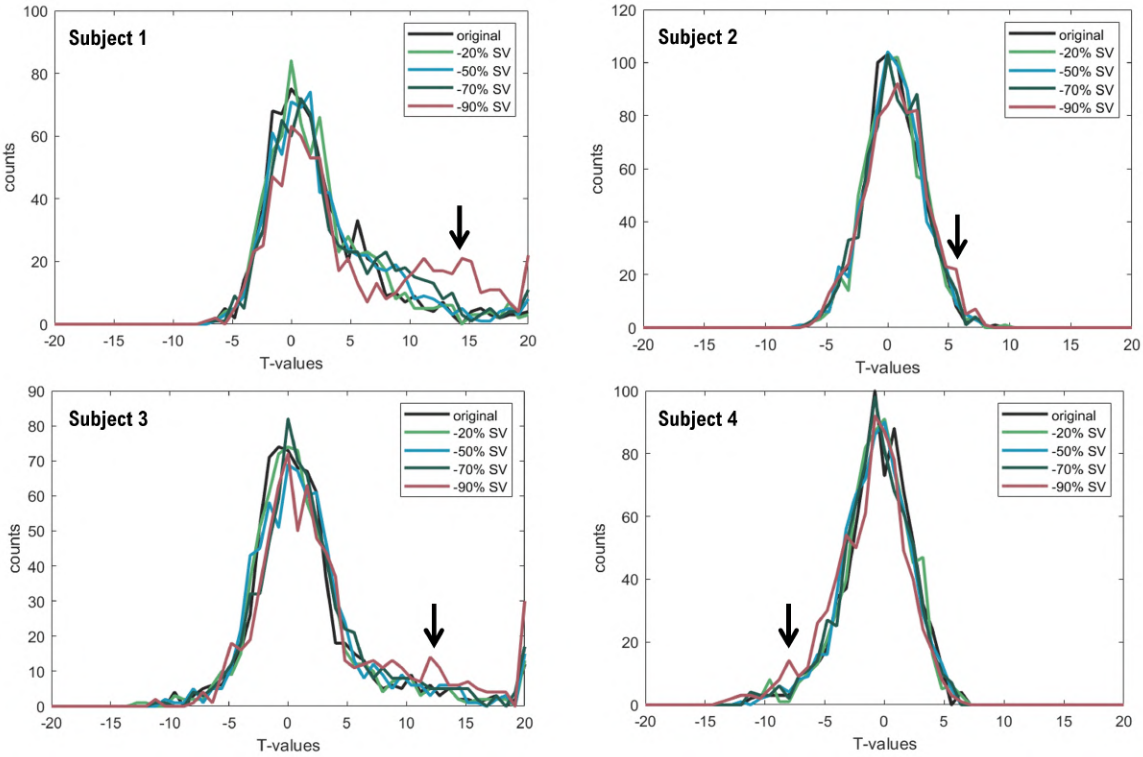

Figure 3.14: T-values distribution for all four participants. The arrows indicate an increase in the number of voxels with higher t-values for the denoised data.

The timecourses averaged over the ROI for the original data and for the denoised data after the removal of 50% and 90% of the singular values are plotted in Figure 3.15. The BOLD response to the visual task was maintained in all time series despite the removal of SVD components, as endorsed by the presence of 16 peaks within the timecourse, which correspond to the visual task blocks. Moreover, considering the decrease in variance as more components were removed, it can be concluded that a substantial amount of thermal noise was eliminated from the fMRI signal.

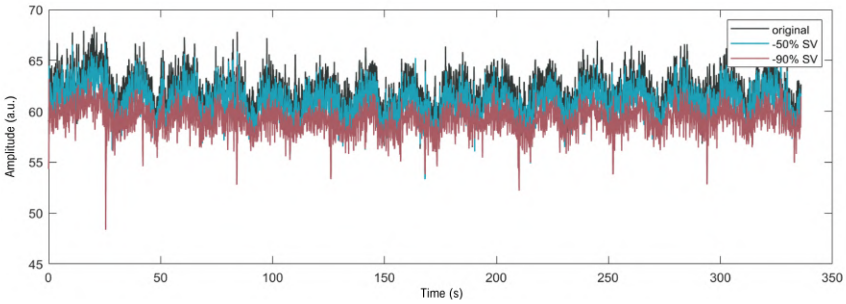

Figure 3.15: Time series of the line-scanning fMRI data in a predetermined 10-voxel ROI for a representative run. Three timecourses are shown - original data, denoised data after the removal of 50% of the singular values and denoised data after the removal of 90% of the singular values.

Although removing up to 90% of the SVD components may raise concerns about eliminating BOLD-related fluctuations, it is worth noting that the elements of the diagonal singular value matrices obtained in each decomposition were arranged in descending order, and the singular values removed were always selected from lowest to greatest. Because only a small number of singular values in each matrix were significantly greater than the others, a significant portion of the signal variance was still preserved when using the 90% threshold.

## 3.4 Differentiating BOLD and non-BOLD signals

In this section, two ROIs were selected for each single-subject analysis - one containing voxels within the superior sagittal sinus, and the other including grey matter voxels with the highest relative activation. Figure 3.16 illustrates the degree of correlation between: (left) the sagittal sinus ROI signal and a subject-specific physiological regressor ($S_0$-weigthed) and (right) the GM ROI signal and the predicted BOLD response ($T_2^*$-weighted). Goodness-of-fit was quantified across the five echo-times using the adjusted $R^2$ metric, particularly useful in this context as it penalizes the addition of unnecessary regressors to the model, thus avoiding overfitting the data.

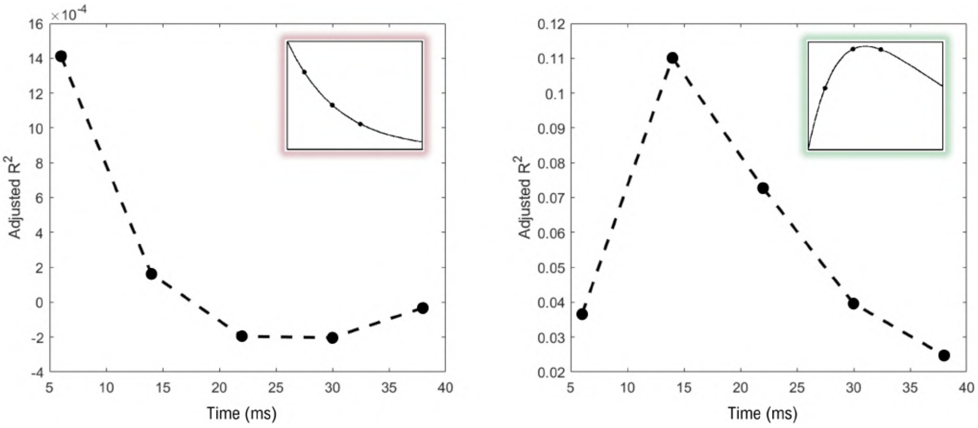

Figure 3.16: **(Left)** TE-independence of the sagittal sinus ROI signal changes. **(Right)** TE-dependence of the grey matter ROI signal changes. As described in Kundu et al [39], the predicted evolution of the goodness-of-fit for non-BOLD and BOLD-related fMRI signal changes is highlighted in red and green, respectively, for comparison purposes.

Across the five echoes, the fMRI signal within the sagittal sinus ROI followed the behaviour expected for non-BOLD fluctuations. The adjusted R$^2$ values quantifying the goodness-of-fit between the fMRI data and the physiological regressor declined steadily throughout the five echo acquisitions, indicating a worse fit across echoes due to the inevitable decay of the MR signal.

Contrastingly, the grey matter ROI signal showed an adjusted R$^2$ evolution comparable to BOLD-related fluctuations. For the first TE, the fMRI data revealed a low correlation to the predicted BOLD response, followed by a drastic increment in the second echo acquisition, which is consistent with the effects of neurovascular coupling mechanisms. The adjusted R$^2$ values for the remaining echoes gradually decreased also due to signal decay.

The evolution of the goodness-of-fit of line-scanning fMRI data to S$_0$- and T$_2^*$-weigthed regressors across echo-times was coherent with the results from Kundu et al [39], thus validating the use of this method for classifying signal sources of both BOLD and non-BOLD nature within line-scanning datasets. Therefore, this evaluation procedure can be applied to potential nuisance regressors prior to their removal, in order to verify their relevance, or lack thereof, to the fMRI experiment.

## 3.5 Regression of non-BOLD fluctuations

In this section, the effects of eliminating different non-BOLD signal contributions from the original echo-combined fMRI data were analyzed.

### 3.5.1 GLM-based denoising

***Short TE1 signal as a nuisance regressor***

The first echo acquisition of each session was averaged across voxels to obtain a time series that could be used as a nuisance regressor in a GLM analysis. The resulting regressor for a representative participant is plotted in Figure 3.17, along its frequency spectrum. It is worth noting that this regressor was generated by only considering the voxels within the brain, which explains the less significant presence of thermal noise in its frequency spectrum when compared to the complete first echo acquisition spectrum, shown in Figure 3.3.

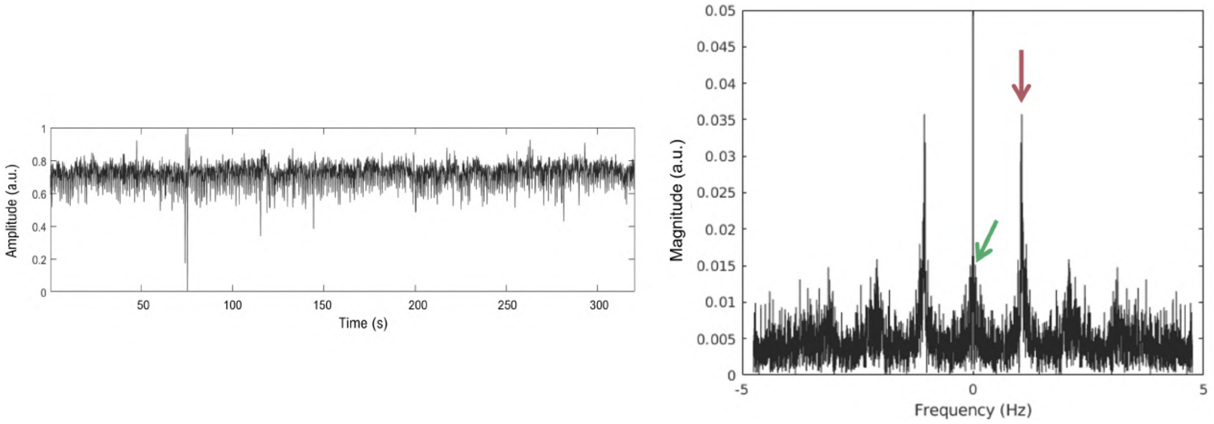

Figure 3.17: **(Left)** TE1 regressor - fMRI signal from the first TE acquisition averaged across all brain voxels. **(Right)** Frequency spectrum of the TE1 regressor. The green and red arrows indicate peaks at the visual task and cardiac cycle frequencies, respectively.

As it is not feasible to acquire data at TE = 0ms, it is possible that task-correlated blood volume effects are responsible for signal variance within the TE1 data [61]. The frequency spectrum presented above confirms the contribution of task-related BOLD signal in the acquired short echo-time signal, which can be attenuated (but not fully resolved) by further reducing TE1. Figure 3.18 presents a comparison between the original line-scanning data and the resulting matrix after regressing the short TE signal.

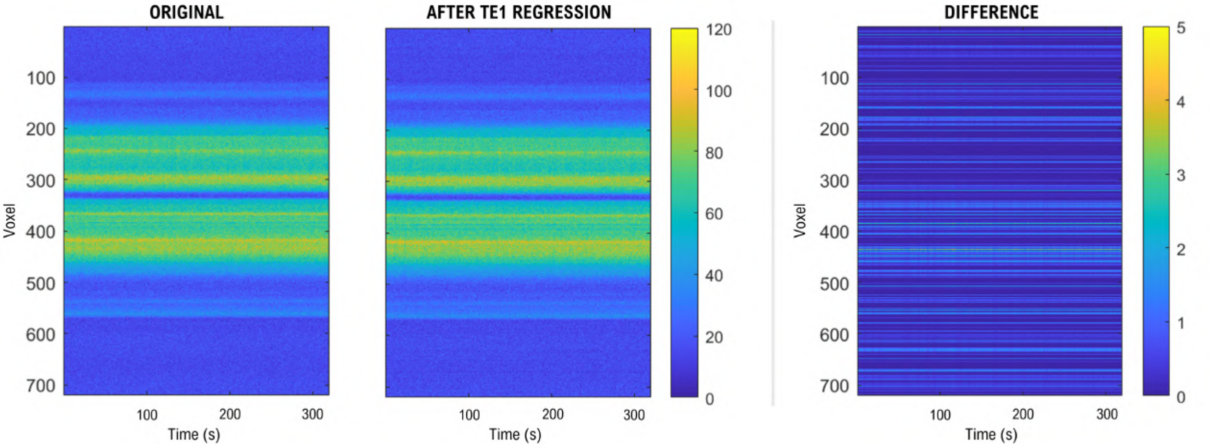

Figure 3.18: **(Left)** Original fMRI data matrix. **(Center)** fMRI data matrix after regressing out the average TE1 signal. **(Right)** Difference between the two previous matrices, depicting the effects of such regression.

The difference between the original and corrected line-scanning fMRI data reveals that the signal sources included in the TE1 regressor affected voxels across the entire line. However, in this particular subject, the largest differences were registered in voxels within the left hemisphere of the brain.

Figure 3.19 includes the original fMRI time series as well as the corrected timecourse resulting from TE1 regression. The amplitude of the signal was not affected, as could be concluded from the data matrices in Figure 3.18, while the signal variance decreased very slightly.

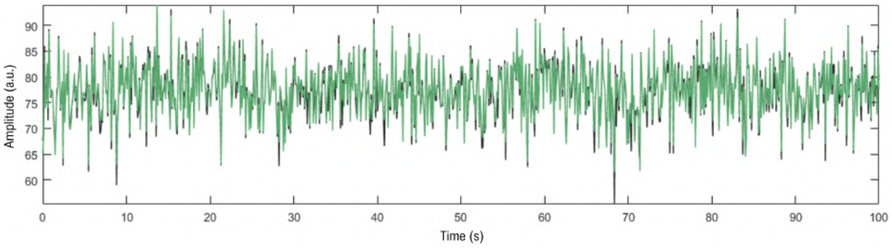

Figure 3.19: Comparison between the original and corrected fMRI time series, after TE1 regression.

Due to its characteristic acquisition time, regression of short TE data can potentially explain appreciable variance and increase significance of neuronal activations when there are large amounts of motion, thermal noise or physiology-related BOLD contamination [61]. To evaluate the effect of short TE regression, the temporal SNR and t-values distribution of the original and corrected datasets are compared in Figure 3.20.

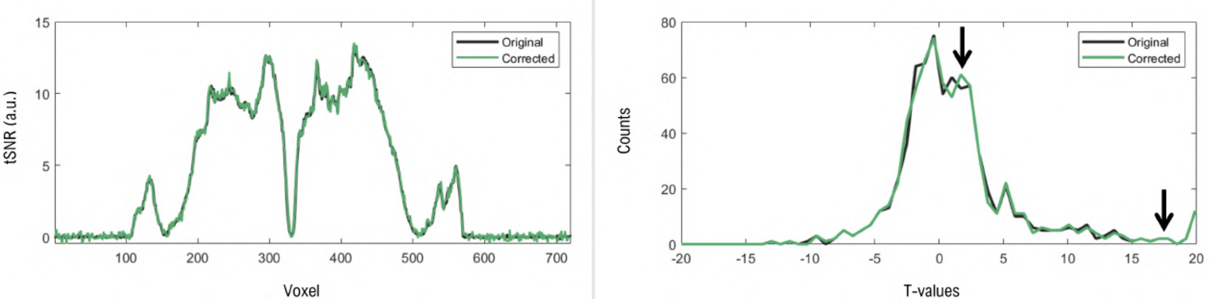

Figure 3.20: **(Left)** Temporal SNR plots and **(right)** t-values distribution for the original and corrected fMRI datasets. The arrows indicate an increase in the number of voxels with slightly higher t-values for the corrected data.

In general, short TE regression resulted in minor changes for both temporal SNR and t-values in comparison to the features of the original data, and ultimately did not improve task-related BOLD sensitivity.

### *White matter and CSF regressors*

As described in Section 1.3.3, the fMRI time series from WM and CSF voxels are often used as nuisance regressors. Despite the substantial visual task frequency peak in the WM spectrum shown in Figure 3.5, the relative contribution of physiological fluctuations, namely the prominent 1Hz peak associated to the first harmonic component of the cardiac cycle, could not be overlooked. Figure 3.21 compares the original data to the corrected data after removing variance contributions from WM and CSF voxels.

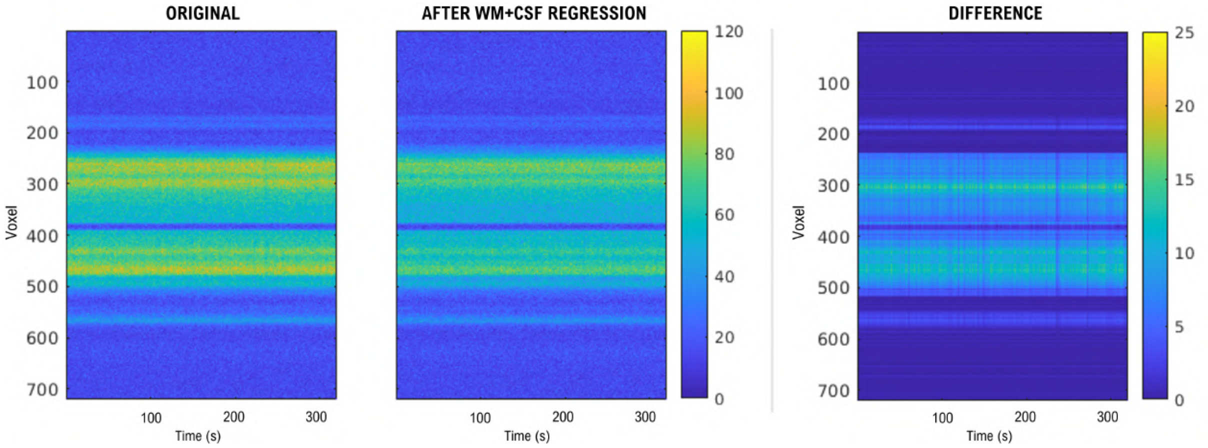

Figure 3.21: **(Left)** Original fMRI data matrix. **(Center)** fMRI data matrix after WM and CSF signal regression. **(Right)** Difference between the two previous matrices, depicting the effects of such regression.

In this case, the signal intensity decreased substantially in voxels within the brain. Although literature suggests that the fMRI signal from cerebrospinal fluid contains the greatest proportion of nuisance variance out of the three brain tissues studied, including motion, thermal noise and some physiological effects [62], voxels along the great longitudinal fissure (which separates the two brain hemispheres and coincides with the superior sagittal sinus) reveal a much less significant signal difference. The very small relative signal change in voxels within the sagittal sinus points to an unbalanced relationship between the $\beta$ coefficients attributed to the WM and CSF ROIs in the GLM analysis, thus indicating that the WM regressor is likely describing more signal sources other than physiological fluctuations.

In Figure 3.22, the time series of the original signal is compared to the result of WM and CSF regression.

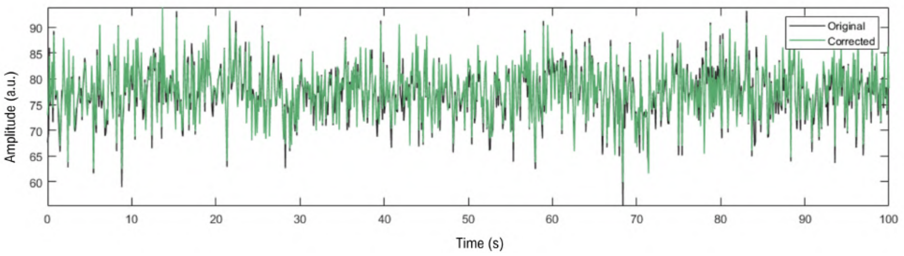

Figure 3.22: Comparison between the original and corrected fMRI time series, after WM and CSF signal regression.

Temporal SNR was reduced across the entire line and less voxels with higher t-values were obtained for the resulting data, as shown in Figure 3.23. These outcomes can suggest that the ROI defined may contain voxels with significant task-related BOLD signal (possibly even misclassified grey matter voxels).

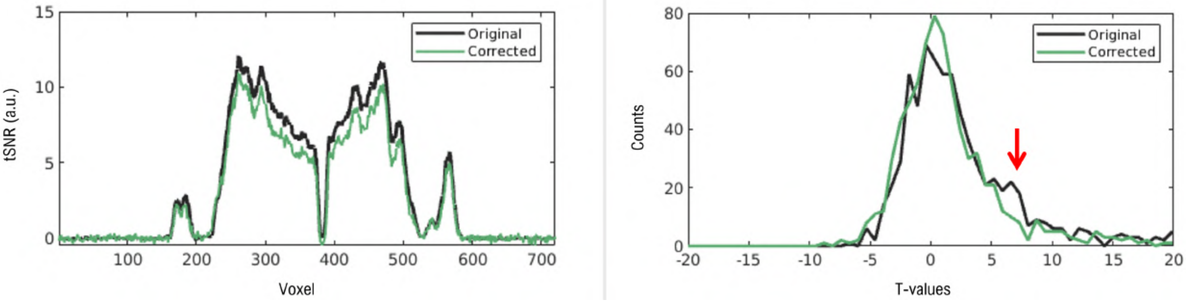

Figure 3.23: **(Left)** Temporal SNR plots and **(right)** t-values distribution for the original and corrected fMRI datasets. The red arrow indicates a higher number of voxels with higher t-values for the original data, which was not the desired effect.

In addition, and as previously mentioned in Section 1.3.3, some consider outdated to use WM fMRI activation as a nuisance regressor, as it contains relevant BOLD fluctuations [30]. To investigate further, the same regression process was repeated, but only considering the CSF signal as a nuisance regressor. Figure 3.24 shows the comparison between the original data and the corrected data.

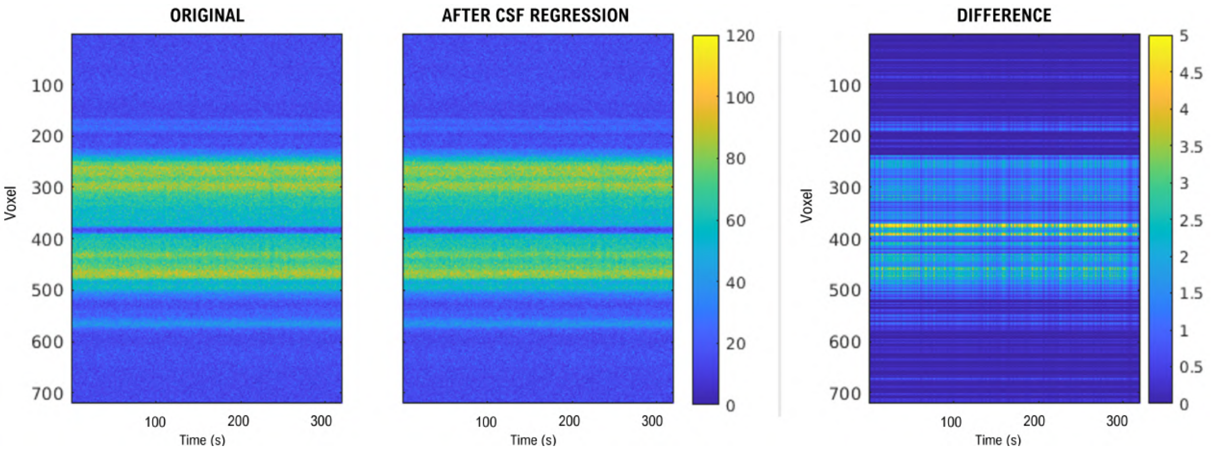

Figure 3.24: **(Left)** Original fMRI data matrix. **(Center)** fMRI data matrix after regressing out the average CSF signal. **(Right)** Difference between the two previous matrices, depicting the effects of such regression.

As expected, and as opposed to the regression of both WM and CSF signals, the signal difference is the greatest in the voxels between the two hemispheres. However, CSF regression removed signal from voxels across the entire line, including inside and outside the brain. These results may indicate the removal of both thermal noise and physiological fluctuations, which is corroborated by the literature as it considers the CSF signal to be a very complete tissue-based nuisance regressor [62].

Additionally, the time series of the original line-scanning data was compared to the data matrix resulting from CSF signal regression (see Figure 3.25). The removal of the CSF contribution resulted in a decrease of the signal variance, without affecting the signal amplitude, indicating that no BOLD components relevant to the experiment were removed.

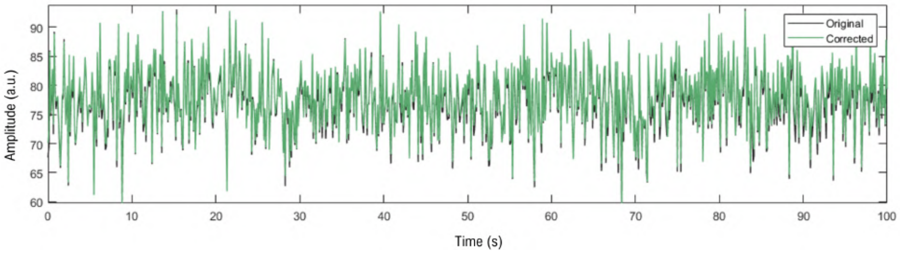

Figure 3.25: Comparison between the original and corrected fMRI time series, after CSF signal regression.

The temporal SNR and distribution of t-values for the data resulting from CSF regression are compared to the original data in Figure 3.26.

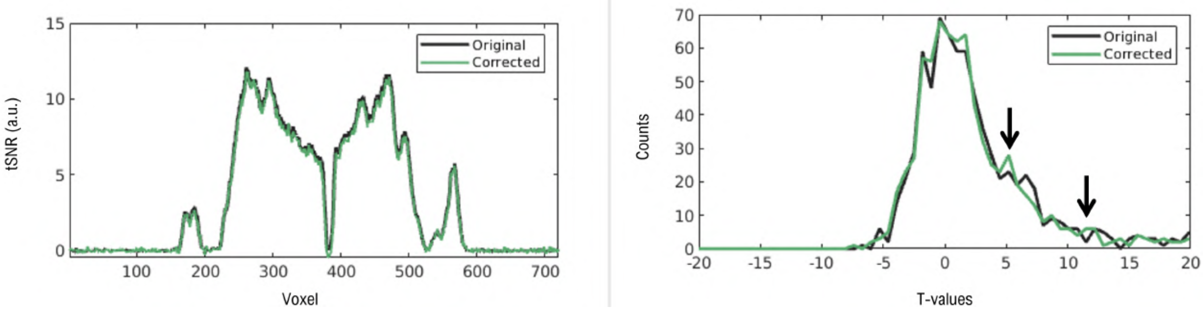

Figure 3.26: **(Left)** Temporal SNR plots and **(right)** t-values distribution for the original and corrected fMRI datasets. The arrows indicate the increase in the number of voxels with higher t-values for the corrected data.

Overall, the regression of CSF signal resulted in subtle changes for both temporal SNR and t-values distribution. Nevertheless, the statistical relevance of the denoised fMRI signal was not significantly improved nor degraded in comparison to the reference data, as occurred with the regression of both WM and CSF signals.

### ***RETROICOR physiology regressors***

Using the external physiological recordings acquired simultaneously to the line-scanning fMRI data, several multivariate linear regression models comprised of subject-specific physiology regressors were computed. Based on the RETROICOR noise modelling approach [17], cardiac and respiration regressors were generated, as well as multiplicative terms to account for the interaction between the cardiac and respiration cycles. The fMRI signal of a relevant voxel was fit to each RETROICOR model, and the correlation between the two was quantified by calculating the adjusted R$^2$, which only increases if each regressor added explains more of the signal variance than what would be expected by chance (i.e., if a random regressor were to be included in the model). Table 3.3 summarizes the adjusted R$^2$ values obtained for each model fit.

| **Order of Regressors** | | | **Adjusted-R$^2$** |
|---|---|---|---|
| Cardiac | Respiration | Interaction | |
| 0 | 0 | 0 | 0.5979 |
| 1 | 0 | 0 | 1.1380 |
| 0 | 1 | 0 | 0.7156 |
| 1 | 1 | 0 | 1.2600 |
| 1 | 1 | 1 | 1.3358 |
| 2 | 2 | 1 | 1.5113 |
| 3 | 3 | 1 | 1.7548 |
| 3 | 4 | 1 | 1.9165 |
| 4 | 4 | 1 | 1.9864 |
| 4 | 4 | 2 | 2.0291 |

Table 3.3: Adjusted R$^2$ values for each RETROICOR model generated for a representative subject.

To better interpret the results from Table 3.3, the adjusted R$^2$ values obtained for each model are plotted in Figure 3.27 as a function of the number of regressors included in the design matrix.

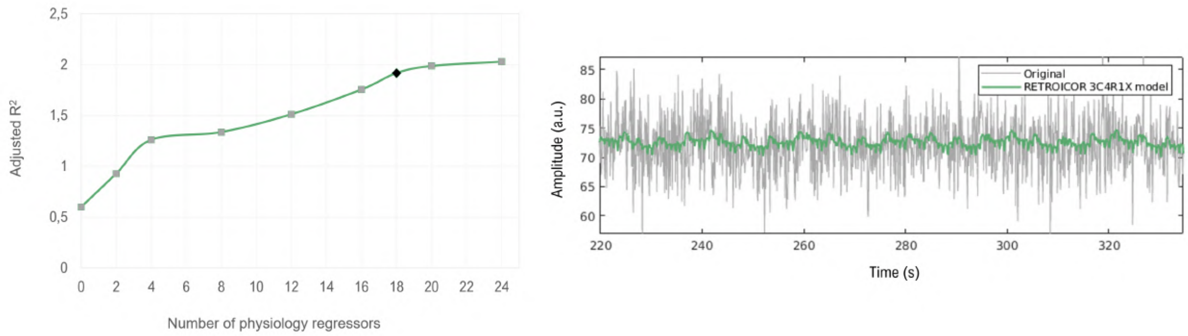

Figure 3.27: **(Left)** Adjusted R$^2$ evolution as a function of the number of physiology regressors included in the RETROICOR model. The point represented in black corresponds to the 3C4R1X model, with a total of 18 physiological regressors. **(Right)** RETROICOR 3C4R1X model fit to the time series of a relevant voxel.

Although the adjusted R$^2$ value increases for larger sets of explanatory variables (indicating an improvement of the model fit), resolving additional variance by adding more physiological regressors comes at the cost of losing degrees of freedom, and thus degrading the statistical significance of the results. The adjusted R$^2$ curve in Figure 3.27 eventually reached a plateau, suggesting the increases in adjusted R$^2$ were not worth the subsequent loss of degrees of freedom. The optimal model considered for this study was the winning RETROICOR model determined by Harvey et al [49], which included a third order cardiac model (6 sine/cosine terms), a fourth order respiratory model (8 sine/cosine terms) and a first order interaction model (4 sine/cosine terms) - "3C4R1X". The fMRI time series of a relevant voxel was fit to the optimal model as shown in Figure 3.27.

After GLM fitting, the physiological contributions to the fMRI signal, weighted by their $\beta$ coefficients, were removed from the data. Figure 3.28 compares the original matrix to the data after the regression of physiological noise

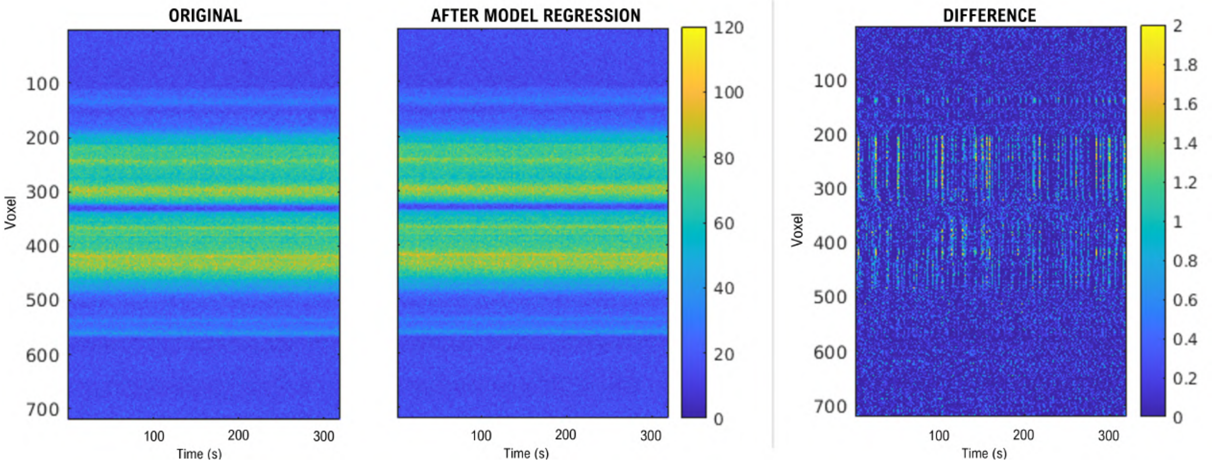

Figure 3.28: **(Left)** Original fMRI data matrix. **(Center)** fMRI data matrix after removing any signal correlated to the physiological regressors generated in RETROICOR. **(Right)** Difference between the two previous matrices, depicting the effects of such regression.

Interestingly, the BOLD signal changes are concentrated within the brain voxels and can be described as vertical stripes that extend through several neighbouring voxels. The disposition of the signal changes resembles a 2-dimensional sinusoidal wave, indicating an association to periodic physiological fluctuations.

In Figure 3.29, the time series of the reference line-scanning data is compared to the signal resulting from the described regression of physiological components. Similarly to TE1 and CSF regression, the signal amplitude was unaffected by the removal of physiological contributions, whereas the signal variance decreased slightly.

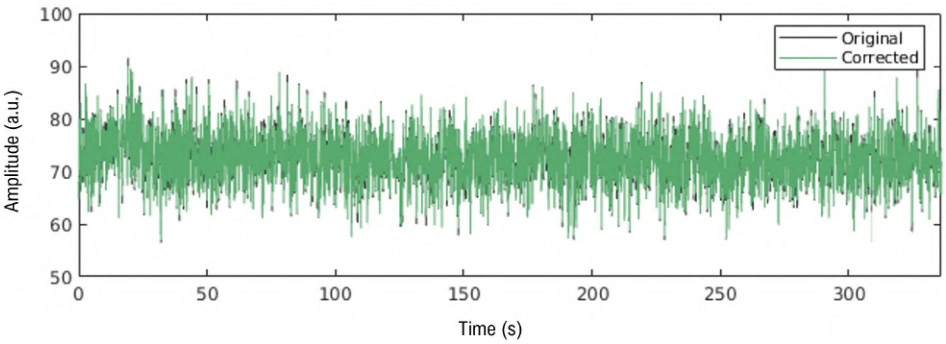

Figure 3.29: Comparison between the original and corrected fMRI time series, after removing the signal contributions correlated to the physiological regressors generated in RETROICOR.

Moreover, the temporal SNR and t-values distribution for the two datasets (original and corrected) are compared in Figure 3.30.

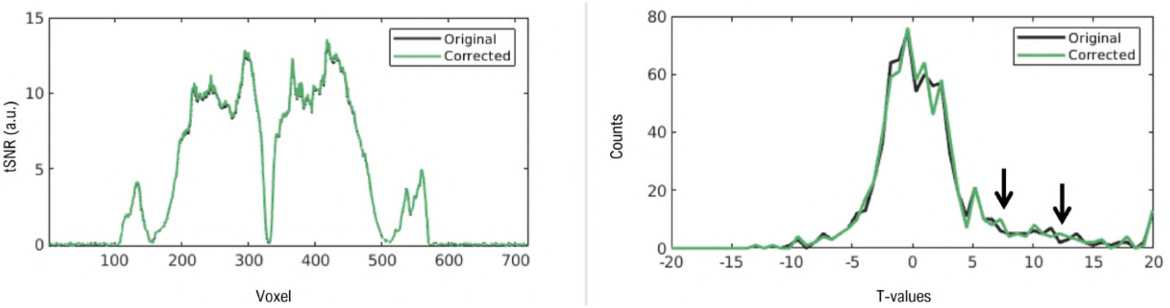

Figure 3.30: **(Left)** Temporal SNR plots and **(right)** t-values distribution for the original and corrected fMRI datasets. The arrows indicate an increase in the number of voxels with higher t-values for the corrected data.

In general, the regression of RETROICOR-based physiological regressors did not elicit major changes in terms of tSNR or t-values. However, both metrics suffered a marginal increase for some of the most activated voxels within the brain.

### 3.5.2 ICA-based denoising

The ten ICA components generated in FSL MELODIC for a representative dataset are shown in this section and were used as explanatory variables in a GLM analysis. Figure 3.31 presents the statistically independent spatial maps, which indicate the voxels activated by the independent signal sources identified within the original data. Additionally, a slice image acquired for the same participant was included in the figure below to associate activated voxels within the spatial maps to specific regions or tissues in the 2D image.

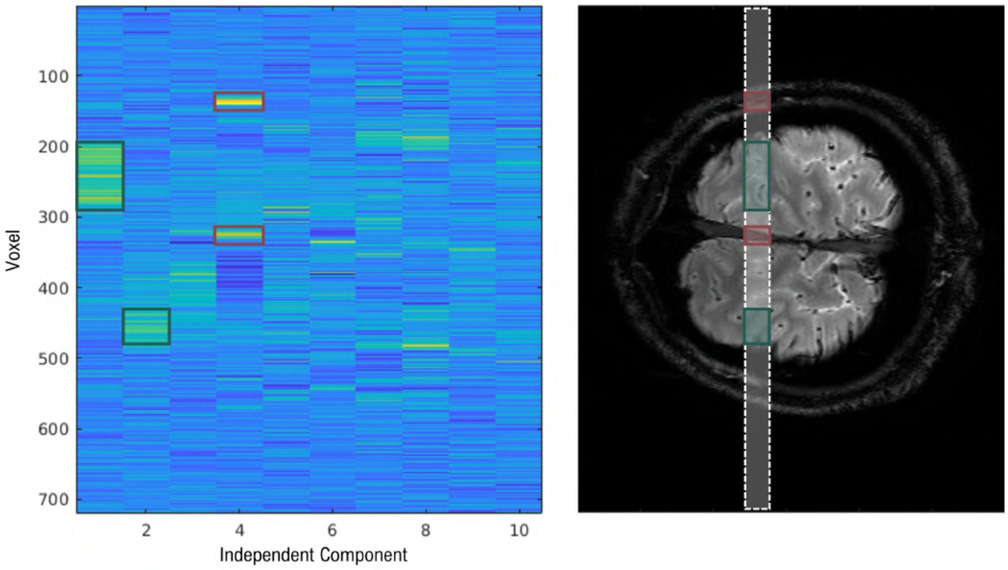

Figure 3.31: **(Left)** Spatial maps of the ten independent components generated by FSL MELODIC. **(Right)** Slice image indicating the most relevant regions activated by the independent signal sources. The red rectangles are associated to regions of non-BOLD fluctuations, whereas the green rectangles indicate grey matter voxels with strong neuronal activation.

The independent components generated through MELODIC are arranged in descending order of amounts of explained variance. The spatial maps of two of the most descriptive components are shown in Figures 3.32 and 3.33, overlayed on top of the slice image. Moreover, their respective time series and frequency spectrum are included as well, to assist manual classification.

The first independent component revealed statistically significant activation in voxels located in the right hemisphere of the brain. Its time series coincides with the behaviour of the blocked design visual task, and the frequency spectrum includes considerable peaks at the predicted BOLD response frequency (∼0.05 Hz). Thus, this component was classified as BOLD-related with reasonable certainty.

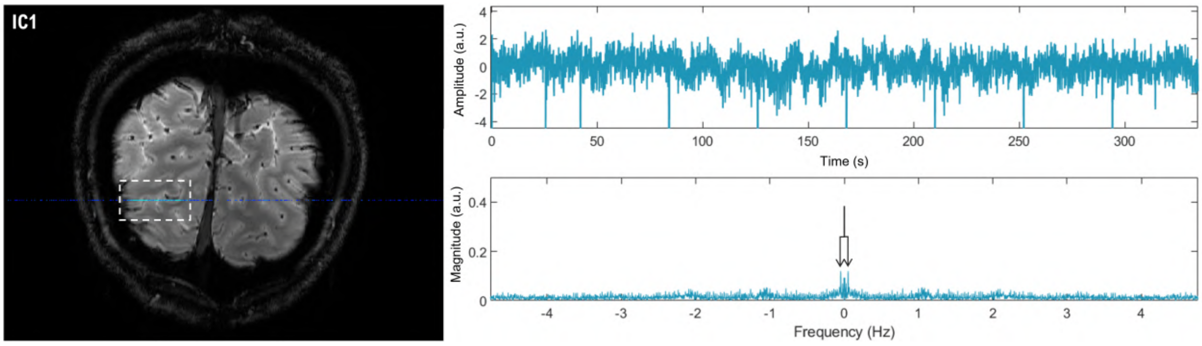

Figure 3.32: **(Left)** IC1 activation map over the slice image. **(Right)** Corresponding IC1 time series and frequency spectrum.

For the fourth independent component, the activated voxels were located within the subarachnoid space (a CSF-filled compartment which houses several major cerebral blood vessels) and the superior sagittal sinus (the largest of the sagittal sinuses). Additionally, its time series presents discernible ∼1 Hz fluctuations, as corroborated by the corresponding frequency spectrum. The classification of this component relies not only on the features of the time series and frequency spectrum, but also on the characteristics of the anatomical structures in which there was significant activation. This component was classified as artifact-related (non-BOLD) - in particular, it is associated with cardiac pulsatility effects within CSF and large blood vessels.

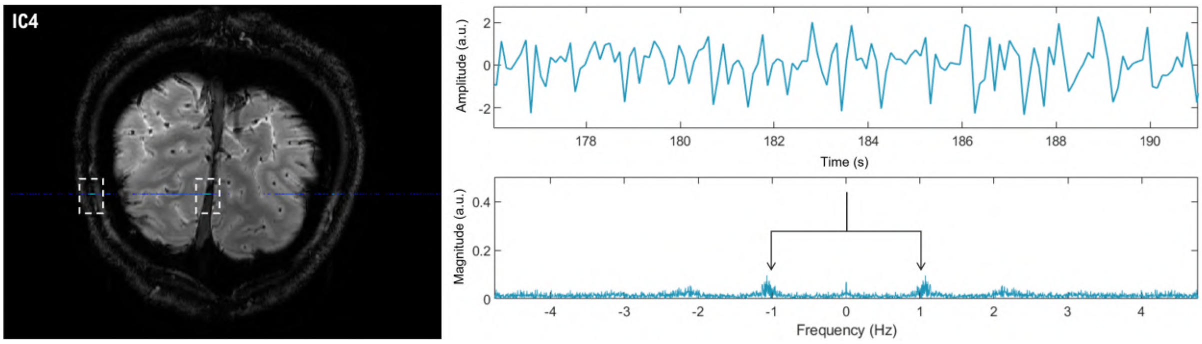

Figure 3.33: **(Left)** IC4 activation map over the slice image. **(Right)** Corresponding IC4 time series and frequency spectrum.

To analyze the TE-dependence of the contributions from these two independent components to the fMRI signal, the original data was fit to each IC time series for the five echo times, as shown in Figure 3.34.

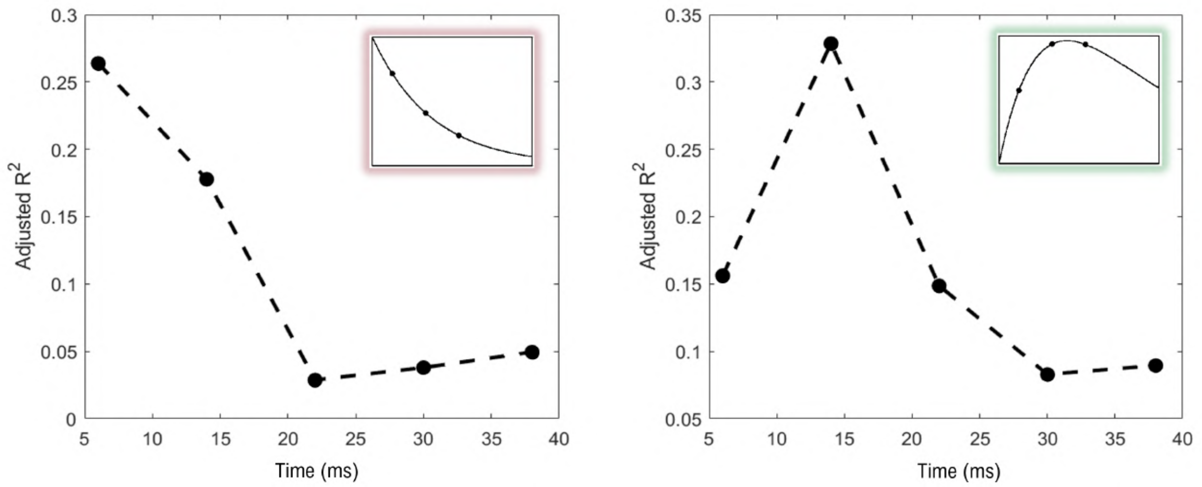

Figure 3.34: **(Left)** TE-independence of IC4-related signal changes. **(Right)** TE-dependence of IC1-related signal changes. The predicted evolution of the goodness-of-fit for non-BOLD and BOLD-related fMRI signal changes, as seen in Kundu et al [39], is highlighted in red and green, respectively, for comparison purposes.

As the IC4 time series is heavily $S_0$-weighted, its correlation to the fMRI signal decreases throughout echo times, as the magnetization decays. In the case of IC1, its time series is undoubtedly BOLD-related, which makes it a heavily $T_2^*$-weigthed signal. Thus, the IC1 fit to the fMRI data across echoes follows the adjusted $R^2$ evolution characteristic of BOLD-related fluctuations, with the highest correlation between the two signals at the second echo-time.

A GLM analysis included all independent components as explanatory variables. All non-BOLD components (such as the time series associated to IC4), were subsequently removed from the original data, weighted by their respective $\beta$ coefficients. In Figure 3.35, the original data is compared to the result of removing ICA components.

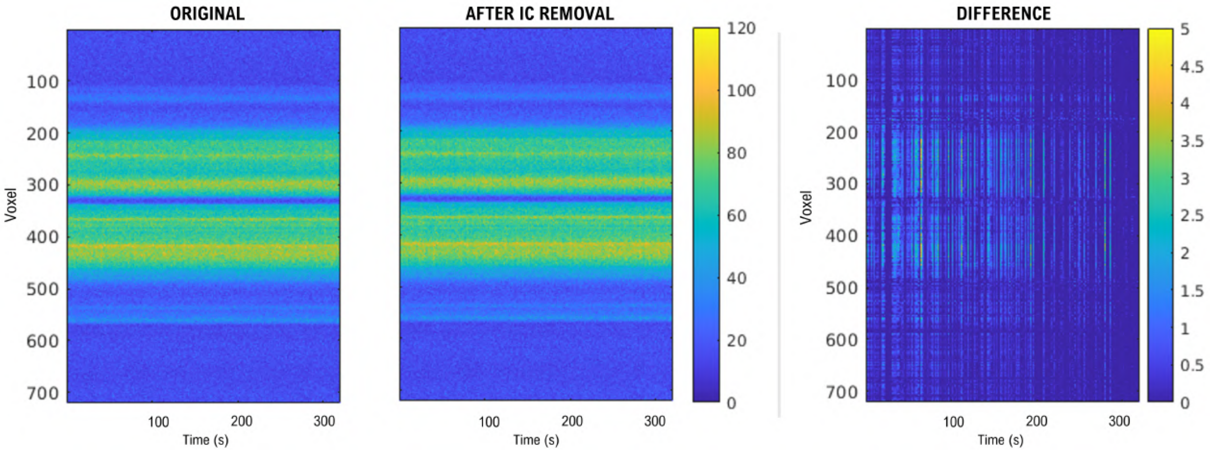

Figure 3.35: **(Left)** Original fMRI data matrix. **(Center)** fMRI data matrix after regressing out non-BOLD related independent components. **(Right)** Difference between the two previous matrices, depicting the effects of such regression.

The BOLD signal changes are evident across the entire line and, once again, can be described as vertical stripes throughout the data matrix, indicating a significant removal of periodic physiological noise, particularly, cardiac fluctuations.

Figure 3.36 compares the original to the corrected time series, and reveals a more considerable decrease in signal variance when compared to previously covered methods, without compromising any signal intensity.

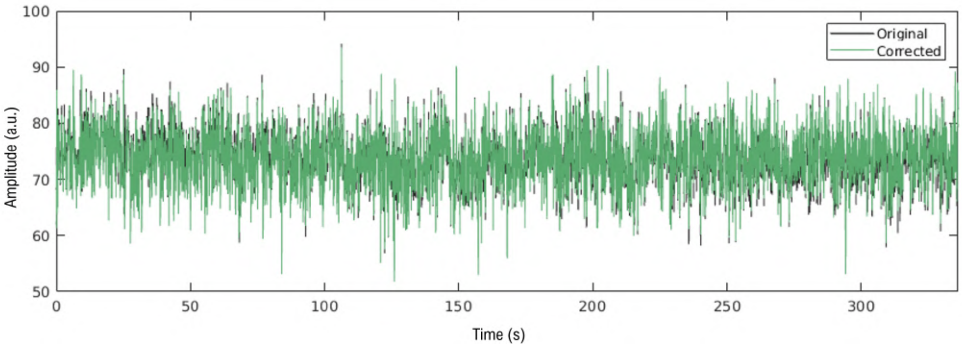

Figure 3.36: Comparison between the original and corrected fMRI time series, after regression of non-BOLD related independent components.

The effects of this particular correction on temporal SNR and on the distribution of t-values were evaluated in Figure 3.37.

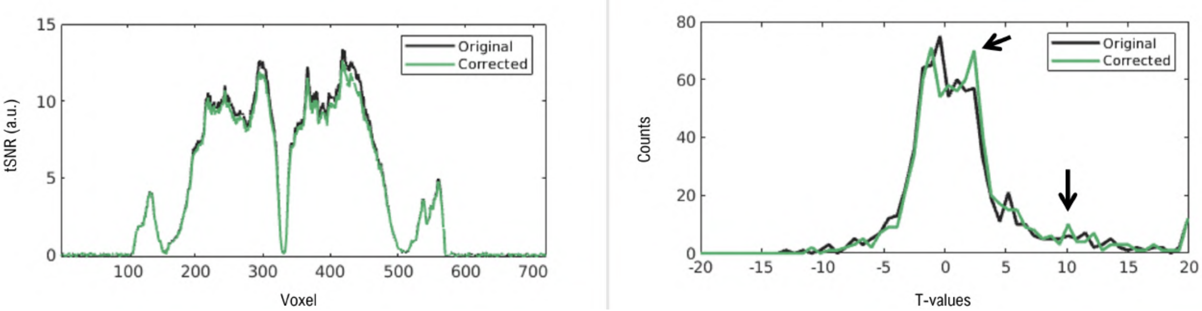

Figure 3.37: **(Left)** Temporal SNR plots and **(right)** t-values distribution for the original and corrected fMRI datasets. The arrows indicate an increase in the number of voxels with higher t-values for the corrected data.

The temporal SNR was generally lower for all voxels within the line when compared to the original fMRI data. However, there was an increment in the number of voxels with higher t-values.

In general, the effects of each method were coherent across subjects and suggest significant reduction of thermal noise and physiological fluctuations within line-scanning fMRI data. Table 3.4 summarizes the features of the data resulting from each noise correction strategy averaged for all four subjects, as well as the standard errors associated to these measures.

| | **Mean tSNR** | **Mean t-values** |
|---|---|---|
| **Reference**<br>**(SoS echo-combination)** | **11.13 ± 0.46** | **7.48 ± 4.11** |
| **NORDIC PCA** | 26.87 ± 1.46 | 8.78 ± 5.70 |
| **TE1 regression** | 10.60 ± 0.83 | 6.92 ± 3.49 |
| **WM+CSF regression** | 10.38 ± 0.70 | 6.88 ± 3.59 |
| **CSF regression** | 11.03 ± 0.52 | 7.37 ± 3.99 |
| **RETROICOR** | 11.21 ± 0.44 | 7.52 ± 4.18 |
| **ICA denoising** | 9.99 ± 0.71 | 7.23 ± 3.83 |

Table 3.4: Mean tSNR and t-values of a 10-voxel ROI averaged across all subjects for the denoising methods covered. The cells with a green overlay highlight the denoising methods for which the mean temporal SNR and t-values improved significantly.

The outcomes of applying the NORDIC PCA-based procedure and removing RETROICOR-based physiological regressors were particularly positive across subjects and improved the data significantly. The application of the remaining methods was less favorable.

# Chapter 4

# Conclusion

The presented work aimed to assess the performance of several signal source identification and denoising procedures (implemented for 2D and 3D fMRI) when applied to high-resolution line-scanning fMRI data acquired at 7T. At first, the nature of physiological noise sources and its role in fMRI was explored. A comprehensive review of the existing denoising strategies for fMRI data was carried out, and several of the methods described were selected to be implemented and evaluated in this study.

Due to the novelty aspect of line-scanning fMRI, the acquired multi-echo data was thoroughly inspected and the effects of applying each denoising procedure to the reference SoS-combined fMRI dataset were characterized both qualitatively and quantitatively. At last, and considering the results obtained during this project, the feasibility of implementing an optimized noise removal pipeline for high-resolution line-scanning fMRI at 7T can be assessed.

## 4.1 Contributions and concluding remarks

The results obtained throughout this work offer valuable insight regarding noise removal in line-scanning fMRI data acquired at 7T, and suggest optimistic perspectives for successful BOLD fMRI cleanup.

Although some software packages had to be adapted to ensure compatibility with line-scanning data, all the denoising techniques covered could be applied. The isolated cases of software incompatibilities due to the unique dimensions of line-scanning data (e.g., FSL MELODIC), ultimately provide important information about what tools require improvements.

Relying on the clear BOLD responses from the four subjects scanned, the efficacy of the hereby covered noise removal methods could be assessed. The NORDIC PCA-based implementation provided the largest increase in BOLD sensitivity and RETROICOR-based regression improved the quality of the fMRI data as well. The results presented validate the application of both NORDIC PCA and RETROICOR-based regression to line-scanning fMRI.

## 4.2 Limitations and future work

Some constraints and drawbacks have arised throughout this work, which could be addressed in future studies.

Due to the limited number of participants scanned, this study lacks in statistical power. Thus, the methods to be included in a general denoising pipeline for line-scanning fMRI data, as well as their relative order, could not be decided. Instead, an optimal denoising pipeline must be created according to the characteristics of each dataset.

Prior to GLM fitting of the short-TE regressor, a frequency analysis of the TE1 signal showed contributions from task-related BOLD fluctuations. To address this BOLD contamination, the short-TE signal was included in the GLM analysis as a nuisance regressor along with the regressor of interest (predicted BOLD response). Even so, short-TE1 regression revealed to be unsuccessful across all four subjects. Therefore, TE1 should be selected as close to zero as possible, in order to minimize BOLD contamination even further.

The less satisfactory performance of WM and CSF signal regression can be mainly attributed to inaccurate tissue segmentation due to partial volume effects, which is validated by the prominent peaks at the visual task frequency present in the spectra of these tissues (presented in Figure 3.5). The implementation of more accurate tissue segmentation algorithms, in particular for line-scanning fMRI data, is crucial for improving tissue-specific signal regression.

The NORDIC PCA-based implementation used in this study yielded a significant increase in BOLD sensitivity. For future work, NORDIC-denoised data should be used as the reference for the application of the remaining aforementioned denoising strategies, since thermal noise removal facilitates the detection of physiological noise [8]. Additionally, in the interest of improving the results obtained even further, a similar threshold-selecting approach to the one described in the literature can be applied [35][34]. Dynamic noise scans acquired during the fMRI scanning session could be utilized for estimating an ideal numerical threshold, as all they encompass is the noise floor of the MRI scanner (see Figure 4.1).

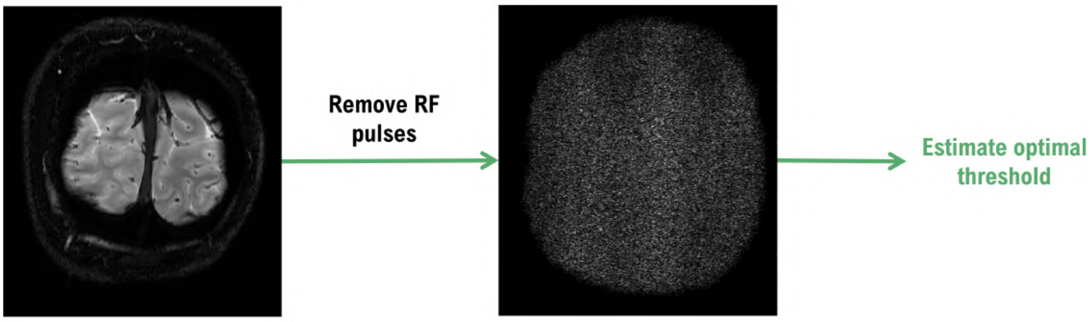

Figure 4.1: **(Left)** Slice image for a representative subject. **(Right)** Noise scan for the same subject - the radiofrequency pulses are turned off, which prevents not only slice excitation but also the placement of the OVS pulses.

To address the software incompatibilities encountered, existing frameworks should be improved and adapted to a wider range of dataset types and dimensionalities. Furthermore, new methods specific to line-scanning fMRI data can be established.

One of the main limitations of this study is the small sample size, as mentioned above. Future work should include a larger group of participants in order to confirm the results hereby obtained and to enable the implementation of a general preprocessing pipeline with adequate denoising for line-scanning fMRI data.

# References

[1] Raimondo, L., Knapen, T., Oliveira, I.A.F.d., Yu, X., Dumoulin, S.O., van der Zwaag, W., Siero, J.C.W. A line through the brain: implementation of human line-scanning at 7T for ultra-high spatiotemporal resolution fMRI. *Journal of Cerebral Blood Flow Metabolism*, 0(0):1–13, 2021.

[2] Dumoulin, S.O., Fracasso, A., van der Zwaag, W., Siero, J.C.W., Petridou, N. . Ultra-high field MRI: Advancing systems neuroscience towards mesoscopic human brain function. *NeuroImage*, 2017.

[3] Sabatini, B., Regehr, W. Timing of neurotransmission at fast synapses in the mammalian brain. *Nature*, 384:170–172, 1996.

[4] Baillarger, J.G.F. Recherches sur la structure de la couche corticale des circonvolutions du cerveau. *Mém. Acad. R. Méd.*, 8:149–183, 1840.

[5] Zilles, K., Palomero-Gallagher, N., Amunts, K. Myeloarchitecture and maps of the cerebral cortex. In *Brain Mapping: An Encyclopedic Reference.*, pages 137–156. Academic Press, 2015.

[6] Kruger, G., Glover, G.H. Physiological Noise in Oxygenation-Sensitive Magnetic Resonance Imaging. *Magn Reson Med*, 46:631–637, 2001.

[7] Bianciardi, M., Fukunaga, M., van Gelderen, P., Horovitz, S. G., de Zwart, J. A., Shmueli, K., Duyn, J. H. Sources of fMRI signal fluctuations in the human brain at rest: a 7T study. *Magn Reson Imaging*, 27(8):1019–1029, 2009.

[8] Caballero-Gaudes, C., Reynolds, R.C. Methods for cleaning the BOLD fMRI signal. *NeuroImage*, 156:128–149, 2017.

[9] Jezzard, P., Matthews, P.M., Smith, M.S. *Functional MRI: An Introduction to Methods.* Oxford University Press, 2001.

[10] Ogawa, S., Lee, T.M., Kay, A.R., Tank, D.W. Brain magnetic resonance imaging with contrast dependent on blood oxygenation. *Magn Reson Med*, 87(24):9868–9872, 1990.

[11] Hillman, E.M.C. Coupling Mechanism and Significance of the BOLD Signal: A Status Report. *Annu Rev Neurosci*, 37:161–181, 2014.

[12] Ogawa, S., Lee, T.M., Nayak, A.S., Glynn, P. Oxygenation-sensitive contrast in magnetic resonance image of rodent brain at high magnetic fields. *Magn Reson Med*, 14(1):68–78, 1990.

[13] Jezzard, Peter, Matthews, Paul M. Functional Magnetic Resonance Imaging. *Journal of Neurology Neurosurgery Psychiatry*, 75(1):6–12, 2004.

[14] Buxton, R.B. *Introduction to Functional Magnetic Resonance Imaging: Principles and Techniques.* Cambridge University Press, 2009.

[15] Zhang, S., Li, X., Lv, J., Jiang, X., Guo, L., Liu, T. Characterizing and differentiating task-based and resting state fMRI signals via two-stage sparse representations. *Brain Imaging Behav*, 10(1):21–32, 2016.

[16] Murphy, K., Birn, R.M., Bandettini, P.A. Resting-state fMRI confounds and cleanup. *NeuroImage*, 2013.

[17] Glover, G.H., Li, T., Ress, D. Image-Based Method for Retrospective Correction of Physiological Motion Effects in fMRI: RETROICOR. *Magn Reson Med*, 44:162–167, 2000.

[18] Biswal, B., Deyoe, E.A., Hyde, J.S. Reduction of physiological fluctuations in fMRI using digital filters. *Magnetic Resonance in Medicine*, 35(1):107–113, 1996.

[19] Yuen, N.H., Osachoff, N., Chen, J.J. Intrinsic Frequencies of the Resting-State fMRI Signal: The Frequency Dependence of Functional Connectivity and the Effect of Mode Mixing. *Front. Neurosci*, 13-900, 2019.

[20] Triantafyllou, C., Hoge, R.D., Krueger, G., Wiggins, C.J., Potthast, A., Wiggins, G.C., Wald, L.L. Comparison of physiological noise at 1.5 t, 3 t and 7 t and optimization of fmri acquisition parameters. *NeuroImage*, 26(1):243–250, 2005.

[21] Fracasso, A., Luijten, P.R., Dumoulin, S.O., Petridou, N. Laminar imaging of positive and negative BOLD in human visual cortex at 7T. *NeuroImage*, 164:100–111, 2018.

[22] Petridou, N., Italiaander, M., van de Bank, B., Siero, J., Luijten, P., Klomp, D. Pushing the limits of high-resolution functional MRI using a simple high-density multi-element coil design. *NMR in biomedicine*, 26(1):65–73, 2013.

[23] Kashyap, S., Ivanov, D., Havlicek, M., Sengupta, S., Poser, B.A., Uludağ, K. Resolving laminar activation in human V1 using ultra-high spatial resolution fMRI at 7T. *Scientific Reports*, 8(17063), 2018.

[24] Fischl, B., Dale, A.M. Measuring the thickness of the human cerebral cortex from magnetic resonance images. *Proceedings of the National Academy of Sciences of the United States of America*, 97(20):11050–11055, 2000.

[25] Siero, J.C.W., Oliveira, I.A.F.d., Choi, S., Yu, X. Implementing human line-scanning fMRI: Initial results of ultra-high temporal and spatial resolution fMRI. *ISMRM*, 2019.

[26] Morgan, A.T., Nothnagel, N., Petro, L.S., Goense, J., Muckli, L. High-resolution line-scanning reveals distinct visual response properties across human cortical layers. *bioRxiv*, 2020.

[27] Yu, X., Qian, C., Chen, D., Dodd, S.J., Koretsky, A.P. Deciphering laminar-specific neural inputs with line-scanning fMRI. *Nature Methods*, 11:55–58, 2014.

[28] Hu, X., Le, T.H., Parrish, T., Erhard, P. Retrospective estimation and correction of physiological fluctuation in functional MRI. *Magnetic Resonance in Medicine*, 34(2):201–212, 1995.

[29] Bartoň, M., Mareček, R., Krajčovičová, L., Slavíček, T., Kašpárek, T., Zemánková, P., Říha, P., Mikl, M. Evaluation of different cerebrospinal fluid and white matter fMRI filtering strategies - Quantifying noise removal and neural signal preservation. *Human brain mapping*, 40(4):1114–1138, 2019.

[30] Grajauskas, L.A., Frizzell, T., Song, X., D'Arcy, R. White Matter fMRI Activation Cannot Be Treated as a Nuisance Regressor: Overcoming a Historical Blind Spot. *Frontiers in neuroscience*, 13(1024), 2019.

[31] Chang, C., Ho, C., Chen, J. ADHD Classification by a Texture Analysis of Anatomical Brain MRI Data. *Frontiers in systems Neuroscience*, 6(66), 2012.

[32] Behzadi, Y., Restom, K., Liau, J., Liu, T.T. A component based noise correction method (CompCor) for BOLD and perfusion based fMRI. *NeuroImage*, 37(1):90–101, 2007.

[33] Kay, K., Rokem, A, Winawer, J., Dougherty, R., Wandell, B. GLMdenoise: A fast, automated technique for denoising task-based fMRI data. *Frontiers in Neuroscience*, 7(7):247, 2013.

[34] Moeller, S., Pisharady, P., Ramanna, S., Lenglet, C., Wu, X., Dowdle, L., Yacoub, E., Uğurbil, K., Akçakaya, M. NOise reduction with DIstribution Corrected (NORDIC) PCA in dMRI with complex-valued parameter-free locally low-rank processing. *NeuroImage*, 226, 2021.

[35] Vizioli, L., Moeller, S., Dowdle, L., Akçakaya, M., De Martino, F., Yacoub, E., Ugurbil, K. A Paradigm Change in Functional Brain Mapping: Suppressing the Thermal Noise in fMRI. *bioRxiv*, 2020.

[36] Beckmann, C.F., Smith, S.M. Probabilistic independent component analysis for functional magnetic resonance imaging. *IEEE Trans Med Imaging*, 23(2):137–152, 2004.

[37] Kelly, R. E., Jr, Alexopoulos, G. S., Wang, Z., Gunning, F. M., Murphy, C. F., Morimoto, S. S., Kanellopoulos, D., Jia, Z., Lim, K. O., Hoptman, M. J. Visual inspection of independent components: Defining a procedure for artifact removal from fMRI data. *Journal of Neuroscience Methods*, 189(2):233–245, 2010.

[38] Kaboodvand, N., Iravani, B., Fransson, P. Dynamic synergetic configurations of resting-state networks in ADHD. *bioRxiv*, 2019.

[39] Kundu, P., Voon, V., Balchandani, P., Lombardo, M.V., Poser, B.A., Bandettini, P. Multi-Echo fMRI: A Review of Applications in fMRI Denoising and Analysis of BOLD Signals. *NeuroImage*, 154:59–80, 2017.

[40] Poser, B.A., Versluis, M.J., Hoogduin, J.M., Norris, D.G. BOLD contrast sensitivity enhancement and artifact reduction with multiecho EPI: Parallel-acquired inhomogeneity-desensitized fMRI. *Magnetic Resonance in Medicine*, 55(6):1227–1235, 2006.

[41] Poser, B.A., Norris, D.G. Investigating the benefits of multi-echo EPI for fMRI at 7 T. *NeuroImage*, 45:1162–1172, 2009.

[42] Kundu, P,, Inati, S.J., Evans, J.W., Luh, W.M., Bandettini, P.A. Differentiating BOLD and non-BOLD signals in fMRI time series using multi-echo EPI. *NeuroImage*, 60(3):1759–1770, 2012.

[43] Yu, M., Lin, Q., Kuang, L., Gong, X., Cong, F., Calhoun, V. ICA of full complex-valued fMRI data using phase information of spatial maps. *Journal of Neuroscience Methods*, 249:75–91, 2015.

[44] Menon, R.S. Postacquisition Suppression of Large-Vessel BOLD Signals in High-Resolution fMRI. *Magnetic Resonance in Medicine*, 47:1–9, 2002.

[45] Stanley, O.W., Kuurstra, A.B., Klassen, L.M., Menon, R.S., Gati, J.S. Effects of phase regression on high-resolution functional mri of the primary visual cortex. *NeuroImage*, 227, 2021.

[46] Juchem, C., de Graaf, R.A. $B_0$ magnetic field homogeneity and shimming for in vivo magnetic resonance spectroscopy. *Analytical Biochemistry*, pages 1–13, 2016.

[47] Raimondo, L., Heij, J., Knapen, T., Dumoulin, S.O., Siero, J.C.W., van der Zwaag, W. Multi-echo line-scanning for ultra-high spatiotemporal resolution: optimal settings for BOLD sensitivity enhancement. *ISMRM*, 2021.

[48] Kasper, L., Bollmann, S., Diaconescu, A., Hutton, C., Heinzle, J., Iglesias, S., Hauser, T., Sebold, M., Manjaly, Z., Pruessmann, K., Stephan, K. The PhysIO Toolbox for Modeling Physiological Noise in fMRI Data. *Journal of Neuroscience Methods*, 276:56–72, 2016.

[49] Harvey, A. Pattinson, K., Brooks, J., Mayhew, S., Jenkinson, M., Wise, R. Brainstem Functional Magnetic Resonance Imaging: Disentangling Signal From Physiological Noise. *Journal of Magnetic Resonance Imaging*, 28:1337–1344, 2008.

[50] Majeed, W., Avison, M.J. Robust Data Driven Model Order Estimation for Independent Component Analysis of fMRI Data with Low Contrast to Noise. *PLoS ONE*, 9(4, e94943), 2014.

[51] Li, Y.O., Adali, T., Calhoun, V.D. Estimating the number of independent components for functional magnetic resonance imaging data. *Human brain mapping*, 28(11):1251–1266, 2007.

[52] Calhoun, V., Adali, T. Unmixing fMRI with independent component analysis. *Engineering in Medicine and Biology Magazine, IEEE*, 25(2):79–90, 2006.

[53] Ma, D., Deshmane, A., Mcgivney, D., Jiang, Y., Badve, C., Gulani, V., Seiberlich, N., Griswold, M. Partial volume mapping using magnetic resonance fingerprinting. *NMR in Biomedicine*, 32, 2019.

[54] Bodurka, J., Ye, F., Petridou, N., Murphy, K., Bandettini, P.A. Mapping the MRI voxel volume in which thermal noise matches physiological noise — Implications for fMRI. *NeuroImage*, 34(2):542–549, 2007.

[55] Attarpour, A., Ward, J., Chen, J. Vascular origins of low-frequency oscillations in the cerebrospinal fluid signal in resting-state fMRI: Interpretation using photoplethysmography. *Human Brain Mapping*, 42(8):2606–2622, 2021.

[56] Gawryluk, J., Mazerolle, E., D'Arcy, R. Does functional MRI detect activation in white matter? A review of emerging evidence, issues, and future directions. *Frontiers in neuroscience*, 8(239), 2014.

[57] Peters, A.M., Brookes, M.J., Hoogenraad, F.G., Gowland, P.A., Francis, S.T., Morris, P.G., Bowtell, R. T2* measurements in human brain at 1.5, 3 and 7 T. *Magnetic resonance imaging*, 25(6):748–753, 2007.

[58] Haast, R.A.M. *Quantitative brain MRI at 7T in healthy subjects and in metabolic diseases*. PhD thesis, Maastricht University, 2018.

[59] van der Zwaag, W., Francis, S., Head, K., Peters, A., Gowland, P., Morris, P., Bowtell, R. fMRI at 1.5, 3 and 7 T: characterising BOLD signal changes. *NeuroImage*, 47:1425–34, 2009.

[60] Ioannidis, G.S., Nikiforaki, K., Kalaitzakis, G., Karantanas, A., Marias, K., Maris, T.G. Inverse Laplace transform and multiexponential fitting analysis of T2 relaxometry data: a phantom study with aqueous and fat containing samples. *European Radiology Experimental*, 4(28), 2020.

[61] Bright, M.G., Murphy, K. Removing motion and physiological artifacts from intrinsic BOLD fluctuations using short echo data. *NeuroImage*, 64(6):526–537, 2013.

[62] Dedora, D., Nedic, S., Katti, P., Arnab, S., Wald, L., Takahashi, A., Van Dijk, K., Strey, H., Mujica-Parodi, L. Signal Fluctuation Sensitivity: An Improved Metric for Optimizing Detection of Resting-State fMRI Networks. *Frontiers in Neuroscience*, 10, 2015.

# Appendix A

# Publication arising from this thesis

*Noise removal in line-scanning fMRI*, Catarina Passarinho, Luisa Raimondo, Jurjen Heij, Tomas Knapen, Serge O. Dumoulin, Jeroen Siero, Wietske van der Zwaag; oral and poster presentations at the 38th Annual ESMRMB Scientific Meeting, Online, October 2021